IOP PUBLISHING REPORTS ON PROGRESS IN PHYSICS

Rep. Prog. Phys. **70** (2007) 1525–1582 doi:10.1088/0034-4885/70/9/R02

Nuclear structure and astrophysics

H Grawe[1], **K Langanke**[1,2] **and G Martínez-Pinedo**[1]

[1] Gesellschaft für Schwerionenforschung (GSI), D-64291 Darmstadt, Germany
[2] Institut für Kernphysik, Technische Universität Darmstadt, D-64289 Darmstadt, Germany

E-mail: h.grawe@gsi.de

Received 16 March 2007
Published 29 August 2007
Online at stacks.iop.org/RoPP/70/1525

Abstract

The nuclear structure in regions of the Segré chart which are of astrophysical importance is reviewed. The main emphasis is put on those nuclei that are relevant for stellar nucleosynthesis in fusion processes, and in slow neutron capture, both located close to stability, rapid neutron capture close to the neutron dripline and rapid proton capture near the proton dripline. The basic features of modern nuclear structure, their importance and future potential for astrophysics and their level of predictibility are critically discussed. Recent experimental and theoretical results for shell evolution far off the stability line and consequences for weak interaction processes, proton and neutron capture are reviewed.

(Some figures in this article are in colour only in the electronic version)

This article was invited by Professor W Nazarewicz.

0034-4885/07/091525+58$90.00

Contents

1. Introduction

Nuclear structure physics and the visible Universe are intimately related since nuclear physics drives many astrophysical processes. These include Big Bang nucleosynthesis and the evolution and final fate of stars. The ejecta of these objects are dispersed into interstellar space where they can serve as seeds for a new generation of stars. The observed abundances of the elements in the Universe and its subsystems are fingerprints to trace back the pathways of nucleosynthesis in terms of their astrophysical parameters. A reliable description of the underlying astrophysical scenarios depends crucially on the knowledge of nuclear properties in the relevant regions of the Segré chart involving both nuclei close to stability, for example, in the heavy-ion fusion below the nickel–iron region, which is important for advanced stellar burning, and the slow neutron capture (s-process) beyond, as well as exotic nuclei far-off stability in the rapid neutron capture (r-process) on the neutron-rich side and the rapid proton capture (rp-process) close to the proton dripline. There are a number of phenomena which highlight the impact of nuclear structure on astrophysics, as for example, the

- triple-α process crossing the bottleneck towards nuclei heavier than Li;
- maximum in binding energy per nucleon terminates heavy-ion fusion in stellar burning at $A \approx 60$;
- s-process peaks at $A = 88$, 140, 208 related to the closed shells at stability;
- rp-process bottlenecks due to dripline staggering and strong binding in α-like nuclei and process termination due to fast α decay beyond ^{100}Sn;
- electron capture Gamow–Teller (GT) resonance structure in the core collapse of massive stars and
- r-process abundance peaks at $A = 80$, 130, 195 due to neutron shell closures in neutron-rich nulei.

Current key questions in nuclear astrophysics include the origin of the elements, the physics of stellar explosions, nuclear and mixing processes in stars, the nature of compact objects like white dwarfs and neutron stars and the thermonuclear explosions on their surfaces like novae and x-ray bursts. Further sites for chemical element formation are main-sequence stars and core-collapse and thermonuclear supernovae.

A number of recent reviews have been published on various aspects of the interplay of nuclear structure and reactions and astrophysics [1–5]. In this paper we address mainly the nuclear structure impact in regions of the Segré chart which are relevant to astrophysical network calculations for location of the reaction flow of nucleosynthesis in the chart and of the possible sites in the universe. The role of nuclear structure in nuclear reactions in the astrophysics environment, for pre-supernova star evolution and neutrino detection in earthbound detectors is reviewed. The roadmap is illustrated in the Segré chart of figure 1 together with the location and pathways of various astrophysical processes. This review is intended to give in sections 2–6 the theoretical background based on modern nuclear structure models for students and experimentalists entering and/or working in the field of nuclear astrophysics and updates the status in key examples for the processes, as outlined in figure 1, in sections 7–11. The general scope of this work is an overview of the basic nuclear structure phenomena while the detailed numerical results are quoted in numerous references. It should be noted that this review can give only a snap-shot of the status in this rapidly developing field of research.

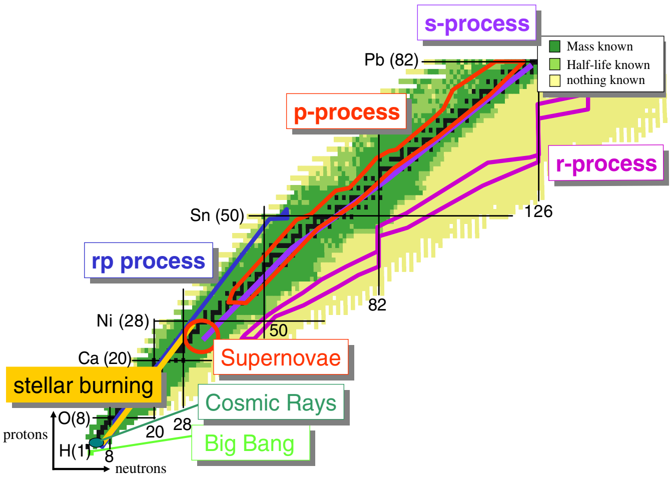

Figure 1. The astrophysical Segré chart. Shell closures and magic numbers beyond ${}^{16}_{8}O_8$ are indicated by black lines and labeled by chemical symbol (Z) and N for protons and neutrons, respectively (figure by courtesy of H Schatz).

2. Shell evolution scenarios near and far-off stability

2.1. *Spherical closed shell nuclei*

Doubly closed shell nuclei (CS) are fixpoints of the nuclidic chart and play, as indicated above, particularly important roles in various astrophysical nucleosynthesis processes. From the spectra of their neighboring nuclei one can infer experimental single-particle (hole) energies (SPE) and two-body matrix elements (TBME), which provide crucial benchmarks for mean-field predictions from Hartree–Fock calculations using density functional interactions, shell evolution scenarios and for interactions based on a renormalized G-matrix as derived from realistic nucleon–nucleon potentials. In figure 2 SPE for well-established stable and far-off-stability doubly magic nuclei are displayed. The data are compiled in [6, 7] and implemented with recent extrapolations for ^{78}Ni and a re-evaluation of ^{131}In and ^{131}Sn in the vicinity of the doubly magic nucleus ^{132}Sn [9]. Firm experimental values supported by spectroscopic factors are available for the stable nuclei ^{16}O, ^{40}Ca, ^{48}Ca, ^{208}Pb [8] and partly for the long-lived ^{56}Ni inferred from a radioactive target experiment [8, 10]. For ^{132}Sn the lowest particle (hole) levels are associated with single nucleon states, while the ^{100}Sn [11] and ^{78}Ni [12, 13] values were extrapolated from regions of stable nuclei by shell model calculations. The lack of spectroscopic factors may lead to serious misinterpretation of single-particle states especially for orbits far beyond and below the Fermi level. In the example of the CS nucleus ^{48}Ca (figure 2(b)) the strength for the lowest proton orbits $f_{7/2}$, $p_{3/2}$, $p_{1/2}$ is well concentrated in the first excited states of each spin. The $f_{5/2}$ strength, however, is highly fragmented as shown in figure 3 [14, 15] with the lowest state deviating from the centroid by $\approx$1 MeV. The good news is that shell model calculations in the pf space can account for it [15]. A specific case is the position of the $g_{7/2}$ neutron–hole state in ^{132}Sn as it is intimately related to the lowest 1^+ state in ^{130}In populated in the β decay of ^{130}Cd [16]. Using the relative strength for the $\nu g_{7/2} \rightarrow \pi g_{9/2}$ GT conversion (π and ν denote protons and neutrons, respectively) to the three observed final $7/2^+$ states [8] as a measure for the spectroscopic $\nu g_{7/2}$ strength in these states yields the $\nu g_{7/2}$ centroid 457 keV above the lowest $7/2^+$ state taken as input for shell

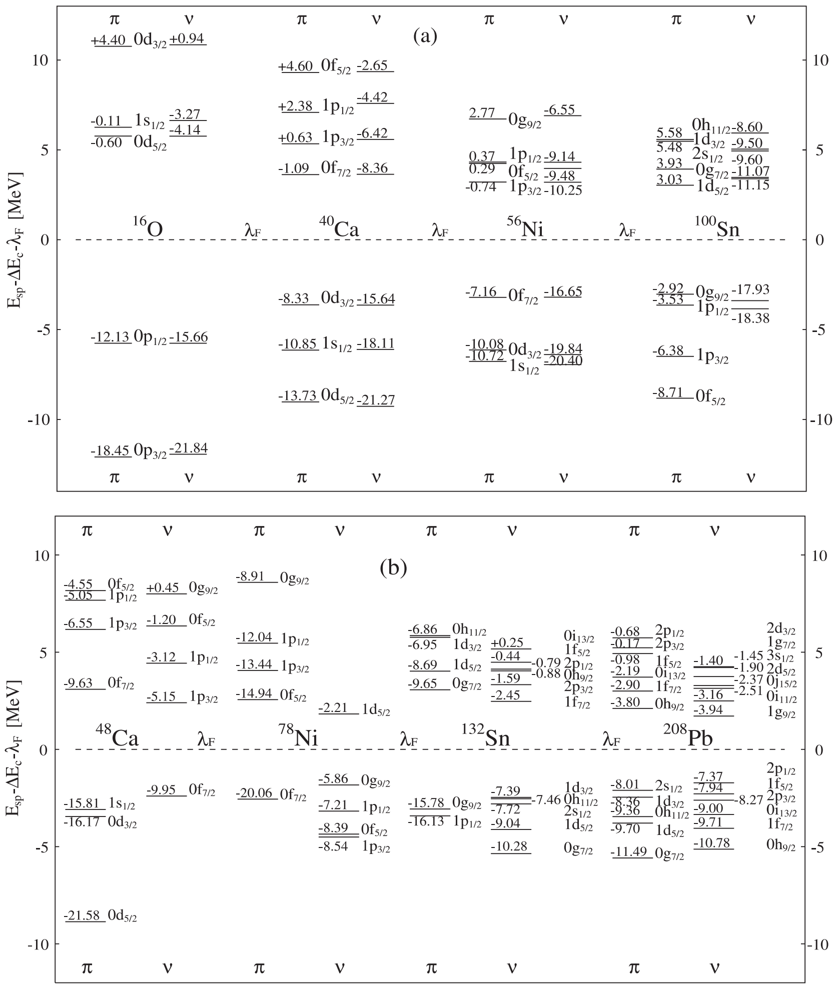

Figure 2. Experimental single-particle (hole) proton (π) and neutron (ν) energies for the doubly magic $N = Z$ nuclei ^{16}O, ^{40}Ca, ^{56}Ni, ^{100}Sn (*a*), and the neutron rich ^{48}Ca, ^{78}Ni, ^{132}Sn, ^{208}Pb (*b*). The energies are normalized to the middle of the shell gap (λ_F), which eliminates the Coulomb energy difference ΔE_C. The numbers next to the levels quote the absolute single-particle energies including the Coulomb shift. Data are from [6–8] unless otherwise specified in the text.

model calculations [16]. The new value from figure 2(*b*) would solve most of the discrepancies found in reproducing the ^{130}In 1^+ state in shell model calculations. It is disputable, however, which choice of shell model input, the yrast (lowest) $7/2^+$ state or the $g_{7/2}$ centroid, is the proper choice. Further details of this topic and alternative solutions are discussed in section 10.2.

The evolution of SPE is determined by the monopole part V^{m} of the residual interaction if Coulomb effects are neglected [7] (see equations (5, 6) in section 2.4). In the case where SPE are not known for exotic CS nuclei a global fit of V^{m} to experimental data can be used to infer unknown values [17]. Another global approach to SPE is provided by the mean-field Hartree–Fock (HF) method employing density functional interactions [18] or relativistic mean-field calculations [19]. It should be noticed though that SPE determined by different methods are

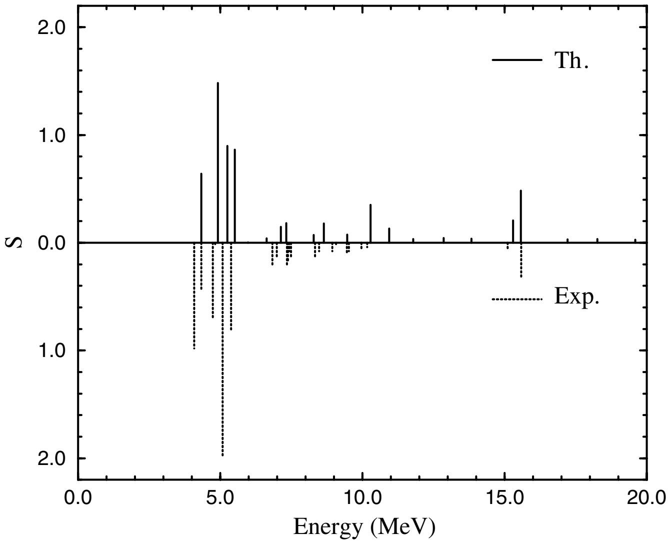

Figure 3. Spectroscopic factors, $S(j, t_z, E_x^i)$, corresponding to stripping of a particle in the orbit $1f_{5/2}$ for a ^{48}Ca target [15]. E_x^i are excitation energies in the final nucleus ^{49}Sc, and the normalization $\sum_i S(j, t_z, E_x^i) = (2j + 1)$ is used.

not strictly equivalent

- a global central potential of a given shape may not account for the realistic nucleon distribution and/or correlations of nucleons at the Fermi surface;
- empirically determined experimental SPE may not exhaust the full spectroscopic strength of the j orbit and
- SPE resulting from mean-field models may not account for correlations of e.g. the pairing ($L = 0$), quadrupole ($L = 2$) or octupole ($L = 3$) type, though it is in principle possible to include these modes.

It is obvious from figures 1 and 2 that the shell structure as dictated by the CS nuclei determines the various pathways of nucleosynthesis along the $N = Z$ stable (stellar burning) and unstable nuclei (rp-process) (figure 2(*a*)), and the $N \gg Z$ unstable nuclei (r-process) (figure 2(*b*)). The paths of all three proceses additionally depend strongly on the detailed open-shell structure in the deformed region.

2.2. *Spherical shell model and its limitations*

Shell-model calculations require four basic ingredients which are mutually interrelated: (i) an appropriate model space, (ii) an effective interaction, (iii) a powerful computer code and (iv) a high-capacity computer. The model space is selected according to the observables to be calculated and the performance of the computer code. The effective two-body interaction and single-particle operators for observables depend on the chosen model space and are strictly valid only for the specific space. Any changes such as truncation require their renormalization. In three recent papers the basic principles of modern shell model approaches have been reviewed as a unified view of nuclear structure with emphasis on nuclei far-off stability and astrophysical applications [14, 20, 21] and on a textbook level [7].

The model space must be well adapted to the problem, as: *what is not allowed for in the model space cannot be calculated reliably*. For example observables such as electromagnetic transition and GT strengths cannot be predicted properly if orbitals with strong contributions such as $\Delta l = 2$ orbits for $E2$ transitions and spin–orbit partners for M1 and GT transitions are excluded from the model space. This deficiency cannot be absorbed in a renormalization. Within the 'no-core' shell model many harmonic oscillator (HO) shells involving up to 6 $\hbar\omega$ for $A = 12$ and up to 50 $\hbar\omega$ for $A = 4$ can be treated in *ab initio* calculations using realistic interactions [22, 23]. For heavier systems an inert core has to be assumed and effective residual interactions and operators as described below have to be employed. With modern shell model codes untruncated calculations within one HO shell can be performed for the 0p ($N = 1$, ^{4}He–^{16}O), 1s,0d ($N = 2$,^{16}O–^{40}Ca) and 1p,0f ($N = 3$,^{40}Ca–^{80}Zr) shell. Inclusion of ph excitations around shell closures and of intruder orbitals in jj major shells with $Z, N \geqslant 28$ require truncation. This can be achieved in various ways: (i) restriction of the number of shell model orbitals, sometimes called *vertical* truncation; (ii) restriction of the ocupation number within a given set of single-particle orbits (*horizontal* truncation), which in high-j orbitals is often achieved by seniority truncation [24] and (iii) restriction according to importance of a configuration, e.g. by excluding components with the least bound diagonal matrix elements from the diagonalization [25] or by probing importance by Monte Carlo sampling [21, 26].

Realistic effective interactions are inferred from experimental nucleon–nucleon (NN) scattering data via effective NN potentials fitted to the data [14] or deduced from chiral effective theories [27, 28]. In the standard approach the NN interaction V_{NN} is used to calculate the G-matrix plus higher-order many-body corrections [29]. This eliminates the strong repulsive core in V_{NN} and accounts for a given model space of occupied and empty 'scattering' orbitals for core polarization contributions to the TBME up to a given order of folded diagrams [29]. Here the notion 'scattering' is used for empty orbitals outside the valence space which are usually unbound. The occupied and scattering states are defined by a doubly magic core serving as reference for the shell model calculation. This method introduces a mass (A) dependence in the extracted TBME, thus requiring a new calculation for every new core nucleus. Unfortunately reliable SPE cannot be obtained in this way and therefore are taken from experiment.

Recently a method was developed to eliminate the hard core repulsive (high momentum) contributions to V_{NN} directly [30]. The resulting smooth and non-singular $V_{\mathrm{low}\text{-}k}$ can then be used to calculate core polarization corrected TBME carrying no A dependence. The approach is analogous to the Lee–Suzuki method [31] in momentum space. Though it was never proven rigorously that the procedures to infer realistic interactions converge, the renormalized G-matrix and the $V_{\mathrm{low}\text{-}k}$ TBME give an extremely good description of energy levels near closed shells. Alternatively short-ranged central and tensor correlations can be included in the unitary correlation operator method (UCOM) [32, 33].

Large-scale shell model calculations have revealed that in spite of the excellent results near closed shells realistic interactions fail to reproduce binding energies and the evolution of single-particle structure from one closed shell nucleus CS to the next. The reason is two-fold: (i) core polarization diagrams become less perturbative with increasing number of valence nucleons in the model space and (ii) the neglect of real and effective three-body forces. Both effects accumulate with the number of valence nucleons added to the core nucleus. As the evolution of SPE throughout a shell is determined solely by the monopole part of the interaction (section 2.4), this deficiency can be cured by adding a constant to the diagonal TBME in each multiplet. In equation (6) of section 2.4 the dependence on the number of valence nucleons is demonstrated in the factor $(2j + 1)$ for a filled subshell. This correction has been proven extremely successful in the (1s,0d) [34] and (1p,0f) shells [35–37]. Alternatively empirical interactions were obtained by a free fit of TBME to experimental data for the smaller (0p) model space [38] and constrained fits of linear combinations of TBME for the larger spaces in the (1s,0d) [39,40] and (1p,0f) shells [41,42]. For convenience a renormalized G-matrix is used as a starting point [40,42].

The standard shell model diagonalization by the Lanczos technique can be performed without truncation in the 0p, 1s0d and 1p0f major harmonic oscillator shells. Powerful computer codes such as the widely used OXBASH [43], ANTOINE [14,44], NATHAN [14,44], REDSTICK [45] and MSHELL [46] are at hand. While in the pf shell the maximum model space at $N = Z = 30$ (^{60}Zn) with 2.3×10^9 $M = 0$ Slater determinants can be treated, the limitation is given by the deformation-driving intruder $0g_{9/2}$ and $1d_{5/2}$ orbits which make the extended model space intractable without severe truncation and consequences for the correct description of nuclear shapes.

To treat even larger model spaces an alternative to the diagonalization method, the shell model Monte Carlo (SMMC) method [47, 48] allows calculation of nuclear properties as thermal averages, employing the Hubbard–Stratonovich transformation to rewrite the two-body parts of the residual interaction by integrals over fluctuating auxiliary fields. The integrations are performed by the Monte Carlo techniques, making the SMMC method available for basically unrestricted model spaces. While the strength of the SMMC method is the study of nuclear properties at finite temperature, it does not allow for detailed nuclear spectroscopy. Moreover, for realistic interactions there exists an intrinsic sign problem that requires extrapolation from specific forces free of this problem [49,50]. The quantum Monte Carlo diagonalization (QMCD) method of [21, 51, 52] consists of exploring the mean-field structure of the valence space by means of Hartree–Fock calculations enforcing good quantum numbers by projection techniques. Then the Monte Carlo sampling techniques are used to obtain an optimal set of basis states and the full Hamiltonian is explicitly diagonalized in this basis. More basis states are iteratively added until convergence is achieved. A strong connection between the mean-field and the shell model techniques is also established in the Vampir approach [53,54].

2.3. Deformed shell gaps in midshell

As one can see in figure 1 major parts of the various pathways of nucleosynthesis proceed through the open-shell regions of the Segré chart. Except for the stellar burning between ^{16}O and ^{56}Ni the nuclear structure impact in these regions is dominated by deformation and shape dependent shell structure. Since the microscopic origin of rotational motion was established [55] it has been proven that with a sufficient large configuration space deformation is treatable within the shell model. In practice this is limited due to computing capacity to the sd [39] and pf [36] shells, where within a $0\hbar\omega$ space rotational motion was successfully described. In heavier nuclei deformation is introduced phenomenologically and determined selfconsistently by variational methods.

For a reliable calculation of the reaction and β-decay rates it is important to take the nuclear shape properly into account. The deformation not only affects the mass predictions and the predictions for the associated Q-values but also the reaction cross section predictions with the Hauser–Feshbach model [56] as well as predictions for the β-decay half lives [57]. Here the Q-value is defined as the mass difference of the reaction partners in the entrance and exit channel of a reaction and the parent nucleus and its decay products, respectively. Large prolate as well as oblate deformations have been predicted for certain mass regions along the rp-process and also the r-process path. Only limited experimental information is available about the actual deformation of isotopes and the associated impact on masses, half lives, level densities and fission. The most important deformation mode for our specific applications is the quadrupole deformation. The intrinsic quadrupole moment Q_2 is directly related to the nuclear charge distribution and therefore to the nuclear shape. The quadrupole deformation parameter ϵ_2 can be directly derived from the intrinsic quadrupole moments Q_i

$$\epsilon_2 = -1 + \sqrt{1 + (5/2ZR_0^2)Q_i}, \tag{1}$$

where Z is the charge number and R_0 is the mean nuclear radius. The intrinsic quadrupole moment Q_i is directly related to the quadrupole moment Q_0 of the ground state with spin J by

$$Q_0 = \frac{3K^2 - J(J+1)}{(J+1)(2J+3)} \cdot Q_i \tag{2}$$

with K as the projection of the angular momentum J on the symmetry axis.

Alternatively the quadrupole deformation can be derived from the reduced E2 γ strength $B(E2; (JK)_{\text{initial}} \to (JK)_{\text{final}})$ within a rotational band. This is mostly done in even–even nuclei for the ground state transition from the first excited 2^+ state, where

$$Q_i = \sqrt{\frac{16\pi}{5} \frac{B(E2; 2^+ \to 0^+)}{e^2}}. \tag{3}$$

This approach assumes that the 2^+ state is predominantly rotational. By using $B(E2; 2^+ \to 0^+)$ data it is not possible to distinguish between prolate and oblate deformation since the sign of Q_i remains undetermined. The bulk of the presently available experimental information comes mainly from Coulomb excitation experiments and is limited to stable or long-lived isotopes [58]. Recently new experimental methods have been developed for Coulomb excitation of radioactive species at intermediate and low energy to infer $B(E2)$ values [59–61]. For even–even nuclei where the $B(E2)$ strength has not been measured but information about the excitation energy of the first excited 2^+ state is available global systematics can be applied to determine the deformation parameter ϵ_2 [58, 62, 63]

$$\epsilon_2 \approx 0.95 \sqrt{\frac{1228}{A^{7/3} E_x(2_1^+)}} \tag{4}$$

with A being the mass number of the deformed nucleus and $E_x(2_1^+)$, the energy of the first 2^+ state, in MeV.

Based on the liquid-drop model hybrid macroscopic–microscopic approaches have found wide applications to calculate the astrophysically relevant data for masses, level densities and shapes in the full range of nuclei including deformed open-shell regions. The existing experimental data base of deformation [58] is complemented by a large range of theoretical model predictions for deformation far from stability. For astrophysical applications the finite range droplet model (FRDM) [64] and the extended Thomas–Fermi plus Strutinsky integral (ETFSI) model have often been used to predict the ground state deformation for a vast range of nuclei between the proton and the neutron driplines [58, 65]. The need for physics beyond the global liquid-drop picture introduces microscopic corrections in a phenomenological manner. For mass predictions the FRDM model in its latest most sophisticated version became thus the macroscopic–microscopic mass formula (see section 5.1), which has been applied to many astrophysical problems including r-process nucleosynthesis. More recently the Hartree–Fock–Bogoliubow (HFB) method employing density functionals has been globally applied on different levels of sophistication (for a recent review see [66]).

The basic input for the microscopic corrections are the SPE in a deformed potential well, which can be of the harmonic oscillator, Woods–Saxon or folded Yukawa type. Figure 4 shows proton SPE for the deformed $N = Z = 40$ nucleus ^{80}Zr calculated for the latter approach [57]. At this mass the neutron and proton patterns are almost identical. Clearly developed shell gaps for various deformations of any shape (spherical, oblate and prolate) are seen for similar

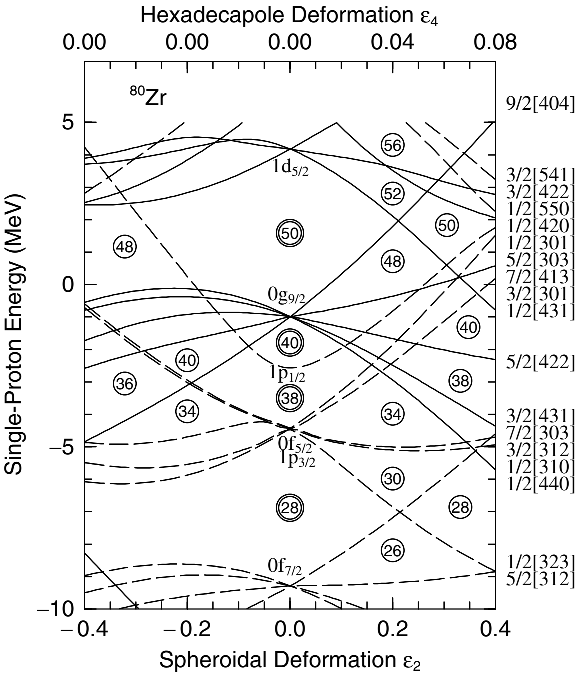

Figure 4. Deformed shell model level scheme along the rp-process path [57]. The lower and upper abscissae give the quadrupole and hexadecupole deformation parameters ϵ_2 and ϵ_4, respectively. The levels are labeled by the standard Nilsson asymptotic quantum numbers $\Omega[N\Lambda\Sigma]$ and parity $(-1)^N$. Exact quantum numbers are the projection of the nucleon angular momentum on the symmetry axis Ω and the harmonic oscillator main quantum number N. For spherical shape the quantum numbers nlj are listed.

or identical nucleon numbers. This is a clear signature for shape coexistence in this region of the rp-process path with mutual mixing and consequences for the GT decay, which is discussed in section 11. Note the shape coexistence for the $N = Z$ waiting point nuclei ^{80}Zr (triple), ^{76}Sr, ^{72}Kr and ^{68}Se. Spectroscopic factors for proton capture and decay might be strongly reduced due to shape mismatch in the initial and final states [67, 68]. Moreover, the presence of a high-spin orbital $g_{9/2}$ and odd-parity pf orbitals gives rise to K isomerism of multi-quasiparticle states which may compete in excitation, capture and decay with ground states. Shape coexistence and K isomerism are of great importance for the s- and r-process paths between the $N = 50$ and 82 and $N = 82$ and 126 neutron shells which is discussed further in sections 8 and 10.

The ETFSI method is a fast-speed approximation to the Hartree–Fock model with Skyrme forces. Pairing correlations are treated within the BCS approach assuming a δ-force [69]. These results are complemented by relativistic mean-field calculations (RMF) [70], the Hartree–Fock plus BCS approach (HF–BCS) [71] and full HFB [72] calculations for predicting ground state deformation for a large number of nuclei [73]. All these models treat deformation up to higher multipole orders, including terms in addition to the quadrupole deformation, the octupole, ϵ_3, the hexadecapole, ϵ_4 and hexacontatetrapole ϵ_6 deformations. In figure 5 the results of various approaches are shown as two-neutron separation energies, which are a measure for the shell gap structure (see section 2.4 for a definition of S_{2n}) in the astrophysically relevant region $Z = 30$–70 and $N = 40$–140, and are compared with a shell model based mass formula by Duflo and Zuker [74]. The latter decomposes the nuclear Hamiltonian into its monopole

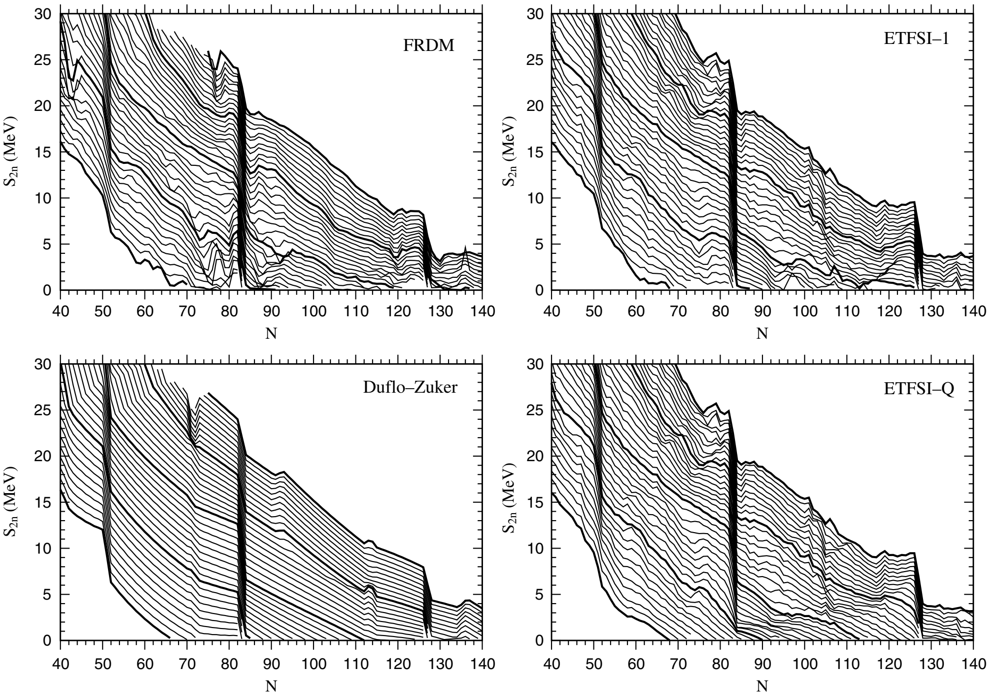

Figure 5. Two-neutron separation energies for $N = 40$–140 for four different mass models, the microscopic-macroscopic finite range droplet model (FRDM) [57], the extended Thomas–Fermi with Strutinsky integral (ETFSI-1) model [69, 78], the Duflo–Zuker mass formula [74] and the quenched ETFSI-Q model [79]. The bold lines correspond to the Z values 30, 40, 50, 60 and 70.

and multipole part and by accurate application of scaling laws that warrant shell formation and saturation a mass formula with a global set of 28 parameters is derived. Clear ridges characterize the $N = 50$, 82 and 126 shells. At $Z \approx 40$ a fading $N = 82$ shell structure appears in the ETFSI-Q model and an irregular ‘saddle point’ structure visible below $N = 82$ in ETFSI-1 and FRDM is smoothed in these approaches. This behavior has been discussed as the origin for the filling of a trough in the r-process abundance distributions below $A = 120$, observed in earlier r-process abundance calculations (see section 10.2).

Most estimates of the half lives of r- and rp-process nuclei are so far based on a combination of global mass models and the quasiparticle random phase approximation (QRPA), the latter to calculate the GT matrix elements. Examples of these models are the FRDM/QRPA [57] and the ETFSI/QRPA [75]. Recently, calculations based on the self-consistent Hartree–Fock–Bogoliubov plus QRPA model became available for even–even r-process waiting point nuclei near the magic neutron numbers $N = 50$, 82 and 126 [76]. An alternative globally applicable approach has been developed in the density functional QRPA (DF-QRPA) [77], which also consistently accounts for the contributions of forbidden transitions to the β half lives, but yet can only be applied to spherical nuclei. The impact of nuclear shapes on GT distributions for rp nuclei will be discussed in section 11.

2.4. Shell evolution towards large N/Z ratios

Two scenarios with different experimental signature have been proposed to describe the shell structure of nuclei on the pathway towards large N/Z ratios. The first is based on the larger

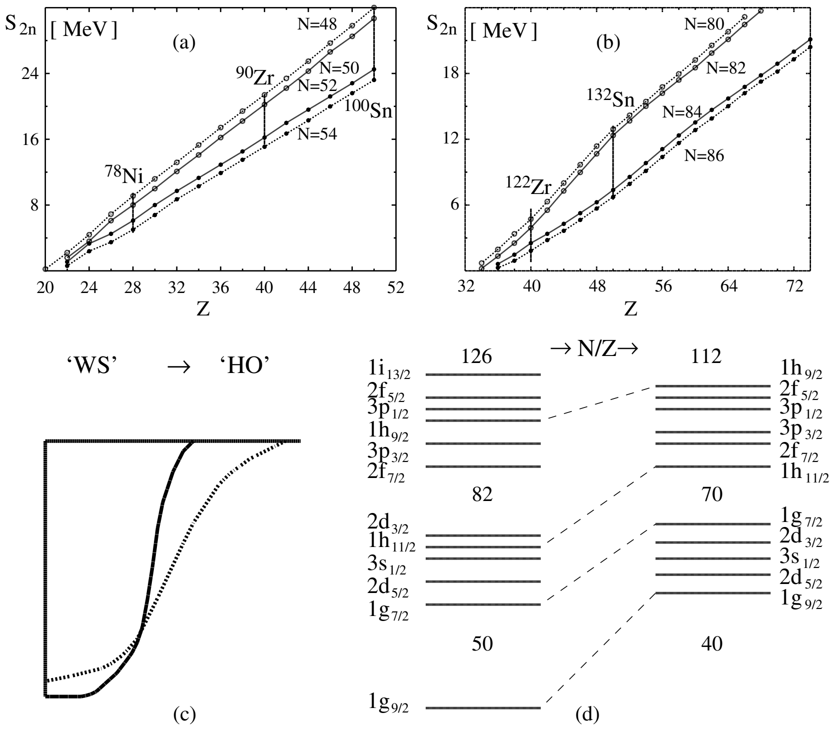

Figure 6. Evolution of neutron SPE from $N = Z$ to $N/Z \gg 1$. In the upper panel results from a Hartree–Fock mean-field calculation for the two-neutron separation energy S_{2n}, which is a measure for the neutron shell gap, along the $N = 50$ (*a*) and $N = 82$ (*b*) isotones are shown [80]. The vertical bars are experimental or shell model extrapolated values from figure 2 for $Z = 28$ (Ni) and 50 (Sn) and from [13] for $Z = 40$ (Zr). The lower panel shows schematically the evolution of SPE from a Woods–Saxon (WS) to a harmonic oscillator type (HO) potential when progressing from $N = Z$ towards $N \gg Z$ as indicated for the $l = 4$ and $l = 5$ orbitals.

radial extension and a softer neutron potential. This shifts large-l orbitals upward in energy and reduces the spin–orbit (SO) splitting, which is proportional to the potential gradient, for nucleon orbitals probing the nuclear surface [81, 82]. Thus for medium-heavy and heavy nuclei the harmonic oscillator (HO) unique-parity shells are restored. The signature for changing neutron shell structure is that it evolves smoothly with A and N/Z and only large variations of these parameters, as expected towards the neutron dripline, will have substantial effects. Proton orbitals are affected only indirectly by their interaction with neutrons. This is demonstrated schematically in the lower panel of figure 6. In the upper panel the results of a Hartree–Fock mean-field calculation are shown for the two-neutron separation energies $S_{2n} = BE(Z, N) - BE(Z, N - 2)$ which give a pairing corrected measure for the shell gap between $N = N_{\mathrm{CS}} + 2$ and $N = N_{\mathrm{CS}}$ [80]. From this and previous work [82] conclusions were drawn in numerous theoretical and experimental publications that at large N/Z ratios the normal shell gaps known from close to stability would disappear and even new shell gaps would open (see lower panel of figure 6). For the r-process nucleosynthesis it was shown for $N = 82$ and $N = 126$ that this scenario qualitatively accounts for the abundance trough at $A = 120$ and 180 in astrophysical network calculations [3, 83, 84] (see figure 20). There are, however, three caveats to be considered: (i) a soft potential implies a reduction of the SO splitting as this is proportional to the derivative of the potential; such a reduction, however, was not applied in [3, 84, 85]; (ii) the experimental and extrapolated shell gaps, as shown by vertical bars in the upper panel of figure 6, even at $N = Z$ (^{100}Sn) and stability (^{90}Zr) are largely underestimated by the mean-field results [80] and (iii) the corresponding astrophysical network calculations were based on a classical static r-process model that does not account for the complicated dynamics expected in realistic astrophysical scenarios. It should be noted, however, that a more recent calculation, based on high-entropy expansions, while filling the $A = 180$ trough, came to the same conclusion for the nuclear physics origin of the $A = 120$ abundance deficiency [86].

The second scenario originates from the strong monopole shifts of selected shell model orbits. They have been ascribed to the tensor force of the NN interaction [87–90], their predictibility, however, is limited due to the neglect of three-body forces. Therefore experimental monopole tuning is indispensable in shell model applications (see section 2.2 and below). The monopole part of the nucleon–nucleon (NN) interaction determines the evolution of single-particle (hole) energies from one closed shell (CS′) to the next (CS). This provides the key input for the shell model and is further demonstrated in the applications of sections 9 and 10. The monopole for a specific multiplet (j, j') is defined by

$$V^{\mathrm{m}}_{jj'} = \sum_J (2J+1)\langle jj'J\,|V|\,jj'J\rangle \Big/ \sum_J (2J+1), \tag{5}$$

which gives rise to the single-particle energy evolution between the two shell closures [7]

$$\epsilon^{\mathrm{CS}}_j = \epsilon^{\mathrm{CS}'}_j + \sum_{j'} (2j'+1-\delta_{jj'}) V^{\mathrm{m}}_{jj'}. \tag{6}$$

The Kronecker symbol applies for $T = 1$ and identical orbitals (j, j') to maintain the Pauli principle. This simple formula can be used to extrapolate single-particle energies from experimentally known CS nuclei into the unknown territory. It should be noted that equation (6) holds only for closed j' shells, in between due to configuration mixing the trend may deviate according to the incomplete subshell filling. The exact progression can be inferred from a full shell model calculation. Strong monopole drifts have been experimentally observed all over the Segré chart, the most prominent being the $\Delta l = 0$ spin–orbit $\pi\nu$ pairs $0\mathrm{p}_{3/2}$–$0\mathrm{p}_{1/2}$, $0\mathrm{d}_{5/2}$–$0\mathrm{d}_{3/2}$, $0\mathrm{f}_{7/2}$–$0\mathrm{f}_{5/2}$, $0\mathrm{g}_{9/2}$–$0\mathrm{g}_{7/2}$ and the $\Delta l = 1$ spin-flip pairs $0\mathrm{p}_{1/2}$–$0\mathrm{d}_{5/2}$, $0\mathrm{d}_{3/2}$–$0\mathrm{f}_{7/2}$, $0\mathrm{f}_{5/2}$–$0\mathrm{g}_{9/2}$, $0\mathrm{g}_{7/2}$–$0\mathrm{h}_{11/2}$. They are summarized in recent reviews [7, 87–89] and can be traced back to the $\sigma\tau$ and tensor parts of the NN interaction [87, 88]. Recently, based on sound evidence from spectroscopic factors the $\pi 0\mathrm{g}_{7/2}$–$\nu 0\mathrm{h}_{11/2}$ drift was confirmed, and for the first time a high spin $\Delta l = 2$ case $\pi 0\mathrm{g}_{7/2}$–$\nu 0\mathrm{i}_{13/2}$ was established [91]. This translates into the following criteria for strong monopoles: (i) the interacting nucleons are spin-flip partners with (ii) $\Delta l = 0, 1, 2$ and (iii) should have the same number of nodes in their radial wave functions to optimize the overlap. These features are also borne out in realistic interactions as derived from effective NN potentials fitted to scattering data via standard many-body techniques [29] as shown in figure 17 of [7]. They suffer, however, from the fact that the monopole part is not determined well and has to be tuned to experimental shell evolution as discussed in section 2.2, which hampers their predictive power. The dramatic impact of monopole drifts and the sensitivity to subtle details of the interaction is due to the factor $(2j'+1)$ in equation (6) which is large in filling (emptying) a high-spin orbital j' and translates monopole corrections of about 100 keV into MeV. This is shown schematically along with the signatures of the scenario in figure 7. Two disclaimers should be kept in mind though: (i) until now there is no stringent experimental proof for the SPE evolution shown on the rhs of figure 7, i.e. the opposite sign of the $\nu j_{>}\pi j'_{<}$ and $\nu j_{>}\pi j'_{>}$ monopoles with $j'_{>,<} = l \pm 1/2$; so far only the increased binding of the $\pi j'_{<}$ relative to a $\pi j = l + 1/2$ reference level (lowest in the π shell as indicated by a dashed line on the rhs of figure 7) was observed [87]; (ii) besides the $\pi\nu$ (T=0) monopoles the $T = 1$ interaction especially for spin–orbit partners may create substantial values of monopoles as

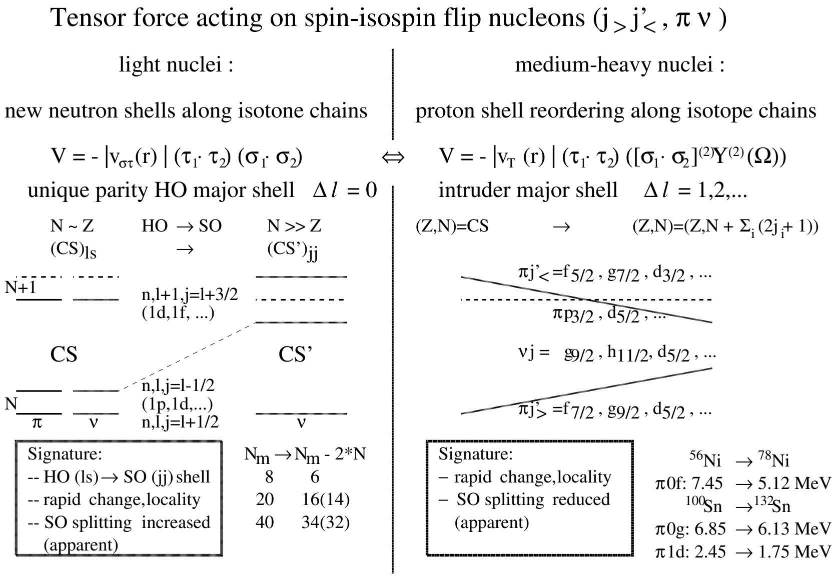

Figure 7. Schematic illustration of signatures for tensor force driven shell evolution for neutron states along isotone chains (lhs) and proton shells along isotope chains (rhs) towards neutron excess [13, 87]. The lhs illustrates the case of proton–neutron spin–orbit partners ($\Delta l = 0$): emptying a proton $\pi j_> = \mathrm{p}_{3/2}, \mathrm{d}_{5/2}, \mathrm{f}_{7/2}$ orbit will release binding of the $\nu j_< = \mathrm{p}_{1/2}, \mathrm{d}_{3/2}, \mathrm{f}_{5/2}$ neutrons to close the $N = 8$, 20, 40 (sub)shells, while opening new $N = 6$, 16(14), 34(32) shells and thus increasing the neutron SO splitting. The ambiguity 14/16 and 32/34 is due to the presence of an intermediate $j = 1/2$ orbit which exhibits a strong $T = 1$ monopole (pairing), i.e. if full it opens a gap to the next higher orbit and if empty the gap is below the $j = 1/2$ orbit. The rhs shows the effect of reduced apparent spin–orbit splitting of proton orbits $\pi j = l \pm 1/2, l = 3, 4, 2$ when filling neutron orbits $\nu j'_> = l' + 1/2, l' = 4, 5, 2$ as consequence of the tensor force. The experimental values and extrapolated shell gaps are from figure 2 and table 1.

Table 1. Apparent spin–orbit splitting for $l = 2$–4 orbitals throughout a full shell along the $Z = 21$, 29 and 51 isotopes for protons and the $N = 27$ isotones for neutrons. $\mathrm{SO}_{\mathrm{beg}}$ and $\mathrm{SO}_{\mathrm{end}}$ and their difference refer to the SO splitting for protons and neutrons at the beginning and end of the respective filled-up neutron or proton shell.

CS ± 1 chain	$l, j_>, j <$	$\mathrm{SO}_{\mathrm{beg}}$ (MeV)	$\mathrm{SO}_{\mathrm{end}}$ (MeV)	Difference (MeV)	Comment
$Z = 21$ (Sc)	$\pi 3, \mathrm{f}_{7/2}, \mathrm{f}_{5/2}$	5.69	5.08	−0.61	^{41}Sc–^{49}Sc
$Z = 27, 29$ (Co,Cu)	$\pi 3, \mathrm{f}_{7/2}, \mathrm{f}_{5/2}$	7.45	5.12	−2.33	^{55}Co,^{57}Cu–^{77}Co,^{79}Cu
$Z = 49, 51$ (In,Sb)	$\pi 4, \mathrm{g}_{9/2}, \mathrm{g}_{7/2}$	6.85	6.13	−0.72	^{99}In,^{101}Sb–^{131}In^{133}Sb
$Z = 51$	$\pi 2, \mathrm{d}_{5/2}, \mathrm{d}_{3/2}$	2.45	1.75	−0.70	^{101}Sb–^{133}Sb
$N = 27, 29$	$\nu 3, \mathrm{f}_{7/2}, \mathrm{f}_{5/2}$	8.75	7.17	−1.58	^{47}Ca,^{49}Ca–^{55}Ni,^{57}Ni

well. The apparent SO splitting is further discussed in the following paragraph. In section 10 for r-process path nuclei around ^{78}Ni and below ^{132}Sn a semi-quantitative discussion of the scenario is given.

In the discussion of shell evolution with increasing N/Z ratio the spin–orbit splitting serves as signature for the specific scenario. It is unique for the softening of the potential (figure 6) for neutrons only, while it is ambivalent in the monopole driven case (figure 7)

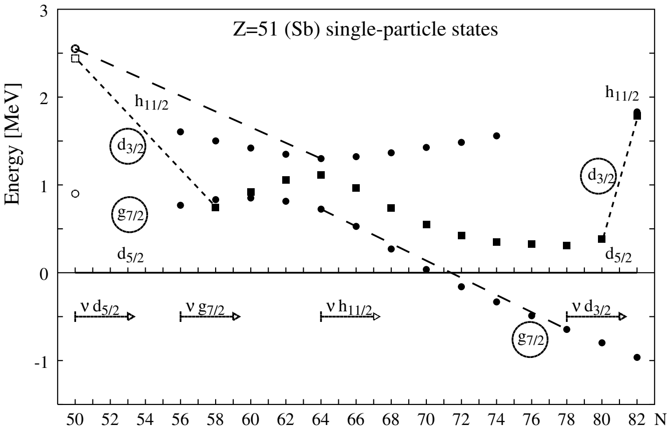

Figure 8. Apparent spin–orbit splitting for $Z = 51$ single proton orbitals with reference to the $\pi d_{5/2}$ state [13]. Experimental values are denoted by full symbols, extrapolated ones by open ones. Dashed lines are drawn to guide the eye.

for both protons and neutrons. For a qualitative discussion in figure 8 the unsuspicious case of evolution of experimental single proton states in $Z = 51$ (Sb) isotopes throughout the major neutron shell from ^{100}Sn to ^{132}Sn is shown with N/Z increasing from 1 to 1.32. In the following qualitative discussion it should be kept in mind that the neutron orbitals are not filled successively but due to configuration mixing partly in parallel, and that spectroscopic factors have been measured consistently only for the $\pi g_{7/2}$ and $\pi h_{11/2}$ states [91]. Striking monopole drifts can be observed for the $\pi\nu g_{7/2}$–$h_{11/2}$ and the $\pi\nu d_{3/2}$–$d_{5/2}$ pairs of nucleons.

- It has been known for a long time that the $\pi g_{7/2}$ is more strongly bound relative to the $\pi d_{5/2}$ reference state as soon as the $\nu h_{11/2}$ is filled above $N = 64$ with a net effect of ~1.9 MeV (lower long-dashed line in figure 8). The same monopole determines the downsloping of the $\pi h_{11/2}$ orbital upon filling of the $\nu g_{7/2}$ between $N = 50$ and 64 by ~1.2 MeV (upper long-dashed line in figure 8). The ratio of the net effects according to equation (6) is close to that of the multiplicities $(2j + 1)$ of the filled neutron orbitals, namely 12/8 . The exact trend is distorted in this case as the $\nu g_{7/2}$ is also acting on the $\pi d_{5/2}$ reference state. From a tensor monopole drift (see figure 7 rhs) one would expect that the $\pi g_{9/2}$ spin–orbit partner would be lifted up by filling of the $\nu h_{11/2}$ which should result in a reduced spin–orbit splitting between the $\pi g_{9/2}$ and $\pi g_{7/2}$ orbitals [87]. The latter effect is masked and compensated, however, by the strong (see [13] figure 4) $\pi g_{9/2}$–$\nu g_{7/2}$ monopole, as the $\nu g_{7/2}$ is filled before and/or in parallel.
- With respect to apparent SO splitting the $\pi d_{3/2}$–$d_{5/2}$ energy difference is a much better study object as it does not depend on the driving force behind the monopole. The splitting reduces from $N = 50$–56 when the $\nu d_{5/2}$ orbit is filled, it increases from $N = 78$ to 82 when the filling of the $\nu d_{3/2}$ binds the reference level $\pi d_{5/2}$ more strongly than the $\pi d_{3/2}$ (short dashed lines in figure 8). As it is the identical monopole, which rules the shift, the ratio of down- and up-shift should be 4/6. In fact the ratio is smaller and this is due to two other neutron orbitals that are being filled in between. From $N = 56$ to 64 the splitting increases due to the $\nu g_{7/2}$ filling effect on the $\pi d_{5/2}$ reference while from $N = 64$ to 76 it reduces again due to the $\pi d_{3/2}$–$\nu h_{11/2}$ monopole. Again the multiplicity factor 12/8 results in a net decrease of the SO splitting, if the two different monopoles involved have a similar value.

As the sign of the SO splitting always places the $j_<$ level above the $j_>$ it can be concluded that a major part of the observed SO reduction for proton levels by adding neutrons from $N = Z$ towards larger N/Z values within a full major shell is related to the trivial $(2j' + 1)$ weighting factor of equation (6) that always favors $j_<$ over $j_>$ energetically as discussed for proton states along the Sn isotopes. The opposite holds for neutron levels when protons are removed towards larger N/Z along isotonic chains. This is not in contradiction to the recently observed SO reduction along $N = 82$ from ^{144}Sm to ^{132}Sn [91], as this covers only the lowest $\pi 1d_{5/2}$ and $\pi 0g_{7/2}$ part of the $Z = 50$–82 proton shell leaving aside the effect by the $\pi 1d_{3/2}$ and $\pi 0h_{11/2}$ orbitals. Any shell model based theory with correct monopoles should account for this general feature.

2.5. *Summary and implications of shell driving mechanisms*

The various facets of shell driving mechanisms and implications for the predictibility of shell structure far off the stability line can be summarized as follows.

- The monopole part of the in-medium NN interaction determines the shell evolution and causes shell reordering but, depending on the orbits involved, not necessarily quenching.
- The tensor force is one major ingredient of the NN interaction, but due to negligence of the three-body forces the predictibility of shell structure is rather limited though first attempts to cure the deficiency are en route.
- A pragmatic way to solve the problem is shell model based empirical monopole tuning. It has the advantage that the tuning can be done in an experimentally accessible region but is essentially limited to one major shell and non-midshell nuclei. Using a global set of parameters the method has been applied to derive a mass formula.
- Microscopic–macroscopic and mean-field approaches based on density functionals are globally applicable but until recently lack explicit tensor terms.
- Monopole-driven shell evolution is symmetric in isospin (i.e. symmetric to $N = Z$) and any deviation from that must be ascribed to dripline effects, which become important at very small separation energies not necessarily on the pathways of nucleosynthesis (see section 10, equation (10) and figure 21 for typical S_n values).

3. Continuum shell model

Whenever the nucleosynthesis paths for explosive scenarios are approaching the driplines the standard shell model for well-bound nuclei is subject to modifications as interactions and shell structure change due to coupling to continuum states. The theoretical challenge in the description of weakly bound nuclei is the strict treatment of both the many-body correlations and the positive-energy continuum states. For bound states virtual scattering into the continuum via intermediate states will alter the nucleon–nucleon interaction. The consistent inclusion of the continuum in multi-configuration mixing calculations is achieved in the continuum shell model (CSM) (see [92] for a review). In spite of the outstanding success of the standard shell model which neglects coupling to scattering states even for weakly bound systems there are problems such as the Thomas–Ehrmann shift [93] which show up for weakly bound single particle levels in figure 2(*a*). Note the relative downward shift of the low-l proton levels in ^{16}O ($s_{1/2}$–$d_{5/2}$), ^{40}Ca (p–f) and ^{56}Ni ($p_{1/2}$–$f_{5/2}$). Nevertheless large-scale shell model calculations using the positive SPE in the core nuclei ^{16}O and ^{40}Ca give an excellent description throughout the 1s0d [39] and 1p0f [36, 42] shell, respectively.

In the CSM [94] and the recently developed shell model embedded in the continuum (SMEC) [95], the scattering states and bound states are treated on an equal footing. So far, most applications of the CSM, including SMEC, have been used to describe limiting situations in which there is coupling to one-nucleon decay channels only. Recently, the multiconfigurational shell model in the complete Berggren basis [96] was developed, the so-called Gamow shell model (GSM) [97]. By going into the complex energy (momentum) plane, GSM overcomes a number of difficulties of the traditional CSM; in particular, it can be applied to systems containing several valence neutrons.

The basic idea behind GSM is the use of resonant (Gamow) states, i.e. generalized eigenstates of the time-independent Schrödinger equation with complex energy eigenvalues. These states correspond to the poles of the S-matrix in the complex energy plane lying on or below the positive real axis; they are regular at the origin and satisfy purely outgoing asymptotics. The single-particle basis corresponds to eigenstates of a spherical single-particle finite potential (such as a Woods–Saxon potential). The generalized completeness relation involving Gamow states [96,98] can be written as

$$\sum_n |\phi_{jn}\rangle\langle\tilde{\phi}_{jn}| + \frac{1}{\pi}\int_{L_+} |\phi_j(\boldsymbol{k})\rangle\langle\phi_j(\boldsymbol{k}^*)|\mathrm{d}\boldsymbol{k} = 1, \tag{7}$$

where ϕ_{jn} are the Gamow states carrying the single-particle angular momentum j, n stands for the remaining quantum numbers, $\phi_j(\boldsymbol{k})$ are the complex-momentum scattering states, and the contour L_+ in the complex k-plane has to be chosen in such a way that all the poles in the discrete sum are contained in the domain between L_+ and the real energy axis. If the contour L_+ is chosen reasonably close to the real energy axis, the first term represents the contribution from bound states and narrow resonances, while the integral part accounts for the non-resonant continuum. In a standard large-scale shell model one uses routinely the Lanczos method to find low-energy eigenstates, which are bound, in a very large configuration space. This method cannot be applied to many-body resonances because of a huge number, i.e. a full continuum, of surrounding many-body scattering states, many of them having lower energy than the resonances. Therefore a problem pertaining to the interpretation of the GSM results is the selection of states associated with resonant excitations of the system. Bound states can be clearly identified, because the imaginary part of their energy must be zero. No equally simple criterion exists for resonance states. Fortunately, the coupling between scattering states and resonant states is usually weak; hence, one can determine the physical resonances by considering first the subspace of Gamow states (the so-called pole expansion) and then by adding the non-resonant continuum.

The main applications of the GSM so far are neutron-rich isotopes of He [99], Li [100] and O [99]. In figure 9 GSM results for the neutron-rich isotopes of helium and oxygen are shown [99]. The effect of continuum coupling on apparent spin–orbit splitting in the 0p shell was investigated for ^{5,7}He [101]. Future application could be the rp-process path in the 1s,0d shell, where large mirror energy differences (MED) point to a proton dripline effect [102], and in the upper 1p,0f shell, where in ^{70}Br hints for a quenching of the two-body interaction were observed [103]. So far mainly schematic interactions were applied but investigations to use realistic interactions [104] are on the way to improve spectroscopic predictability. Recently calculations for the He chain were performed in this way [105].

The continuum shell model is custom-tailored to treat particle decay and nuclear reactions. Recently the SMEC was applied to two-proton emission and to astrophysically relevant reactions by treating one (or two) particle(s) in the continuum [106, 107]. Interesting application of the models deal with ^{7}Li(n,γ) [108] and ^{17}F(p,γ) [109] reactions and the low-energy ^{7}Be(p,γ)^{8}Be reaction [108] which is crucial for understanding the high-energy neutrino spectrum from the sun. Extrapolation of measured cross sections for the latter reaction [110] are usually performed on the basis of microscopic three-cluster resonating group models with

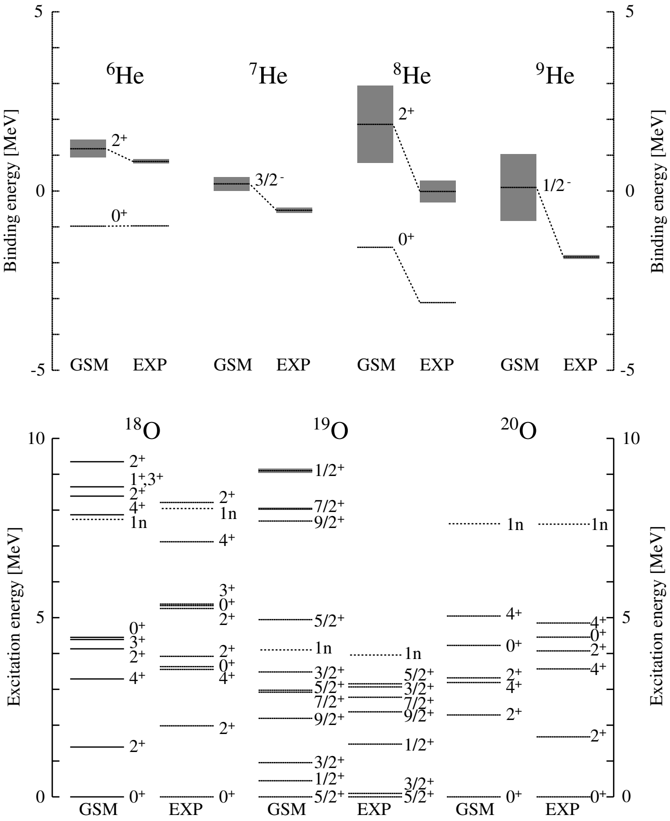

Figure 9. Experimental $^{6-9}$He (upper panel) and $^{18-20}$O (lower panel) bound and resonance states are compared with GSM results [99]. For He, the binding energies are given relative to ^{4}He and for O excitation energies are shown. The resonance widths are indicated by shadowing and the one-neutron separation energies by dashed lines.

simplified empirical NN interactions (see section 4). Examples of such studies are reported in [111–114]. Very recently a first attempt to adopt the no-core shell model [22] for the description of low-energy nuclear reactions has been reported [115]. This model studies fusion reactions assuming a potential model description for the low-energy cross section, but derives the important spectroscopic information of the states involved from a full shell model treatment with realistic interactions. Finally, the Green's function Monte Carlo method has been applied to calculate cross sections for the five-body problem of neutron-alpha scattering at low energy from realistic NN potentials [116].

4. Cluster structure in nuclear astrophysics

It is well known that besides single particle and collective aspects light nuclei exhibit additionally cluster degrees of freedom. While shell model based approaches are able to describe the former the inclusion of clustering is quite challenging and have led to the development of microscopic cluster models which have been applied to the description of astrophysically important reactions between light nuclei. The nuclear cluster model gives a unique description of nuclear bound and scattering states taking the Pauli principle among all nucleons fully into account [117]. However, it is based on the assumption that the full many-nucleon wave function can be approximated by an antisymmetrized cluster product state where the internal degrees of freedom of the clusters are frozen and that the nuclear low-energy phenomena are solely determined by the dynamics of the relative motion among the clusters, which is governed by some (often effective) Hamiltonian. Nevertheless due to the potential selection of a basis made of multi-cluster wave functions supplemented by shell model-like states, the cluster model has a large flexibility and can be the method of choice to describe several structure phenomena in light nuclei. Another strong point of the method is the ability to consistently describe bound, resonant and scattering states based on the same microscopic Hamiltonian. This makes the cluster model a very useful tool for the study of astrophysically important reactions between (relatively) light nuclei where a direct measurement of the cross sections at the astrophysically most effective energies is often impossible and the required information is achieved by extrapolation of data to lower energies.

Reviews of the cluster model and its application to nuclear structure and astrophysical applications can be found in [118, 119] and in [120, 121], respectively. These cluster model studies have usually been based on antisymmetrized many-body wave functions consisting of harmonic oscillator single-particle states with a common oscillator parameter and determine the dynamics from an empirical, rather simple nucleon–nucleon interaction. Recently the coupled-cluster method has undergone a renaissance in nuclear structure physics [122]. Since the early work in 1970s [123] this approach to the many-body problem has found little attention in nuclear physics but was applied with tremendous success in quantum chemistry. Applications in nuclear structure studies were resumed in different approaches by Mihaila and Heisenberg [124] and Dean and Hjorth-Jensen [122] with focus on ^{16}O. The method is fully microscopic, works with a no-core G-matrix as NN interaction, can in principle be extended to include three-body forces and can treat weakly bound systems [122].

In another exciting recent development cluster model applications have been improved in two important aspects: (i) by introducing more flexible wave functions and (ii) by using more realistic NN interactions. These improved models (antisymmetrized molecular dynamics (AMD) [125] and fermionic molecular dynamics (FMD) [126]) have been quite successfully applied to nuclear structure problems in light nuclei and the FMD has very recently been used to study astrophysically important reactions.

4.1. Fermionic molecular dynamics

In the FMD the many-body states are given by Slater determinants with Gaussian wave packets for the spatial degrees of freedom of the single-particle states. The intrinsic states of the cluster nuclei are determined by minimizing the intrinsic energy expectation value with respect to all the single-particle parameters (e.g. the complex width parameters of the Gaussians). The translational, rotational and parity symmetries of the intrinsic states are guaranteed by appropriate projections. Improved intrinsic wave functions are achieved by multi-configuration mixing where the basis configurations are obtained by minimizing the energy under constraints on collective variables like dipole, quadrupole or octupole moments.

The important short-ranged nucleon–nucleon correlations are accounted for by using the unitary correlation operator method (UCOM) [32, 33]; i.e. they are introduced by an unitary operator which is given by a product of a central and a tensor correlator [32, 33]. The parameters in these central and tensor correlators are determined by variation in the various spin–isospin channels of the two-nucleon system. The matrix elements of the momentum-dependent interaction, defined this way, are very similar to those of the $V_{\mathrm{low}-k}$ in momentum space. No three-body interaction is taken explicitly into account, but it is simulated by a

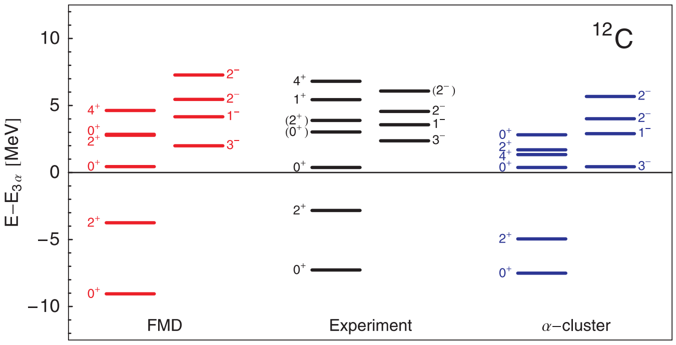

Figure 10. The ^{12}C level scheme relative to the 3α threshold in comparison to FMD and α cluster results [129].

correction term which is fitted to the binding energies and radii of the double-magic nuclei ^{4}He, ^{16}O, and ^{40}Ca. Detailed descriptions of the FMD and its applications to nuclear structure are given in [126–128].

4.2. *FMD and AMD applications to nuclear structure*

The FMD method has been successfully used to study the development of nuclear structure in the ground states of isotopic chains of light nuclei. Using the dipole moment as a collective generator coordinate, the binding energies and charge radii of the even helium isotopes are reproduced quite well. In particular, the soft-dipole mode has been identified to generate important ground state correlations in the Borromean nuclei ^{6}He and ^{8}He [130]. Similarly successful descriptions are obtained for beryllium and boron isotopes [131]. For medium-heavy nuclei the AMD has been used to study ^{20}Ne [132] and superdeformation in ^{40}Ca [133]. An interesting extension of the AMD to kaonic nuclei has been reported in [134].

Particularly powerful FMD and AMD studies have been reported for the carbon isotopes, covering the range from the proton-deficient ^{10}C over the tightly bound ^{12}C to the neutron rich ^{20}C [129, 135]. Again a good overall reproduction of the binding energies and the charge and matter radii is obtained. Importantly, based on a multi-configuration study, it has been possible to obtain a fair account of the low-energy spectrum of ^{12}C (figure 10) including the famous Hoyle state, which is known to have an extended triple-alpha structure, and is usually not reproduced by *ab initio* calculations like the no-core shell model [136]. It has been speculated that the Hoyle state corresponds to an alpha-condensate state [137]. A recent FMD study [138], which described the electromagnetic properties of this state very well, could not give a decisive answer to this interesting proposal (see also section 7).

The nucleus ^{16}C has been found to have a surprisingly small $B(E2)$ transition from the ground state to the first excited 2^{+} state ($B(E2, 0^{+} \rightarrow 2^{+}) = 3.15 \pm 0.95 e^{2} fm^{4}$ [139]). AMD [135] and FMD [129] studies explain this small value by almost decoupled proton and neutron matter distributions. While the proton distribution is nearly spherical, the neutron distribution is strongly deformed (figure 11). We mention in passing that surprisingly small $B(E2)$ values with strong deviations from the empirical Grodzins rule [62] are found also in other regions of the nuclear chart (e.g. for ^{68}Ni and ^{136}Te) and are here explained by the dominance of neutron excitations in the 2^{+} state [140–142].

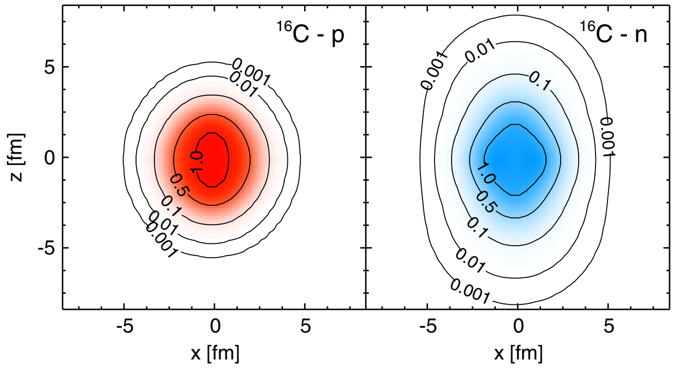

Figure 11. Proton and neutron shape distribution in ^{16}C [129]. The coordinates z and x denote the symmetry axis and the axes perpendicular to it.

4.3. FMD applications to astrophysically relevant reactions

The FMD is a very promising tool to describe astrophysically important nuclear reactions among light nuclei as it combines the flexibility in the choice of basis wave functions for bound and scattering states with the virtue to account for the relevant degrees of freedom and correlations among the nucleons. For example, the FMD reproduces the spectrum and the low-energy ^{3}He +^{4} He scattering phase shifts quite well [143]. Hence it should be extended to a calculation of the $^3\mathrm{He}(\alpha, \gamma)^7\mathrm{Be}$ cross section at solar energies; such a study is in progress.

Another example for the capabilities of the FMD model is given in figure 12 which shows the astrophysical S-factors for the sub-barrier fusion of various oxygen isotopes [144]. Fusion of two ^{16}O nuclei triggers oxygen burning as one of the last stages in stellar hydrostatic evolution, while the fusion of the neutron-rich oxygen isotopes ^{22}O and ^{24}O explores the potential increase in the fusion cross sections due to the pronounced neutron tails which develop in neutron-rich nuclei. The fusion of such neutron-rich isotopes is expected to be relevant for the evolution of the crust matter of a neutron star if the latter accumulates matter from a binary star and undergoes regular x-ray bursts [145]. Two facts are worth mentioning from figure 12: at first, the FMD calculation reproduces the ^{16}O+^{16}O fusion data quite well, without adjustment of any parameters. Secondly, the pronounced neutron tail enhances the fusion cross sections for the other oxygen isotopes by several orders of magnitude stressing the sensitivity of the fusion process to a correct description of the asymptotic cluster wave functions. While FMD studies for the many pycnonuclear fusion reactions needed to simulate the neutron star crust evolution are yet computationally not feasible, such studies are, however, very useful to check and constrain simple phenomenological potential models [146].

5. Global nuclear properties: masses, half lives, level densities

5.1. Masses

Nuclear structure and its evolution as a function of mass and isospin determines the behavior of nucleosynthesis processes. The importance of nuclear structure has already been recognized when the so-called s-process and r-process peaks in the galactic abundance distribution were recognized as signatures of the impact of the nuclear shell structure on these processes [147, 148].

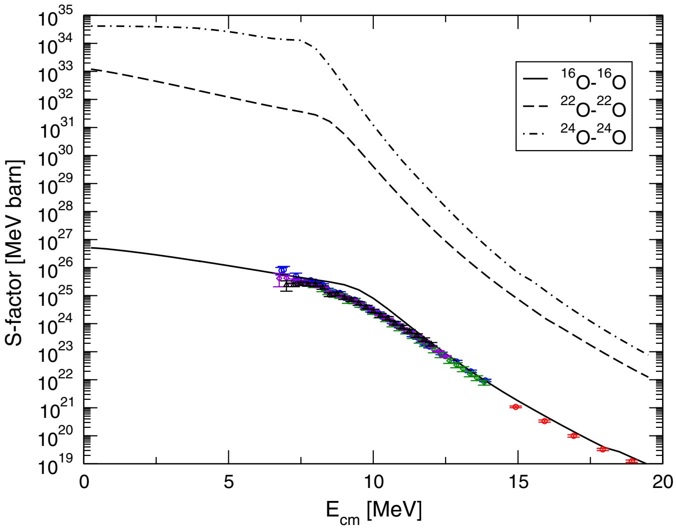

Figure 12. FMD S-factors for the fusion reactions of various oxygen isotopes [144].

One of the most obvious nuclear parameters is the nuclear mass. Masses determine the valley of stability, the separation energies and the position of the driplines, the decay Q-values, i.e. the half lives of radioactive nuclei and the reaction energetics. Therefore masses or mass differences determine the energy generation in nucleosynthesis processes, mass differences decide on which decay channels are open for compound states and determine reaction branchings that affect the reaction path and therefore guide the nucleosynthesis pattern. Mass differences also determine equilibrium conditions and the timing of nucleosynthesis events. While in general nuclear masses near stability are well known and tabulated [149], the uncertainties on masses are mainly associated with regions far-off stability in the nuclear chart. In these regions the nuclear masses used in large scale nucleosynthesis simulations are largely based on model predictions. As an example in figure 13 the binding energy per nucleon is shown for nuclei near stability. One can clearly recognize the nearly equal values for ^{4}He, ^{8}Be and the triple-α resonance ^{12}C*, which open nucleosynthesis beyond Li, the maximum at ^{56}Fe, which stops stellar burning by heavy-ion fusion, and the s-process maxima at $A \simeq 90$, 140 and 208 corresponding to the $N = 50$, 82 and 126 closed shells (see figure 17).

Traditionally nuclear masses are described empirically, but more recently microscopically based mass formulae have become available. Empirical mass formulae based on the nuclear liquid-drop model have been improved by introducing phenomenologically microscopic corrections if needed to describe experimental data. Thus the macroscopic–microscopic mass formula, whose latest and most sophisticated version, the finite range droplet model (FRDM), has become the tool of choice and has been applied to many astrophysical problems, including r-process nucleosynthesis. As a number of merit, the FRDM mass formula reproduces the known masses of about 2000 nuclei with an rms deviation of about 0.7 MeV [57].

The advances of (non-relativistic and relativistic) mean-field models and the progress in computational power have made it possible to develop microscopic mass models and apply them globally to the entire nuclear chart. The break-through of such microscopically founded models came with the development of the extended Thomas–Fermi plus Strutinsky integral (ETFSI) method [69] (see section 2.3). It reproduces the known nuclear masses as well as the

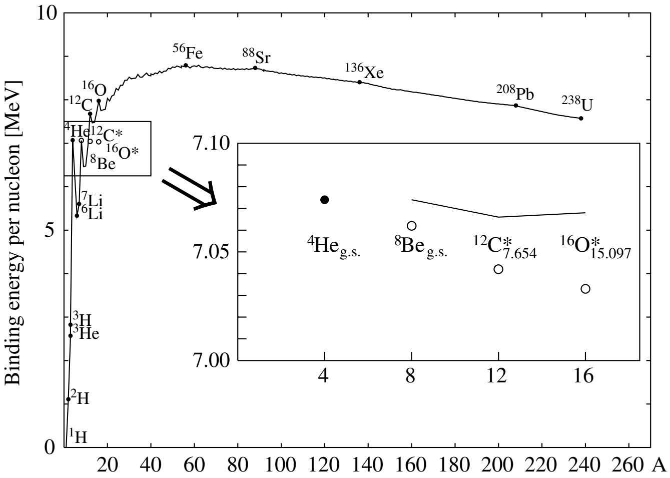

Figure 13. Binding energy per nucleon for nuclei close to stability. For ^{8}Be, ^{12}C and ^{16}O also the resonance ground state, the triple-α 0_2^+ state at 7.654 MeV (^{12}C*) and the 0_6^+ state at 15.097 MeV (^{16}O*) are shown. Resonances are marked as open circles. The inset enlarges the multiple-α states, the line marks the n–α thresholds ($n = 2$–4).

FRDM approach, and has become the other standard model to produce the unknown nuclear masses in r-process simulations.

Further progress in the development of microscopic mass formulae are mass compilations based on the shell model making use of monopole-driven shell evolution and A-scaling laws to warrant saturation [74], and more recently on HFB calculations with Skyrme forces fitted globally to nuclear masses. It was shown that the known nuclear masses can be reproduced with the same overall quality as by the best FRDM fits. The microscopic approach has been extended to a full Hartree–Fock–Bogoliubov treatment of the masses, assuming a specifically designed Skyrme force and a δ pairing force [73, 150, 151]. Critical recent reviews of the status of nuclear masses both experimentally and theoretically can be found in [66, 152–154].

While the various nuclear mass models agree quite well with the known nuclear masses, they disagree among each other in their predictions for nuclei far-off stability, for example, for the very neutron-rich nuclei in r-process simulations. The differences in mass predictions between the FRDM model and one of the microscopic approaches is illustrated in figure 2 of [2]. In the region of the nuclear chart relevant for the rp- and r-processes deviations amount up to 3 MeV. Obviously, the models treat the isospin degrees of freedom quite differently. The conclusion from this comparison, i.e. the quite distinct differences in mass, is the need for more experimental data far-off stability which will come from the next generation of radioactive ion-beam facilities like FAIR at GSI, SPIRAL 2 at GANIL and RIBF at RIKEN. To illustrate the shell structure in neutron-rich nuclei in figure 5 the S_{2n} values as defined in section 2.4, which provide a measure for the shell gap, are shown for $Z = 30$–70 and $N = 40$–140, for four different mass formulae.

5.2. *Beta decay half lives*

The prediction of β- and particle-decay half lives is intimately related to decay Q-values inferred from mass predictions. The extreme sensitivity is determined by the strong decay-energy dependence of the phase space function $f \sim E_\beta^5$ in β-decay and the penetrability in particle decay.

Experimental data so far play crucial roles in constraining and testing nuclear models, which are still essential to predict the bulk of half lives required in r- and rp-process simulations. It is generally assumed that the half lives are determined by allowed GT transitions. Contributions of first-forbidden (FF) transitions to r-process half lives have been discussed in selected cases [155–157]. The β decay half lives due to the E_β^5 dependence only probe the weak low-energy tail of the GT distributions, where only a few percent of the $3(N-Z)$ Ikeda sum rule [158] are exhausted. Therefore a correct description of the detailed low-energy GT distribution and its relative energy scale to the parent nucleus are an indispensable prerequisite for an adequate modeling of the nucleosynthesis paths far-off stability. Most estimates of the half lives of r- and rp-process nuclei are so far based on a combination of global mass models and the quasiparticle random phase approximation (QRPA) to calculate the GT matrix elements. Examples of these models are the FRDM/QRPA [57] and the ETFSI/QRPA [75]. Recently, calculations based on the self-consistent Hartree–Fock–Bogoliubov plus QRPA model (HFB-QRPA) became available for even–even r-process waiting point nuclei near the magic neutron numbers $N = 50$, 82 and 126 [76]. Near closed neutron shells half lives of r-process waiting point nuclei were calculated by shell-model calculations [159, 160]. Near ^{100}Sn shell model predictions of masses and β^+ decay half lives are at hand for rp-process nuclei [4, 161]. A compilation of stellar weak interaction rates for rp-process studies is available in [162].

The QRPA approach based on the density functional of Fayans (DF-QRPA) [163] has been recently proven to yield a quite convincing consistent description of the half lives of nuclei in various regions of the nuclear chart, including nuclei in the vicinity of the r-process waiting points associated with the neutron magic numbers $N = 50$, 82 and 126 [77,164]. As an example half lives for the $N = 82$ isotones, the chain of Cd isotopes including the waiting point nucleus ^{130}Cd and for the $N = 126$ isotones are shown in figure 23, 24 and 26, respectively, and discussed in section 10. The DF3 + CQRPA approach considers consistently allowed and FF contributions to the half lives. It is found that allowed transitions clearly dominate the half lives for the r-process nuclei close to the $N = 50$ and 82 waiting points. This is different from the recent conclusions based on the FRDM/QRPA model, where FF contributions, obtained within the gross theory, yield a significant reduction of the half lives. For the nuclei close to $N = 126$, both models (FRDM/QRPA and DF3 + CQRPA) predict forbidden transitions to be important for the description of the half lives and the β-delayed emission probabilities.

While the β-decay half lives set the time scale, the competition between β-delayed γ- and particle emission determine the particle branching. The branching ratios due to the strong energy dependence of barrier penetration, which favors ground state decays, are mainly determined by the decay energy, which can be inferred from mass predictions. In selected cases as in regions of shape coexistence structure effects will influence the decay widths via spectroscopic factors. In global calculations identical shapes are routinely assumed for parent and daughter states. Similarly in close-to-magic nuclei with isolated high-spin intruder orbitals the particle branch might be hindered by the centrifugal barrier. For heavy nuclei beyond $Z = 84$ some final states populated by β-decay can also decay by fission [165] causing a major redistribution of the flux. The relevant beta-delayed fission probabilities depend sensitively on the modeling of the fission barriers [166–169].

5.3. Nuclear level densities

In various astrophysical elemental synthesis processes, like the r- and rp-process [165], theoretical nuclear reaction rates are often based on statistical approaches. This requires the knowledge of the nuclear level density at modest excitation energies, typically around the neutron and proton thresholds. Conventionally, nuclear level densities have been described in these astrophysical studies by the backshifted Fermi gas model of Gilbert and Cameron [170]. This model extends the non-interacting Fermi gas model of Bethe [171] by considering pairing among like nucleons via a backshift of the excitation energy E. Thus one has [165]

$$\rho(U) = \frac{\sqrt{\pi}}{12a^{1/4}} \frac{\exp 2\sqrt{aU}}{U^{5/4}}, \qquad U = E - \Delta, \tag{8}$$

where Δ is the backshift. The level density parameter a incorporates a dependence on deformation and energy [172] and it is often determined by comparison to data. It was shown [173] that such an approach gives quite satisfactory agreement to experimental data.

There have been several attempts to derive $\rho(E)$ from microscopic models; for a review see for example [165, 174]. In recent years it has become possible to calculate level densities microscopically, based on the shell model Monte Carlo (SMMC) method which takes the dominant correlations among nucleons at low and modest excitation energies into account and can be used in model spaces far larger than those accessible to conventional shell model methods [48, 49].

First SMMC level densities have been reported in [175, 176] for even–even nuclei. The first SMMC study for odd-A and odd–odd nuclei was presented in [177]. In the meantime the SMMC approach was applied to many nuclei in the mass range $A \sim 55$–70, using a model space of 30 active orbitals for protons and neutrons (complete pfg$_{9/2}$ space). It is stated that in all cases, the SMMC level densities agree quite well with a backshifted Fermi gas model with constant parameters Δ and a. The SMMC approach was extended to study the parity-dependence of the level density for even–even nuclei [178] and recently also for odd-A nuclei [179]. Astrophysical applications usually assume an equal distribution of even and odd parities. Importantly, the SMMC level densities show that such an equality is not necessarily achieved at the low excitation energies of relevance for r-process nucleosynthesis. Based on the SMMC results and assuming BCS pairing, Alhassid *et al* have given a rather simple prescription on how to determine the ratio of even-to-odd parity level densities [180]. This approach has recently been extended, based on the energy dependence of SMMC pairing correlations, and is now being implemented in r-process rate predictions [181]. Attempts to derive the angular momentum dependence of the level density microscopically have been reported by [182, 183]. Experimentally level densities for distinct angular momenta and parity can be derived by wavelet analysis of precision electromagnetic strength function data [184]. The SMMC method is also well suited to calculate the temperature dependence of the various correlations and their effect on the level density. For example, the isovector pairing correlations decrease with increasing temperature, resulting also in a pronounced peak in the specific heat for even–even nuclei at temperatures around $T = 0.7$ MeV [186]. Relatedly SMMC level densities for even–even nuclei can be well approximated by a backshifted Fermi gas ansatz, however, with an energy-dependent backshift parameter the energy dependence of which closely follows the one of the pair correlations (see figure 14) [185].

6. Gamow–Teller distributions and weak interaction rates

Nuclear reactions mediated by the weak interaction play important roles in many astrophysical objects. Quite often these processes involve rather low momentum transfer and are dominated by allowed transitions. Typical examples are the electron captures occuring during the final core collapse of massive stars or neutrino–nucleus reactions as part of explosive nucleosynthesis during a supernova explosion. Yet no experimental data for neutrino–nucleus cross sections as a function of neutrino energy exist. Moreover, weak interaction processes like electron captures during a supernova collapse occur at extreme conditions of densities and temperatures, making

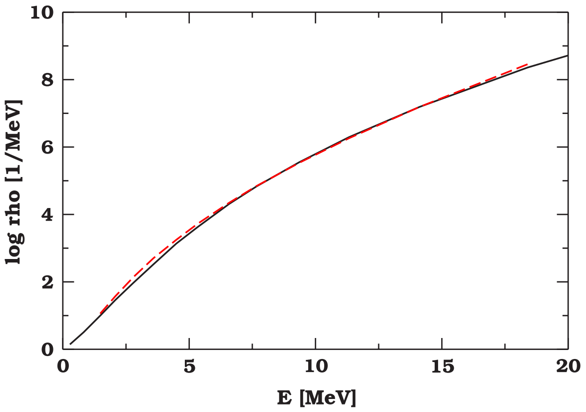

Figure 14. SMMC level density for ^{72}Ge (——) compared to a backshifted Fermi gas ansatz (- - - -). The energy dependence of the backshift parameter is identified with those of the pairing correlations calculated within the same SMMC approach (from [185]).

a direct measurement in the laboratory impossible and hence requiring theoretical modeling. Nevertheless the determination of such weak-interaction rates has strongly benefitted from the development of novel charge-exchange techniques which allow the precise measurement of GT_- (where a neutron is changed into a proton like in charged-current (ν_e, e^-) reactions) and GT_+ (here a proton is changed into a neutron as in electron capture) Gamow–Teller strength functions via $(^3\mathrm{He}, t)$ and $(d, ^2\mathrm{He})$ reactions [187–189]. These data serve as constraints for large-scale shell model calculations which, in fact, have been proven to describe the GT distributions for pf-shell nuclei, which are very abundant in the early collapse, quite well [190] (see figure 15). As the shell model also reproduces the low-energy spectrum of nuclei sufficiently well, it has been the method of choice for the calculation of the weak interaction rates on nuclei with mass numbers $A = 45$–65 under collapse conditions [192] improving the pioneering work of Fuller, Fowler and Newman [193]. In figure 16 recently measured GT distributions are compared with shell model predictions [192] and to the centroids assumed in [193]. For heavier nuclei the electron capture rates have been derived on the basis of the SMMC method [194] showing that due to nucleonic correlations and finite temperature effects the rates are significantly less Pauli-suppressed than expected on the basis of the independent particle model and assumed in supernova simulations.

The shell model capture rates have significant impact on collapse simulations. In the presupernova phase (at densities $\rho < 10^{10}\,\mathrm{g\,cm^{-3}}$) the captures proceed slower than assumed before and for a short period during silicon burning β-decays can compete [199, 200]. As a consequence, the core is cooler, more massive and less neutron rich before the final collapse. During the final collapse capture on nuclei dominates over capture on free protons. The changes compared with the previous simulations are significant [194, 201, 202]. Importantly the shock is now created at a smaller radius with more infalling material to traverse, but also the density, temperature and entropy profiles are strongly modified [201].

Recently inelastic neutrino–nucleus scattering has been included for the first time in supernova simulations. The relevant cross sections have been calculated based on large-scale shell model calculations for the allowed GT transitions and within the random phase approximation for forbidden transitions [203], taking special care of finite temperature effects [204, 205]. At low and modest neutrino energies E_ν the cross sections are dominated by GT_0 contributions for which the shell model has been validated by detailed comparison to precision

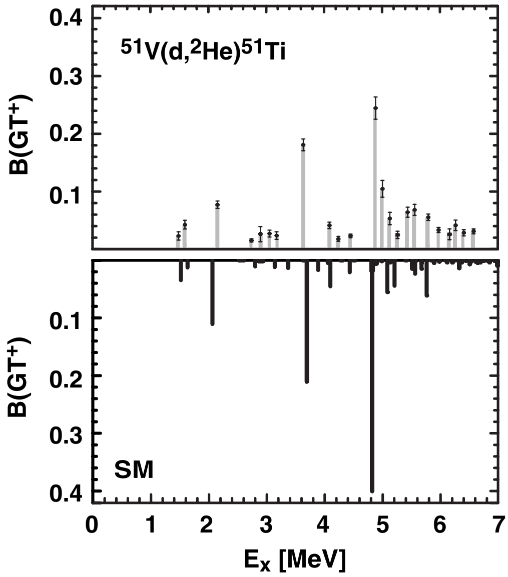

Figure 15. Comparison of the measured ^{51}V(d,^{2}He)^{51}Ti cross section at forward angles (which is proportional to the GT$_+$ strength) with the shell model GT distribution in ^{51}V (from [191]).

$M1$ data derived from electron scattering on spherical nuclei which are mainly due to the same isovector response [206].

Although inelastic neutrino–nucleus scattering contributes to the thermalization of neutrinos with the core matter, the inclusion of this process has no significant effect on the collapse trajectories. However, it increases noticeably the opacity for high-energy neutrinos after the bounce [207, 208]. As these neutrinos excite the nuclei, they are down-scattered in energy, in this way significantly reducing the high-energy tail of the spectrum of emitted supernova neutrinos. This makes the detection of supernova neutrinos by earthbound detectors more difficult, as the neutrino detection cross section scales with E_ν^2.

Charged-current (ν_e, e$^-$) reactions might occur during r-process nucleosynthesis [209, 210] in a supernova or are important for the observation of supernova neutrinos by earthbound detectors. In both cases the neutrino spectrum is approximately given by a Fermi–Dirac distribution with zero chemical potential and a temperature of about $T = 4$ MeV. Thus, for the neutron-rich r-process nuclei the neutrinos are energetic enough to excite the isobaric analog state by Fermi transition or the centroid of the GT strength distribution in the daughter nucleus. Moreover, the total GT$_-$ strength is basically given by the Ikeda sum rule in neutron-rich nuclei, as the GT$_+$ strength nearly vanishes. Thus, (ν_e, e$^-$) reactions do not require the detailed reproduction of the GT$_-$ strength distribution and are often already reasonably well described by many-nucleon methods like the RPA which fulfills the Ikeda sum rule and gives a good account of the GT centroid energy [211, 212]. The RPA has also been used to derive the neutrino-induced cross sections for supernova detector materials like ^{12}C, ^{16}O, ^{40}Ar [213] and ^{208}Pb [214, 215, 216, 217], while the cross sections for ^{56}Fe have been determined by a combination of shell model for allowed transitions and RPA for forbidden transitions [218].

The low-energy GT$_-$ tails are essential for the calculation of β^- half lives. Due to its sensitivity to nuclear correlations it is usually quite difficult to reproduce in detail. While the shell model might be the method of choice, its application to medium-mass and heavy

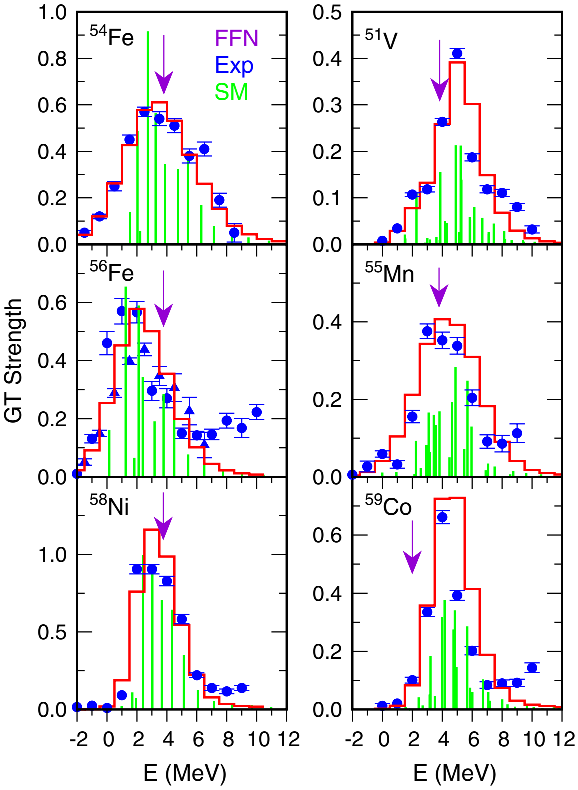

Figure 16. Experimental [195–197] and shell model Gamow–Teller distribution for key nuclei in the early stage of the core collapse of a massive star [192, 198]. The vertical bars indicate the centroids assumed in [193].

open-shell nuclei requires model spaces far beyond the feasibility of present computational possibilities. Hence the half lives for the many r-process nuclides, which are also still out of experimental reach, have to be modeled by empirical, globally applicable models (see sections 2.3 and 5.2).

7. Nucleosynthesis from ^{4}He to ^{56}Ni

The nucleosynthesis beyond ^{4}He as formed in the Big Bang is hampered by the $A = 5{,}8$ stable mass gaps. This can be overcome both in hydrostatic and explosive stellar burning via the triple-alpha process and successive fusion, αp- and rp-processes. The latter is discussed in section 11.1. In the presence of a sufficient reservoir of neutrons, as is the prerequisite for a successful r-process, the gap can also be bridged by the $\alpha + \alpha + \mathrm{n}$ three-body reaction. A decisive part in the underlying nuclear structure of fusion and α-particle induced reactions is played by the cluster structure of light nuclei. The importance of cluster structure in stellar nucleosynthesis is governed by the large binding energy of the α particle and of $N = Z$ even–even nuclei up to ^{28}Si as indicated by the peak structure in the binding energy per nucleon shown in figure 13. It is also demonstrated by the small α separation energies for CS + α nuclei as shown in figure 9 of [2]. Key applications for cluster models are stellar helium burning, stellar neutron sources, the αp-process and α dissociation of rp nuclei, stellar ^{12}C burning [2] and, in the future, (γ, α) reactions of importance for the p-process.

Stellar helium burning can only operate due to the pronounced alpha cluster structure in light $T = 0$ nuclei. The fact the ^{8}Be is unbound prevents a simple ^{4}He + ^{4}He fusion process and therefore a rapid processing of the available ^{4}He fuel and warrants the long lifetime of the stellar He-burning phase. On the other hand, the fact that ^{8}Be is only unbound by $Q_\alpha = 92$ keV leads, at sufficient stellar temperatures, to an equilibrium between formation of the α cluster ground state configuration of ^{8}Be and its back-decay to two single α particles. This equilibrium warrants a sufficient abundance of ^{8}Be in order to capture a third α particle forming the 0_2^+ compound state in ^{12}C at 7.654 MeV which lies only 287 keV above the α separation energy. This state subsequently decays to the ground state of ^{12}C by a cascade two-γ emission and by $e^+ - e^-$ pair-production. The cluster structure of the two states involved is evident from their binding energy per nucleon which is only marginally smaller than that of ^{4}He as shown in figure 13 (inset), i.e. the interaction between the ^{4}He constituents, composed of nuclear attraction and Coulomb repulsion, is small in comparison to their binding energy. The intrinsic structure of the ^{12}C* resonance (the Hoyle state) is still controversially discussed. The question whether it resembles a strongly deformed three-α-chain configuration [219] as illustrated in the Ikeda diagram [220] or a dilute gas-like Bose-condensate [138, 221] is still open experimentally and theoretically. It is intriguing to note, however, that a triangular arrangement of three-α clusters in the Hoyle state would have the threefold interaction energy of ^{8}Be which is reflected in the ratio 3.1 of the differences of the resonance energies above threshold (see inset in figure 13). Recent FMD results on this issue are discussed in section 4.2 and figure 10. A state of similar character is the 15.097 MeV resonance in ^{16}O lying 568 keV above the two-α threshold, i.e. a factor of 6.2 relative to the ^{8}Be energy difference (see insert in figure 13), which suggest a four-α structure for this ^{16}O resonance.

The explosive scenarios of x-ray bursts are driven by the thermonuclear runaway on the surface of an accreting neutron star. The runaway is triggered by the break-out reactions from the hot CNO cycle and the ignition of the triple α reaction that produces fresh material for the CNO cycle and the feeding of the rp-process [4, 222] (see section 11.1). The reaction link $^{4}\mathrm{He}(2\alpha,\gamma)^{12}C(\mathrm{p},\gamma)^{13}\mathrm{N}(\mathrm{p},\gamma)^{14}\mathrm{O}(\alpha,\mathrm{p})^{17}\mathrm{F}(\mathrm{p},\gamma)^{18}\mathrm{Ne}$ followed by the actual break-out sequence $^{18}\mathrm{Ne}(\alpha,\mathrm{p})^{21}\mathrm{Na}(\mathrm{p},\gamma)^{22}\mathrm{Mg}(\alpha,\mathrm{p})^{25}\mathrm{Al}\ (\mathrm{p},\gamma)^{26}\mathrm{Si}$ is called the αp-process because it is characterized by a sequence of α capture and proton capture reactions along the $T_z = -1$ line up to the Ca, Ti range. For $Z = 20$, 22 the Coulomb barrier prevents further α capture processing and the reaction flow towards higher masses takes place by rapid proton captures (the rp-process). The even–even $Z = N+2$ compound nuclei, like ^{18}Ne, ^{22}Mg, ^{26}Si, etc, again are expected to show a pronounced α cluster structure at the α threshold, which influences the α capture processes. This would guarantee a rapid break-out from the hot CNO cycles and an efficient conversion of ^{4}He fuel towards heavier mass nuclei. Experimental results are scarce and present reaction rates are based on Hauser–Feshbach estimates [4] which could be significantly enhanced in the presence of resonances with large α spectroscopic factors. While α capture starts the rp-process, α decay above the doubly magic nucleus ^{100}Sn due to low separation energies may terminate it (see figures 29, 31 and [223, 224]).

Carbon burning, the third stage in stellar burning, is determined by heavy-ion fusion. The most important reaction is $^{12}\mathrm{C} +^{12}\mathrm{C}$ with the fuel ^{12}C provided by the preceding helium burning. The reaction forms ^{24}Mg at high excitation energy well above the ^{12}C threshold. At these energies ^{24}Mg shows distinct molecular structure of the types ^{12}C–^{12}C, ^{16}O–^{4}He–^{4}He and ^{12}C–^{4}He–^{4}He–^{4}He [225, 226]. The molecular structure is supported by the rotational like increase of resonance spin with excitation energy. For the stellar reaction rate, however, the fusion cross section has to be extrapolated to the Gamow window. The total cross section is dominated by the α, p and (at higher energy) n exit channels from the ^{24}Mg compound system which are comparable for the observed resonances so that a pronounced α or single-particle structure can be excluded [227]. Recently it has been proposed that heavy-ion fusion reactions might be suppressed at energies below the Coulomb barrier [228, 229]. If confirmed, this would have important impact on the extrapolations of data for the reactions relevant in carbon and oxygen burning towards the astrophysically effective energies.

Stellar neutron sources for the s-process operate at low temperature conditions ($T \approx 2 \times 10^8$ K) and are typically associated with (α, n) reactions in stellar helium and carbon burning. One of the three sources considered is the ^{22}Ne(α, n) reaction with a negative Q-value of -0.478 MeV, however, which requires higher temperature conditions ($T \approx 3 \times 10^8$ K). The other two sources ^{13}C(α, n) and ^{21}Ne(α, n) have positive Q-values but cannot be produced at conditions of stellar He burning as their efficiency is hampered by the unfavorable production abundance of the seed isotopes ^{13}C and ^{21}Ne. In the case of ^{13}C the lack of ^{10,11}B abundance is responsible, while the production of ^{21}Ne is hindered by a negative Q-value in the reaction chain, which is even more unfavorable than that for ^{22}Ne [2]. The production sequence of ^{22}Ne, ^{18}O(α, γ)^{22}Ne and presumably also the reaction rate of ^{22}Ne(α, n)^{25}Mg are dominated by the α cluster structure in the even–even $Z = N - 2$, $T_z = 1$ compound nuclei chain ^{18}O, ^{22}Ne and ^{26}Mg. Applying the Ikeda rule [220] to these systems, the compound nuclei are characterized by strong natural parity α cluster configurations near the α particle threshold in ^{22}Ne at 9.67 MeV, and ^{26}Mg at 10.615 MeV, which should give rise to strong resonances in the (α, γ) and the competing (α, n) reaction channel. Such resonances with large α spectroscopic factors have been observed for low-energy resonances in ^{14}C(α, γ)^{18}O [230] and ^{18}O(α, γ)^{22}Ne [231] but were also identified in ^{22}Ne(α, γ)^{26}Mg and the competing reaction channel ^{22}Ne(α, n)^{25}Mg [232–234].

8. The s-process

The impact of nuclear structure details on the s-process has been discussed in recent reviews [2, 5]. The s-process is driven by a weak neutron flux from the ^{13}C(α, n) and ^{22}Ne(α, n) reactions in stellar helium and carbon burning phases [235] and therefore has no significant impact on the stellar energy generation rate. It is the only nucleosynthesis process during stellar evolution that generates heavy elements above iron in significant abundances. Two different astrophysical s-process components associated with different sites, termed the weak and the main s-process have been proposed [236]. The weak s-process is responsible for neutron-induced nucleosynthesis up to the mass $A = 100$ region during helium and carbon core burning of massive stars, while the main s-process in the helium shell burning prior and during thermal pulsing in AGB stars provides sufficient neutron flux to extend neutron-induced nucleosynthesis up to the Pb–Bi region.

8.1. Magic numbers near stability

The characteristic abundance distribution of the s-process reflects the shell structure in heavy nuclei in a unique way (figure 17). The abundance peaks at $A \approx 90$, 140 and 200 are directly correlated with the $N = 50$, 82 and 126 shell closures for stable nuclei. Neutron capture cross sections on closed neutron shell nuclei are typically much lower than the ones for neutron capture on open-shell nuclei mainly because of the significantly lower Q-values for neutron capture on closed shell isotopes [57].

The natural endpoint of the s-process is associated with the α unbound isotopes ^{210}Po and ^{211}Po which are produced by β-decay of ^{210}Bi. This is again a signature of shell structure

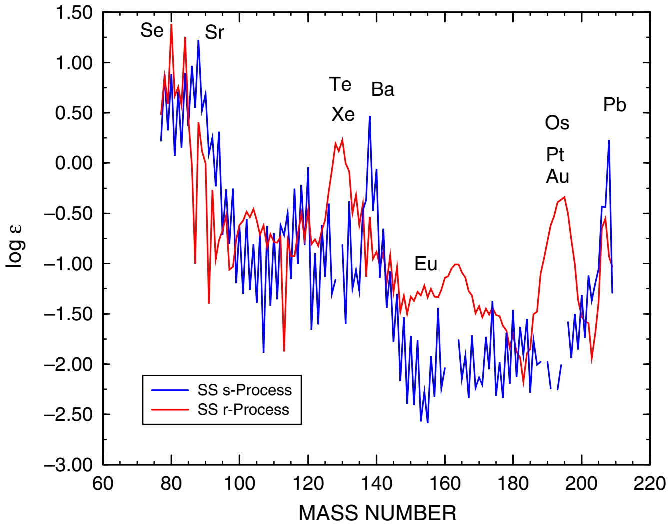

Figure 17. s-process and r-process abundances. Clear abundance peaks show up which can be associated with the $N = 50$, 82 and 126 closed shells at $A \simeq 90$ and 140 (s-process, black line) and $A \simeq 130$ and 195 (r-process, grey line) [2].

as nuclei above closed shells exhibit fast α decays due the favorable Q-values (see also sections 5.1, 7 and 11.2).

8.2. Branching points and excited states

As the α-induced neutron production is low due to the small α penetrability at stellar temperatures the neutron captures are in first approximation assumed to be much slower than competing β decay processes, which keeps the s-process path close to the line of stability. However, a more detailed view reveals that this assumption is not generally true. There are about 15–20 branching points along the s-process path where neutron capture competes with slow β decay. From the variation in time scales important information on the s-process site can be inferred such as temperature, neutron flux and density [237]. For certain nuclei on the s-process path, the β half life is strongly changed due to direct neutron-capture population or thermal excitation of isomeric states. Isomers are a very sensitive signature of nuclear structure. They originate from intruder single-particle states of opposite parity and/or large spin differences in near-sperical nuclei or from K isomerism in deformed regions. In either case γ decay is inhibited by high multipolarity and/or small transition energies. Examples of the first category are ^{121}Sn with a neutron $\nu d_{3/2}$ ground state and a $\nu h_{11/2}$ isomer (see ^{132}Sn figure 2(b)) studied in [238] and ^{85}Kr with a $\nu g_{9/2}$ ground state and a $\nu p_{1/2}$ isomer (see ^{78}Ni figure 2(b)), which is important for both the weak and main components of the s-process. To the second category belongs the prominent example of ^{176}Lu (with a ground state spin and half life of $I^{\pi} = 7^{-}$ and 4×10^{10} yr, respectively) which has an $I^{\pi} = 1^{-}$ isomeric state at an excitation energy of 123 keV which lives only 3.66 h. On the stellar s-process path both states are populated by ^{175}Lu(n, γ) with known partial cross sections. The s-process matter flow is then determined by the competetion of neutron capture on the ground state and β decay of the isomer. Furthermore, the ground and isomeric state couple in the stellar photon bath via the excitation of an intermediate state, leading to a matter flow from the isomer to the ground state, which is very temperature dependent. Thus, it is possible from a detailed study of the s-process yield around the ^{176}Lu waiting point to determine the stellar temperature [239]. Another example for K-isomerism is the famous ^{180}Ta, which is the rarest isotope of Nature's rarest element, which is a similar temperature probe. ^{180}Ta is also the only nuclide which exists in an excited state (an $I^{\pi} = 9^-$ isomer at the excitation energy 75 keV which lives for more than 10^{15} yr). The 1^+ ground state decays by electron capture to ^{180}Hf with a half life of about 8.2 h. While a direct electromagnetic decay of the isomer to the ground state is strongly K-forbidden, the isomer can decay via coupling to intermediate states in finite temperature environment. It was found that, under s-process conditions, the half life of ^{180}Ta is reduced by more than 15 orders of magnitude compared with the one of the isomeric state [240].

8.3. Neutrino nucleosynthesis of s-process elements

We note that ^{180}Ta, like ^{11}B, ^{19}F and ^{138}La, can also be produced by neutrino-induced spallation on more abundant nuclei (^{12}C, ^{20}Ne, ^{138}Ba and ^{180}Hf) in a core-collapse supernova, when the neutrinos, produced by cooling of the proto-neutron star, pass through the outer layers of the star [241, 242]. Interestingly the production of ^{11}B and ^{19}F is due to neutral current reactions $(\nu_x, \nu_x' \mathrm{p})$ and $(\nu_x, \nu_x' \mathrm{n})$, where ν_x is a short for ν_μ, ν_τ neutrinos and their anti-particles, which are more energetic than ν_e and $\bar{\nu}_\mathrm{e}$ neutrinos [243], while ^{138}La and ^{180}Ta are made via $(\nu_\mathrm{e}, \mathrm{e}^-)$ charged-current reactions. Hence neutrino nucleosynthesis probes the distributions of the five neutrino species which have not been observed from the supernova SN1987A by the Cerenkov detectors, which were only sensitive to $\bar{\nu}_\mathrm{e}$ neutrinos. Recent stellar nucleosynthesis calculations find that inclusion of the neutrino process is required to produce the nuclides ^{11}B, ^{19}F, ^{138}La and ^{180}Ta in solar abundances. This makes neutrino nucleosynthesis sensitive to the spectral properties of the different neutrino species and to neutrino-oscillations in the mantle of the star [242, 244, 245].

The needed $^{138}\mathrm{Ba}(\nu_\mathrm{e}, \mathrm{e}^-)^{138}\mathrm{La}$ and $^{180}\mathrm{Hf}(\nu_\mathrm{e}, \mathrm{e}^-)^{180}\mathrm{Ta}$ cross sections are now derived from the experimental GT_- distributions on ^{138}Ba and ^{180}Hf, which have been recently measured using the $(^3\mathrm{He}, t)$ charge-exchange technique [246].

9. Nucleosynthesis of medium-mass nuclei

Iron group nuclei are synthesized under conditions of large temperatures where nuclear statistical equilibrium is achieved during supernovae explosions (both core-collapse and thermonuclear) [247]. The production of different isotopes depends on the conditions achieved during the explosion and in particular on the neutron richness of the material, which, for core-collapse supernovae, is very sensitive to the spectrum and luminosities of neutrinos and antineutrinos emitted during the supernovae explosion [248, 249].

Traditionally, it was thought that elements heavier than iron are synthesized by the s-, p- and r-processes that are discussed later. However, recent observations at low metallicities tend to challenge this interpretation. First, the germanium abundance has been shown to track the iron abundance at low metallicities [250] indicating that at least at low metallicities some other process(es) are contributing beyond the traditional s- and r-processes.

Recent observations of metal-poor stars show that the relative abundance of elements heavier than $Z \simeq 56$, except for the radioactive actinides, exhibits a striking consistency with the observed solar abundances of these elements, while elements lighter than $Z = 56$ are underabundant relative to a scaled solar r-process pattern that matches the heavy element abundances [250,251]. These observations indicate that the astrophysical sites for the synthesis of light and heavy r-process nuclides are different [252, 253]. The exact site and operation for both types of r-process is not known. There are clear indications that the process responsible for the production of heavy elements is universal [254] while the production of lighter elements (in particular Sr, Y and Zr) has a more complex Galactic history [255].

Most of the stable neutron-deficient nuclei are thought to be produced in hot (supernova) environments by disintegration of pre-existing heavy elements due to black-body radiation photons. This process is denoted by the label p-process and can account for the solar abundances of heavy neutron-deficient nuclei, while the light ones like ^{92,94}Mo and ^{96,98}Ru are underproduced (see, e.g. [256, 257, 258] and figures 29 and 31). Currently, the mechanism for the production of the light p-nuclei is unknown. However, chemical evolution studies of the cosmochronometer nucleus ^{92}Nb [259] imply a primary supernova origin for the light p-nuclei.

Several recent studies [254, 260, 261] have suggested a new nucleosynthesis process denoted νp-process [260] that can explain the production of light p-nuclei and contribute to explaining the early galactic history of some medium-mass elements. In this process, proton-rich matter ejected during the supernova explosion expands and cools. During this expansion nuclei form at a typical distance of $\sim$1000 km from the proto-neutron star where antineutrino absorption reactions proceed on a time scale of seconds which is much shorter than the typical beta-decay half lives of the most abundant nuclei present (e.g. ^{56}Ni and ^{64}Ge). As protons are more abundant than heavy nuclei, antineutrino capture occurs predominantly on protons via $\bar{\nu}_e + p \rightarrow n + e^+$, causing a residual density of free neutrons of 10^{14}–10^{15} cm^{-3} for several seconds, when the temperatures are in the range (1–3) $\times 10^9$ K. These neutrons can easily be captured by neutron-deficient $N \sim Z$ nuclei (for example ^{64}Ge), which have large neutron-capture cross sections, by (n, p) reactions and successive proton captures allowing for matter flow to heavier nuclei. The amount of nuclei with $A > 64$ produced is then directly proportional to the number of antineutrinos captured.

The nuclear structure aspects relevant for the nucleosynthesis of medium-mass nuclei are: (i) the existence of a $N = 40$ (sub)shell in ^{68}Ni and below $Z = 28$ and (ii) the persistence of the $Z = 28$, $N = 50$ proton and neutron shell gaps in ^{78}Ni. The heaviest nucleus with doubly magic features and an ls-closed HO neutron shell is ^{68}Ni at $N = 40$. The neutron shell gap has been discussed in many publications and was found to be small and to disappear at more than two nucleons distance from ^{68}Ni [7, 140, 262, 263]. This can be understood within the framework of the scenarios shown in section 2.4 and figure 7. Towards the neutron-rich Ca isotopes the removal of $\pi f_{7/2}$ protons will release the $\nu f_{5/2}$ neutrons to close the $N = 40$ gap. Experimentally deformation was observed already in ^{66,67}Fe [262, 264] and ^{64}Cr, the latter corresponds to ^{32}Mg one major shell lower. The $N = 40$ gap according to this scenario would shift to $N = 32$, 34 in the Ca isotopes. Recently relativistic Coulomb excitation experiments were performed on the $N = 32$, 34 Cr [265] and Ti [266] isotopes. In both cases clear evidence for a $N = 32$ subshell was observed in the $B(E2, 2^+ \rightarrow 0^+)$ transition strength, which corroborates an earlier conclusion from excited states in ^{54}Ti [267]. On the other hand, evidence for the $N = 34$ closure was not seen and it may develop only in the Ca isotopes.

10. The r-process

The r-process is responsible for the synthesis of approximately half of the nuclei in nature beyond Fe [147, 148, 268]. It requires neutron densities which are high enough to make neutron capture faster than β decay even for neutron excess nuclei 15–30 units from the stability line. These conditions enable the production of neutron-rich nuclei close to the dripline via neutron capture and (γ, n) photodisintegration during the r-process. Once the neutron source ceases, the progenitor nuclei decay either via β^- or α emission or by fission towards stability and form the stable isotopes of elements up to the heaviest species Th, U and Pu. Due to the relatively

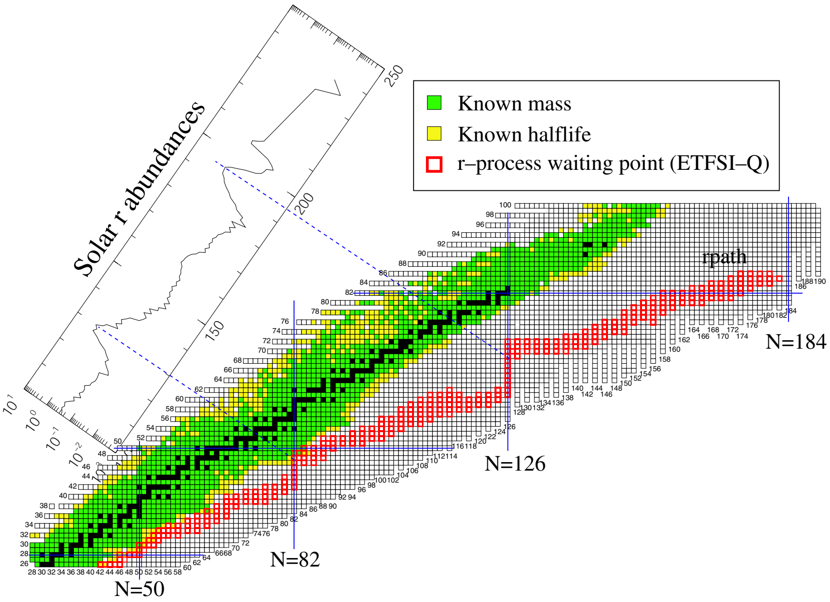

Figure 18. The figure shows the range of r-process paths, defined by their waiting point nuclei. After decay to stability the abundance of the r-process progenitors produce the observed solar r-process abundance distribution. The r-process paths run generally through neutron-rich nuclei with experimentally unknown masses and half lives. In this calculation a mass formula based on the ETFSI model and special treatment of shell quenching [79] has been adopted (courtesy of Kratz and Schatz).

small neutron separation energies in nuclei with $N_{\mathrm{mag}} + 1$, where $N_{\mathrm{mag}} = 50, 82, 126, 184$, the r-process flow at magic neutron numbers comes to a halt requiring several β decays to proceed. As the half lives of these magic nuclei are large compared with ‘regular’ r-process nuclides, they determine the dynamical time scale of the r-process. Furthermore, much matter is accumulated at these ‘waiting points’ resulting in the observed peak structure in the r-process abundance distribution. As far from stability the masses A with magic neutron numbers are smaller, these abundance peaks are shifted relative to the s-process peaks (see figures 17 and 18).

The astrophysical sites for the r-process are still heavily debated. Depending on the thermodynamical conditions and in particular the entropy they can be classified in low-entropy and high-entropy sites. Low-entropy sites include the decompression of cold neutron star material [269], prompt explosions of ONeMg cores [270] and jets from accretion disks [271]. The neutrino-driven wind from the nascent neutron star in a core-collapse supernova [272,273] constitutes the typical example of an r-process in high entropy environments.

Currently, the neutrino-driven wind is the favored scenario for r-process nucleosynthesis. In this environment, neutrino emission from the cooling of the just formed neutron star produces an outflow of baryonic matter. This matter expands rapidly and cools, once charged-particle reactions freeze-out (alpha-rich freeze-out), elements heavier than iron are produced. For sufficiently large neutron excesses and/or entropies a large abundance of free neutrons is still available that can be captured on these heavy nuclei (the ‘seed’) producing an r-process [274, 275].

The r-process occurs under conditions for which an equilibrium between neutron captures and photodissociations is achieved as long as neutrons are available [165]. In this case the abundances in an isotopic chain are given by the simple relation

$$\frac{Y(Z, A+1)}{Y(Z, A)} = n_{\mathrm{n}} \left(\frac{2\pi\hbar^2}{m_{\mathrm{u}}kT}\right)^{3/2} \left(\frac{A+1}{A}\right)^{3/2} \frac{G(Z, A+1)}{2G(Z, A)} \exp\left[\frac{S_{\mathrm{n}}(Z, A+1)}{kT}\right], \tag{9}$$

where n_{n} is the neutron number density, T is the temperature, m_{u} is the atomic mass unit, G is the partition function and S_{n} is the neutron separation energy. For each isotopic chain, the above equation defines a nucleus that has the maximum abundance and which is normally known as waiting point nucleus as the flow of neutron captures 'waits' for this nucleus to beta-decay. The set of waiting point nuclei constitutes the r-process path. The maximum of the abundance distribution can be determined setting the left-hand side of equation (9) to 1, which results in a value of S_{n} that is the same for all isotopic chains for a given neutron density and temperature

$$S_{\mathrm{n}}(\mathrm{MeV}) = \frac{T_9}{5.04}\left(34.075 - \log n_{\mathrm{n}} + \frac{3}{2}\log T_9\right), \tag{10}$$

where T_9 is the temperature in units of 10^9 K and n_{n} is the neutron density in cm^{-3}. Equation (10) implies that the r-process proceeds along lines of constant neutron separation energies towards heavy nuclei. Figure 18 shows a range of r-process paths for a set of dynamical astrophysical conditions. After decay to stability the progenitor abundances produce the shown solar r-process abundance distribution. It is obvious that from the $A = 50$–80 seed region on the lower left side towards heavy nuclei the closed neutron shells at $N = 50$, 82 and 126 determine the evolution of the process and the peak structure in the distribution. Magic proton and neutron numbers are indicated by solid lines.

10.1. The $N = 50$ shell near ^{78}Ni

On the neutron-rich side of the valley of stability ^{78}Ni, the doubly-magic $N = 50$ isotone of ^{100}Sn has been the subject of numerous experimental studies with respect of the persistence of the $N = 50$ shell and its relevance for the astrophysical r-process path. Early β-decay results seem to indicate a substantial shell quenching [276], while in-beam experiments on $N \sim 50$ Ge–Se isotopes [277] and isomer studies following fragmentation [278–282] give evidence for the persistence of the $N = 50$ shell. In β-decay of odd-mass Ni isotopes a strong monopole shift of the $\pi 0\mathrm{f}_{5/2}$ level in Cu isotopes is observed when the $\nu 0\mathrm{g}_{9/2}$ shell beyond N=40 is getting filled [7, 89, 283]. This is decisive for both the $Z = 28$ and $N = 50$ shell gaps in ^{78}Ni which are determined by the interaction of the spin-flip $\Delta l = 1$ $\pi 0\mathrm{f}_{5/2}\nu 0\mathrm{g}_{9/2}$ pair of nucleons. In Ni isotopes ($Z = 28$) beyond $N = 40$, due to filling of the $\nu 0\mathrm{g}_{9/2}$ shell, the $\pi 0\mathrm{f}_{5/2}$ orbit is bound more strongly than the adjacent $\pi 1\mathrm{p}_{3/2}$ and $\pi 0\mathrm{f}_{7/2}$ orbits and eventually crosses the $\pi 1\mathrm{p}_{3/2}$ to enter the shell gap. Along $N = 50$ the removal of $\pi 0\mathrm{f}_{5/2}$ protons will release the $\nu 0\mathrm{g}_{9/2}$ stronger than $\nu 1\mathrm{d}_{5/2}$ which will reduce the gap.

In figure 19 (lower panel) the extrapolation of the shell gap along the $N = 50$ line from ^{100}Sn to ^{78}Ni for successive removal of the $\pi 0\mathrm{g}_{9/2}$, $\pi 1\mathrm{p}_{1/2}$, $\pi 1\mathrm{p}_{3/2}$ and $\pi 0\mathrm{f}_{5/2}$ protons is shown for different experimentally known starting points at $Z = 50$, 40 and 38. Monopoles inferred from a realistic 1p, 0f, 0g interaction [29] were used for $\nu 0\mathrm{g}_{9/2}$, whereas the unknown monopoles involving the $\nu 1\mathrm{d}_{5/2}$ were taken from a 1d, 0g, 1f interaction above ^{132}Sn after $A^{-1/3}$ mass scaling. The experimental gaps at $Z = 50$, 40 and 38 are well reproduced, and the $N = 50$ gap at $Z = 28$ is extrapolated to be ~3.5 MeV, which is reduced by ~3.0 MeV compared with ^{100}Sn (see figure 2(*a*)) but still maintains a shell closure. Between the proton subshells the experimental gaps are smaller due to core excitations and configuration mixing. Therefore it should be noted that the extrapolation of the $N = 50$ shell gap is only realistic

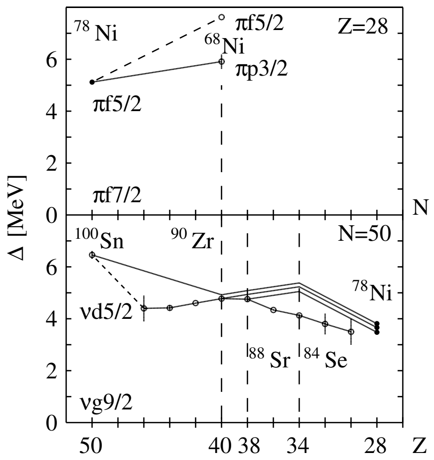

Figure 19. Evolution of the $Z = 28$ (upper panel) and $N = 50$ (lower panel) shell gaps towards ^{78}Ni. Measured and extrapolated values are indicated by filled and open symbols [90]. Note that the Z and N abscissae are running in decreasing sequence.

for the closed proton shells at $Z = 50$, 40, 38 and 28. The shell gap is defined here as the energy difference between the highest hole ($\nu 0g_{9/2}$) and the lowest particle ($\nu 1d_{5/2}$) levels. In the upper panel the evolution of the proton gap between $\pi 0f_{7/2}$ and $\pi 0f_{5/2}$ (dashed line), respectively $\pi 1p_{3/2}$ is shown, where the latter is the lowest-lying particle orbit at $N = 40$. Therefore the effect is not as dramatic as along $N = 50$. From $N = 40$ to $N = 50$ the gap is reduced by ~1 MeV to ~5 MeV, i.e. we come to the conclusion that the ^{78}Ni shell closure is preserved in agreement with experimental evidence on the persistence of $\nu 0g^2_{9/2}$ seniority isomerism from $N = 42$ (^{70}Ni) to $N = 48$ (^{78}Zn,^{76}Ni) [278–282] and the $N = 50$ shell strength in Ge isotopes [277].

The inferred ^{78}Ni shell gaps along with the recently determined empirical $T = 1$ interaction and single-particle (hole) energies for the $N = 50$ isotones and Ni isotopes [12] are shown in figure 2(*b*) and provide a benchmark for tuning the monopole interaction in the ^{48}Ca to ^{78}Ni model space. The puzzling disappearance of the $I^{\pi} = 8^+$ isomers in the midshell nuclei ^{72,74}Ni [284], which is intimately connected to the low $I^{\pi} = 2^+$ excitation energies [7,13,285], is nicely reproduced by the new $T = 1$ empirical interaction for $Z = 28$ [12] and has no relation to deformation.

Beta-decay half lives are decisive at neutron shell closures where the r-process path is shifted towards stability and therefore the slowest decay rates are encountered. Slow β-decay rates are the bottle-necks that control the synthesis of all heavier elements and serve as benchmarks to constrain the astrophysical parameters of the r-process. They also determine the local abundance pattern as fast (slow) rates lead to low (high) abundance [3]. In the $Z \simeq 28$, $N \simeq 50$ region β-decay is governed by the allowed $\nu 0f_{5/2,7/2} \rightarrow \pi 0f_{7/2,5/2}$ and $\nu 0g_{9/2} \rightarrow \pi 0g_{7/2}$ GT transition, while first-forbidden (FF) decays stem from $\nu 0g_{9/2} \rightarrow \pi 0f_{7/2}$, $\nu 0f_{5/2} \rightarrow \pi 1d_{5/2}$ and across the $N = 50$ shell $\nu 1d_{5/2} \rightarrow \pi 0f_{5/2}$ transitions. All these orbitals are affected by the shell evolution scenario discussed above. Recent results for β-decay half lives and β-delayed neutron emission probabilities applying the DF3+CQRPA model [164] can be summarized as follows.

- A very good agreement with experimental half lives is obtained.
- The Ni isotopes for $N \leqslant 50$ are well described with GT transitions only, while FF decays become important for $N \geqslant 50$.

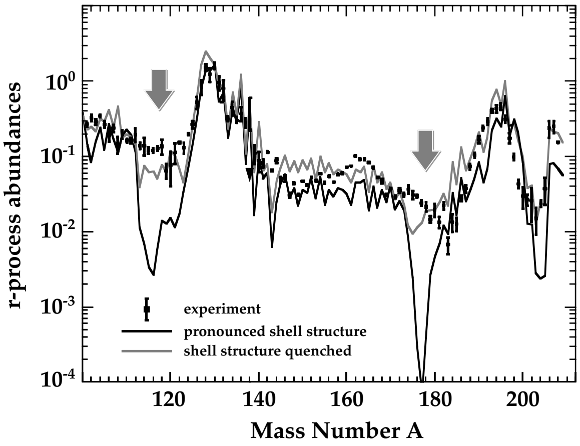

Figure 20. Solar r-process abundance distribution compared with two r-process calculations assuming pronounced (black line) and quenched $N = 82$ shell gap (grey line). The dips below the $A \simeq 130$ and 195 peaks are filled for the latter model [84].

- This is at variance with earlier work that FF transitions are important for $N \leqslant 50$ [286] and the claim that only shell quenching can explain the half lives of these nuclei [287].

These results support the persistence of both the $Z = 28$ and $N = 50$ shell gaps in ^{78}Ni and the r-process path evolution as shown in figures 18 and 19.

10.2. The $N = 82$ *shell below* ^{132}*Sn*

The $N = 82$ shell gap and its evolution with neutron excess plays a very important role for r-process nucleosynthesis studies. For the high-entropy conditions (i.e. large number of neutrons available after the alpha-rich freeze-out) that allow for the synthesis of nuclei with $A = 195$ and beyond the r-process path initially proceeds very far from stability due to the large initial abundance of neutrons. In this case a reduced (quenched) shell gap far from stability translates in a faster flow of the initial abundance distribution, that peaks around $A \sim 90$, through the $N = 82$ nuclei, a faster decrease in the neutron abundance and a reduced amount of fission during the r-process (see discussion in section 10.4).

For the conditions responsible for the synthesis of nuclei below $A = 195$ the presence of a strong shell gap far from stability has been associated with the appearance of an abundance trough around $A \simeq 115$ (see figure 20 and [84, 288]) that is cured by a mass model with a quenched shell gap far from stability [84, 289]. The abundance troughs at $A \simeq 115$ and $A \simeq 175$ in figure 20 were originally identified in r-process calculations that used the waiting point approximation (i.e. $(n, \gamma) \rightleftarrows (\gamma, n)$ equilibrium) and assumed an instantaneous freeze-out [288]. Under the same assumptions and using a mass model with quenched $N = 82$ and $N = 126$ neutron shell gaps the abundance troughs were filled [84]. Later calculations [86] which considered astrophysical conditions similar to the ones achieved in neutrino-driven winds showed that the $A \simeq 175$ trough could be filled even for mass models with large shell gaps far from stability once freeze-out effects were considered (i.e. taking into account that neutrons emitted during the decay of the r-process matter back to the stability of the r-process matter are captured again). However, the $A \simeq 115$ trough persisted in these calculations.

The presence of a quenched shell gap is associated with the 'saddle point behavior' seen in the two-neutron separation energies for $Z \approx 40$ and $N = 75$–82 in the mass models ETFSI-1

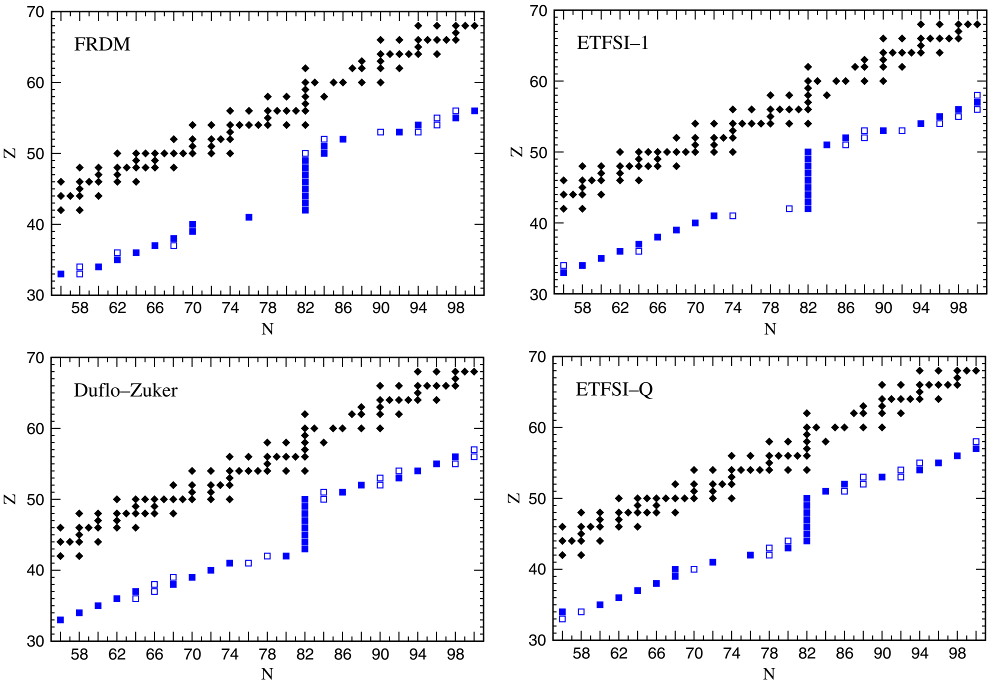

Figure 21. The r-process paths in the $A = 80$–150 mass region obtained assuming equilibrium between neutron capture and photodissociation (equation (9)) for the four mass models shown in figure 5 and using a temperature of $T_9 = 1.35$ and neutron density of 4.5×10^{21} cm^{-3} [289] that correspond to a two-neutron separation energy of 6.76 MeV according to equation (10). Nuclei in the valley of stability are shown as diamonds. Nuclei present during the r-process are shown as full squares (nuclei with the maximum abundance in an isotopic chain) or open squares (nuclei with an abundance larger than 10% of the population of their isotopic chain).

and FRDM (see figure 5). As discussed above (see equation (10)) the r-process proceeds through lines of constant neutron separation energies (or equivalently constant two-neutron separation energies with $S_{2n} = 2S_n$). Thus a sudden increase in the two-neutron separation energies implies the appearance of a gap in the r-process path that results in the absence of progenitor nuclei with $A \simeq 115$ (see figure 21). This behavior of the two-neutron separation energies is probably due to the sudden transition from deformed nuclei around $N = 75$ to spherical nuclei at the $N = 82$ shell closure. In mass models with a quenched (or even absent) shell gap like the ETFSI-Q mass model [79] the deformation is greatly reduced so that no transition occurs and consequently no increase in the two-neutron separation energies takes place. Nevertheless, it should be pointed out that the 'saddle point behavior' and the quenching of the shell gap are not necessarily related as the first could be also associated with the instabilities of the mean-field models in regions where several minima with different deformations are close in energy. In fact the experimentally known neutron separation energies never show this behavior when approaching neutron magic numbers (see figures 1–9 in [149]) and it is also absent in other mass models like the Duflo–Zuker model (see figure 5) and relativistic mean-field calculations [290] where the shell gap persists for nuclei below $Z = 40$.

Figure 21 shows the r-process paths obtained using equation (9) (i.e. $(n, \gamma) \rightleftarrows (\gamma, n)$ equilibrium) for a temperature of 1.35×10^9 K and a neutron density of 4.5×10^{21} cm^{-3} [289]. These values correspond to a two-neutron separation energy of 6.76 MeV according to equation (10). The mass models ETFSI-1 and FRDM show large gaps around $N = 75$, $Z = 40$ which correspond to the abundance trough seen in figure 20 around $A = 115$. As discussed above, this gap is not present in the ETFSI-Q mass models where a quenched $N = 82$ shell gap is assumed far from stability. However, it is also absent in the Duflo–Zuker mass model even if this model presents the largest neutron shell gap for $Z = 40$. Notice that the smaller gap, seen around $Z = 52$ $N = 88$ in the FRDM mass model and which is responsible for the appearance of an abundance trough around $A = 140$ in calculations that use this mass model (e.g. [289]), is not present in any of the ETFSI or in the Duflo–Zuker mass models. This gap is due to the strong variations of the two-neutron separation energies in the FRDM mass model above the neutron magic number $N = 82$ that is not present in any of the other mass models. This could indicate that some of the problems detected in r-process calculations [288] may be due to local deficiencies in global mass models.

In addition to its relevance in nucleosynthesis, the evolution of the $N = 82$ shell gap far from stability is interesting from the nuclear structure point of view and can have important consequences for the half lives of the $N = 82$ isotones. A reduced $N = 82$ shell gap causes increased excitation of neutrons into orbitals above the gap. As a consequence the β-decay half lives of $N = 82$ nuclei become shorter due to larger Q_β values while they are increased for smaller neutron numbers due to the delayed filling of the $\nu 0\mathrm{g}_{7/2}$ subshell which is the key orbital for the $\nu 0\mathrm{g}_{7/2} \rightarrow \pi 0\mathrm{g}_{9/2}$ allowed GT transition. The experimental nuclear structure indications for a reduced shell gap for $N = 82$, $Z \leqslant 50$ is based on the following arguments [16, 291].

- The large Q-value inferred for the ^{130}Cd β decay.
- The unsatisfactory shell model description of the ^{130}In spectrum [16], especially the 1^+ state fed in the β decay of ^{130}Cd which is shown in figure 22 left column.
- The systematics of the 2^+ states in the heavy Cd isotopes which decrease in approaching the $N = 82$ shell.

Recently large-scale shell model (LSSM) calculations have been performed in the proton $\pi(\mathrm{p}_{1/2}, \mathrm{g}, \mathrm{d}, \mathrm{s})$ and neutron $\nu(\mathrm{g}_{7/2}, \mathrm{d}, \mathrm{s}, \mathrm{h}_{11/2})$ model space allowing for up to 4p4h excitation across the $Z = 50$ shell. As excitations across the $N = 82$ shell are not considered a quenching of this shell is out of question for these studies. The results for ^{130}In are shown in the right column of figure 22. The agreement for the 1^+ state is greatly improved in comparison to [16], which is partly due to the new experimental proton $\pi \mathrm{p}_{1/2}$ and neutron $\nu \mathrm{g}_{7/2}$ SPE as discussed in section 2.1 and shown in figure 2(*b*). In a recent experiment of the GSI/RISING collaboration the 2^+ energy of ^{130}Cd was measured in the γ decay of an 8^+ μs isomer [292]. The level scheme and the $B(E2; 8^+ \rightarrow 6^+)$ show striking resemblance to the $N = 50$ isotope ^{98}Cd and can be well reproduced in the LSSM if interactions are properly monopole adjusted. A mean-field particle-number-projected HFB calculation [293] employing the Gogny force accounts for the 2^+ systematics of Cd and Te isotopes in approaching the $N = 82$ shell [292]. In the same stopped beam campaign at GSI/RISING a core excited isomer in ^{131}In was identified at an excitation energy that confirms an $N = 82$ shell gap unchanged relative to ^{131}Sn [294]. Therefore persistence of the $N = 82$ shell gap between $Z = 50$ and 48 is concluded.

In figure 23 theoretical half life predictions for $N = 82$ isotones obtained in macroscopic–microscopic (FRDM,ETFSI), mean-field (HFB) and shell model calculations as described here (LSSM) [198] are compared with the known experimental data. The half lives of ^{131}In, ^{130}Cd and ^{129}Ag [3, 295] serve as benchmarks to judge the predictive power of the various models. The shell model gives an excellent agreement with experiment proving adequate description of both GT strength and Q_β. Figure 24 compares the DF3 + CQRPA half lives for the chain of cadmium isotopes [164] to experimental data. The DF3 + CQRPA half lives agree with the

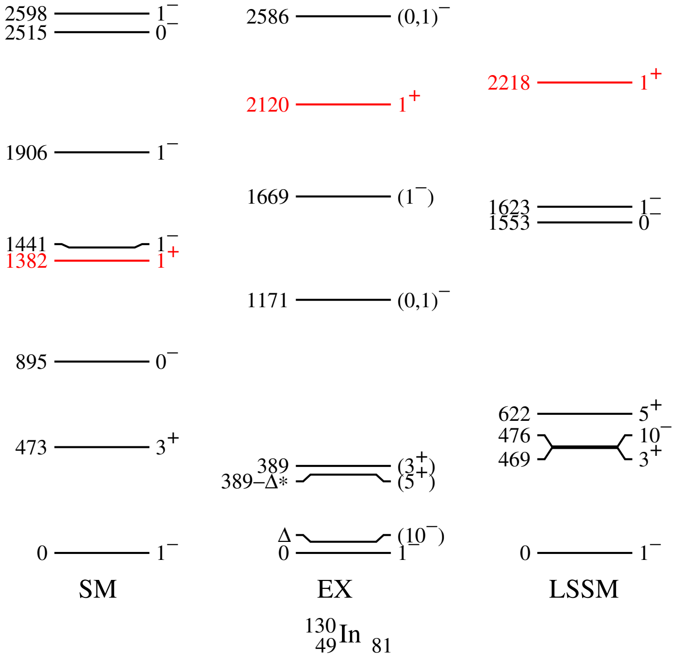

Figure 22. Experimental (EX) and shell model (SM) level scheme of ^{130}In in the proton (1p, $0g_{9/2}$) and neutron (2s, 1d, $0g_{7/2}$, $0h_{11/2}$) model space [16] in comparison to large-scale shell model (LSSM) results in the proton ($1p_{1/2}$, 2s, 1d, 0g) neutron (2s, 1d, $0g_{7/2}$, $0h_{11/2}$) model space [296]. The data are from [16] and for the β-decaying (10^-) and (5^+) isomers from [8].

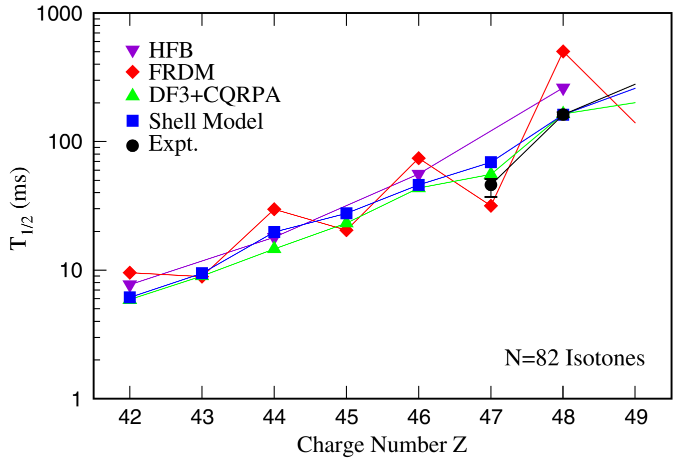

Figure 23. Half lives for $N = 82$ isotones in various approaches HFB [76], FRDM [57], DF3+CQRPA [77] and shell model [296] in comparison with experimental data for ^{129}Ag [3], ^{130}Cd [16] and ^{131}In [8].

data better than within a factor of two, including the r-process $N = 82$ waiting point ^{130}Cd. It is worth mentioning that the DF3 + CQRPA results for the r-process waiting point nuclei at $N = 50$, 82 and 126 agree quite well with the shell model results, where the latter regards GT transitions only [160, 164, 296]. Both model calculations also make predictions for β-delayed

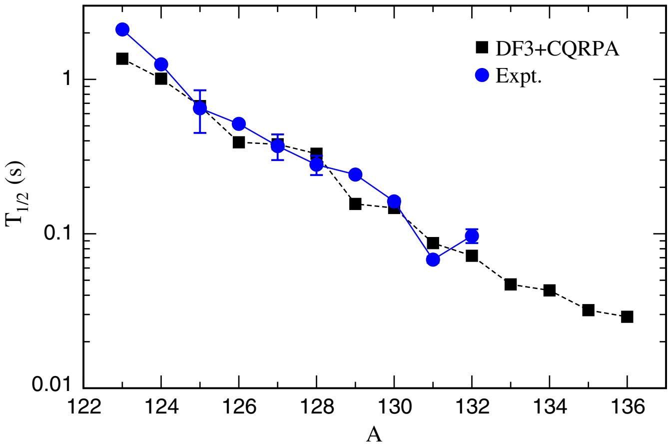

Figure 24. Theoretical DF3+CQRPA [164] results in comparison with experimental half lives for neutron-rich Cd isotopes.

neutron emission probabilities, which await experimental verification. Again the DF3+CQRPA calculations exhibit a completely different importance for GT and FF transitions for $Z < 50$ and $Z \geqslant 50$ $N \simeq 82$ nuclei. Below $Z = 50$ the allowed GT transition $\nu g_{7/2} \rightarrow \pi g_{9/2}$ dominates, which explains the good agreement with the shell model results regarding GT only. For $Z \geqslant 50$ $N \simeq 82$ nuclei the $\pi g_{9/2}$ is blocked and the $\nu f_{7/2} \rightarrow \pi g_{7/2}$ and $\nu g_{7/2} \rightarrow \pi d_{5/2}$ FF decays dominate. Similar to the ^{78}Ni region the role of FF contributions seems to be overestimated in [286].

The success of the concept of monopole-driven shell structure especially for the partially quenched $N = 50$ shell at ^{78}Ni, raises the question whether this could provide a possible scenario to understand the deficiency trough in r-process abundance distributions below the $A \simeq 130$ peak in astrophysical network calculations [3]. The $N = 82$ r-process nuclei which are needed to investigate shell quenching are ^{122}Zr to ^{130}Cd as shown in figure 21. Except for a renormalization due to the different shell model core, which in the simplest case is an $A^{-1/3}$ scaling, the evolution of the neutron hole states is governed by the same $\pi 0g_{9/2}\nu j$ interaction [29] as for the neutron particles states along $N = 50$ which is shown in figure 4 (MHJ) of [13]. In figure 25 the evolution of the $N = 81$ neutron hole states is shown as calculated from equation (6) employing an interaction as determined for a ^{132}Sn core [29, 90]. Starting points are the experimental values adopted in figure 2(*b*) for ^{132}Sn [6, 7]. The interaction $\pi(g_{9/2}, p_{1/2})$ with the $\nu f_{7/2}$ orbit above $N = 82$ is extrapolated from the ^{208}Pb region [90]. It is obvious that the $N = 82$ gap is preserved and the only dramatic change is the relative position of the $\nu g_{7/2}$ orbit which moves from lowest in the shell at $Z = 50$ to the Fermi surface at $Z = 40$. It should be noted that equation (6) holds only for closed j' shells as discussed in section 10.1, i.e. in the example of figure 25 for the points, provided the proton shell gap is preserved, too. In between due to configuration mixing the trend may deviate from the lines drawn, which only serve to guide the eye. The exact progression can be inferred from a full shell model calculation (see figure 4 in [13]). This does not exclude a shell gap reduction due to cross shell excitations when moving away from a doubly magic nucleus along a semi-magic chain of nuclei. Note that, e.g. from ^{100}Sn to ^{94}Ru this amounts to a ~2 MeV reduction (figure 19). To validate this extrapolation it has to be proven that the $Z = 38$ and 40 shell gaps are preserved on the way from ^{88}Sr and ^{90}Zr at $N = 50$ to the $N = 82$ isotopes ^{120}Sr and

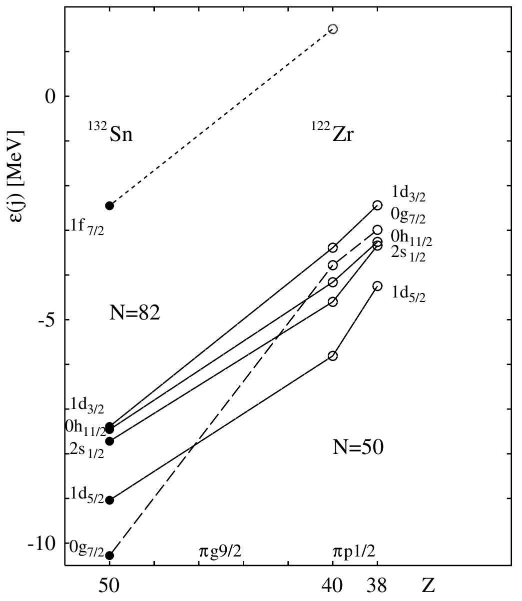

Figure 25. Evolution of the $N = 82$ shell gap below ^{132}Sn as function of Z from $Z = 50$ to the next proton subshell closures at $Z = 38$ and 40. Measured and extrapolated values are indicated by filled and open symbols [90]. The lines are drawn to guide the eye. In the open proton shell cross shell excitations may reduce the gap (see, e.g. figure 19 lower panel for $N = 50$ isotones).

^{122}Zr. In [13] it is shown that the positions of the $\pi\,g_{9/2}$ and $\pi\,p_{1/2}$ hole states in the In isotopes can be taken as a measure for the evolution of the $Z = 40$ shell gap. The $1/2^-$ excitation energies start from $\simeq$630 keV at $N = 50$ and drop between $N = 60$ and 66 to $\simeq$340 keV and stay there till $N = 82$ (302(32) keV [9], see ^{100}Sn and ^{132}Sn in figure 2). The reduction of the $Z = 40$ proton gap in ^{122}Zr by $\simeq$300 keV is in agreement with a shell model extrapolation of the ^{131}In $g_{9/2}$–$p_{1/2}$ energy difference using the $\pi\pi$ interaction that accounts excellently for the ^{130}Cd spectrum [292]. Experimentally nothing is known about the evolution of the $Z = 38$ gap, i.e. the 1p spin–orbit splitting. From the discussion of the π 1d SO splitting in section 2.4 (figure 8 and table 1) a similar apparent reduction can be expected for the π 1p orbitals. In essence a reduction of the $Z = 38$, 40 proton gaps at $N = 82$ to values below 3 MeV is expected which facilitates both proton and neutron ph excitations and therefore effectively shell erosion. It is also remarkable that both the reduction of the $\pi\,g_{9/2}$–$\pi\,p_{1/2}$ distance and the π 1p SO splitting should reach their minima at about $N = 70$ (see figure 8 for π 1d) which would not support the frequently discussed new double shell closure at the mid-r-process path nucleus $^{122}_{40}$Zr$_{70}$.

10.3. *The* $N = 126$ *shell and beyond*

The $N = 126$ shell gap is of similar importance for the r-process modeling calculations as the $N = 82$ gap. The experimental situation in the relevant region around $Z \leqslant 72$, however, is much worse. The most proton-deficient $N = 126$ nucleus, for which the half life is known, is $^{205}_{79}$Au$_{126}$ and it is only very recently that a detailed isomer spectroscopy of $^{204}_{78}$Pt$_{126}$ was performed by the GSI RISING collaboration [297, 298]. So new results from β decay studies in fragmentation of ^{208}Pb or ^{238}U may be close ahead.

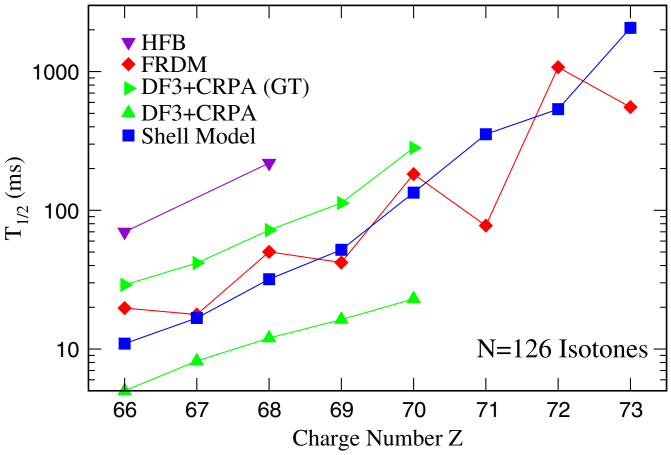

Figure 26. Theoretical half life predictions for $N = 126$ isotones in the shell model [299], the HFB [76], FRDM [57] and the DF3+CQRPA [77] approaches.

Closer inspection of the shell model orbits involved and their counterparts in the $N \simeq 82$ region (see figure 2) reveal differences which affect the relative role of allowed GT and FF transitions. The allowed GT transition $\nu h_{9/2} \rightarrow \pi h_{11/2}$ besides being blocked early due to filling of the $\pi h_{11/2}$ orbit has a much smaller decay energy than the corresponding $N = 82$ configuration $\nu g_{7/2} \rightarrow \pi g_{9/2}$ (see figure 2(*b*)) and the $\nu i_{13/2} \rightarrow \pi i_{11/2}$ effective Q_β is even smaller. Therefore the high-energy FF $\nu i_{13/2} \rightarrow \pi h_{11/2}$ Q_β-value, which is associated with this transition, is even smaller implying that the high-energy FF $\nu i_{13/2} \rightarrow \pi h_{11/2}$ dominates [164]. In figure 26 half life predictions for $N = 126$ isotones using the same approaches as for the $N = 82$ isotones shown in figure 23 are shown; these results exhibit similar characteristics and expect experimental verification. A very satisfying reproduction of the half lives of proton-deficient nuclei around the $N = 126$ shell closure is obtained within the DF3 + CQRPA approach [77]. Regarding GT transitions, the shell model [160] yields half lives which are faster by a factor of 2–3 than the DF3 + CQRPA GT results, but they exceed the GT + FF half lives by about a factor of five [164]. Once FF transitions are included in the shell model calculations one can have confidence in the extension of both approaches to the $N = 126$ waiting point nuclei ($Z \approx 68$–76) for half lives and delayed neutron emission probabilities, for which no experimental data exist yet.

10.4. Shell structure and the role of fission

Recent observations in metal-poor old stars show always the same relative abundance distributions for r-process elements with $Z > 56$, implying that the r-process responsible for the production of these elements is quite robust [251]. Here robust means that the production occurs always under similar astrophysical conditions resulting in similar abundance patterns or that the final abundance pattern becomes independent of the astrophysical conditions probably because very extreme conditions are achieved. From the astrophysical side the present situation is unfortunate as none of the current supernovae models can achieve the large neutron-to-seed ratios necessary for the production of r-process nuclei around the third peak ($A \sim 195$) [268]. Several studies have shown that the neutrino-driven wind can in fact reproduce the r-process abundance provided large enough neutron-to-seed ratios are assumed [86]. Nevertheless, one will still need that the astrophysical models converge to a single set of conditions that produce a

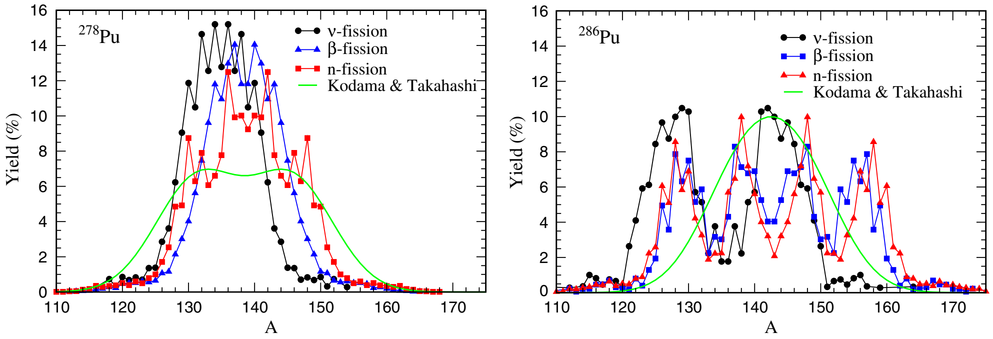

Figure 27. Yields for the fission of ^{278}Pu and ^{286}Pu induced either by neutron capture, beta-decay or neutrino capture. The line shows the parametrization of Kodama and Takahashi [300] that has been extensively used in r-process calculations. The yields have been computed using the ABLA code [301, 302] and the fission barriers of [303].

robust r-process pattern. An alternative is to consider an astrophysical scenario in which large enough neutron-to-seed ratios are achieved to induce fission cycling during the r-process. In this case fission could represent a way of producing a robust nucleosynthesis pattern [271] that is independent of the astrophysical conditions provided these permit the onset of fission. The currently available global parametrizations of fission barriers [167, 303] predict an increase in fission barriers for neutron-rich nuclei. This implies that fission during the r-process only becomes important once the theoretically postulated $N = 184$ magic number is overcome. At this time fission can occur in several ways: spontaneous, neutron-induced, beta-delayed, and if the r-process occurs under strong neutrino fluxes, neutrino-induced fission. The role of fission in the r-process has been the subject of many studies in the past (see [304] and references therein), however, often only a subset of fission-inducing reactions was considered and a rather simplistic description of fission yields was used. It should be emphasized that, if fission really plays a role in determining the final abundances of the r-process, one needs not only fission rates but—equally important—realistic fission yields as they determine the final abundances. Recently this situation has been improved by putting together a full set of fission rates including all possible fission reactions listed above [305–307]. For each fissioning nucleus the fission yields are determined using the statistical code ABLA [301, 302] which reproduces the existing data for fission yields very well. The fission yields change from nucleus to nucleus and in a given nucleus depend on the excitation energy at which fission is induced. Figure 27 shows the fission yields for the two nuclei ^{278}Pu and ^{286}Pu that are abundant during the r-process before neutrons are exhausted and matter decays to stability.

Figure 28 shows the results of r-process calculations for two different mass models. The calculations assume an adiabatic expansion of the ejected matter with a constant velocity of 4500 km s^{-1} (corresponding to a dynamical time scale of 50 ms) [86]. The density is evolved assuming that the mass in a given mass shell is constant and the temperature is determined from the equation of state under the condition of constant entropy. The curves are labeled according to the entropy s and neutron-to-seed ratio (n/seed) resulting after the alpha-rich freeze-out. In all calculations the r-process starts with an initial seed distribution around $A \sim 90$ and, by neutron captures, the matter flows to heavier nuclei reaching the $N = 184$ shell gap. Once this gap is bridged, fission is induced via neutron capture till the neutrons are exhausted. Then briefly beta-delayed fission becomes the dominating fission channel, until the neutrons, liberated by the fission processes, can induce new fission events. This makes neutron-induced fission the dominating fission channel.

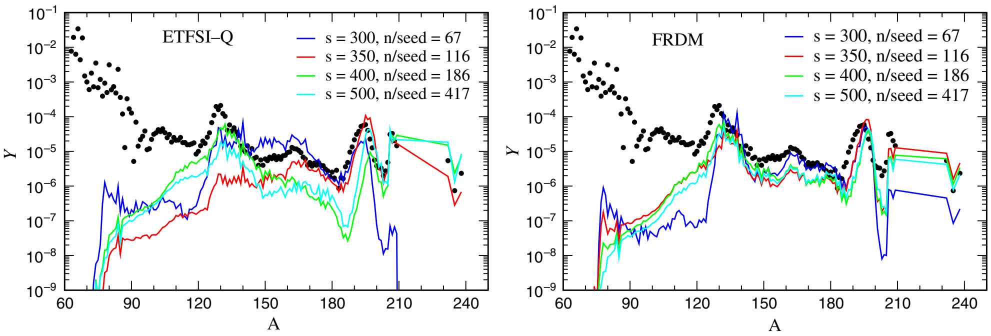

Figure 28. Final r-process abundances (at 1.6 Gy after the r-process event) obtained in several adiabatic expansions using two different mass models (FRDM [57] and ETFSI-Q [79]). The solid circles correspond to a scaled solar r-process abundance distribution [308].

While the FRDM mass model yields similar abundance distributions with increasing neutron-to-seed ratio, the ETFSI-Q mass model does not. This is due to the different behavior of the FRDM and ETFSI-Q models after the $N = 82$ and $N = 126$ shell closures. In particular the FRDM predicts a fast drop in the neutron separation energy when the r-process breaks out of the $N = 82$ and $N = 126$ waiting point nuclei (see the saddle point behavior in figure 5 after $N = 82$ and $N = 126$ for the FRDM mass model). This holds matter in nuclei with relatively long beta-decay half lives and reduces the mass flow to heavier fissioning nuclei. In the ETFSI-Q the r-process can reach heavier nuclei with shorter half lives after breaking out of $N = 82$ and $N = 126$ so that the mass flow to heavy nuclei is faster. In this way most of the neutrons are used for the build up of heavy nuclei and very few are left to induce fission events. In calculations that use the FRDM mass model, a smaller amount of matter passes the $N = 82$ and $N = 126$ waiting points. Once this matter reaches the region of fissioning nuclei, a large abundance of neutrons is still present which, as explained above, induces further fission events liberating more neutrons and allowing the r-process to last for a longer time and produce a larger fraction of fission fragments. This explains why the FRDM mass model produces larger amounts of matter in the range $A = 130$–190. It should be also noted that the shell structure around $N = 184$ is also important for determining the role of fission. In this sense the ETFSI-Q model predicts a larger shell gap than the FRDM model that additionally contributes to reducing the amount of fission present in these models. The above discussion clearly shows that it is important to know the shell structure around neutron magic numbers in order to determine the role of fission in r-process nucleosynthesis.

11. The rp-process

In recent reviews the astrophysical conditions and nuclear structure impact on explosive hydrogen burning have been discussed in great detail [4, 224]. The most likely astrophysical sites for explosive hydrogen burning are novae and x-ray bursts. The process is triggered by the break-out reactions from the hot CNO cycle and the ignition of the triple α reaction that produces fresh material for the CNO cycle and the feeding of the rp-process [4, 222]. The mechanism depends critically on the rates of the alpha capture reactions on ^{15}O and ^{18}Ne. The thermonuclear runaway of an x-ray burst is driven by the αp-process and by rapid proton captures (rp-process) which convert the initial material rapidly to ^{56}Ni causing the formation of Ni oceans at the neutron star surface. The αp-process is characterized by a sequence of

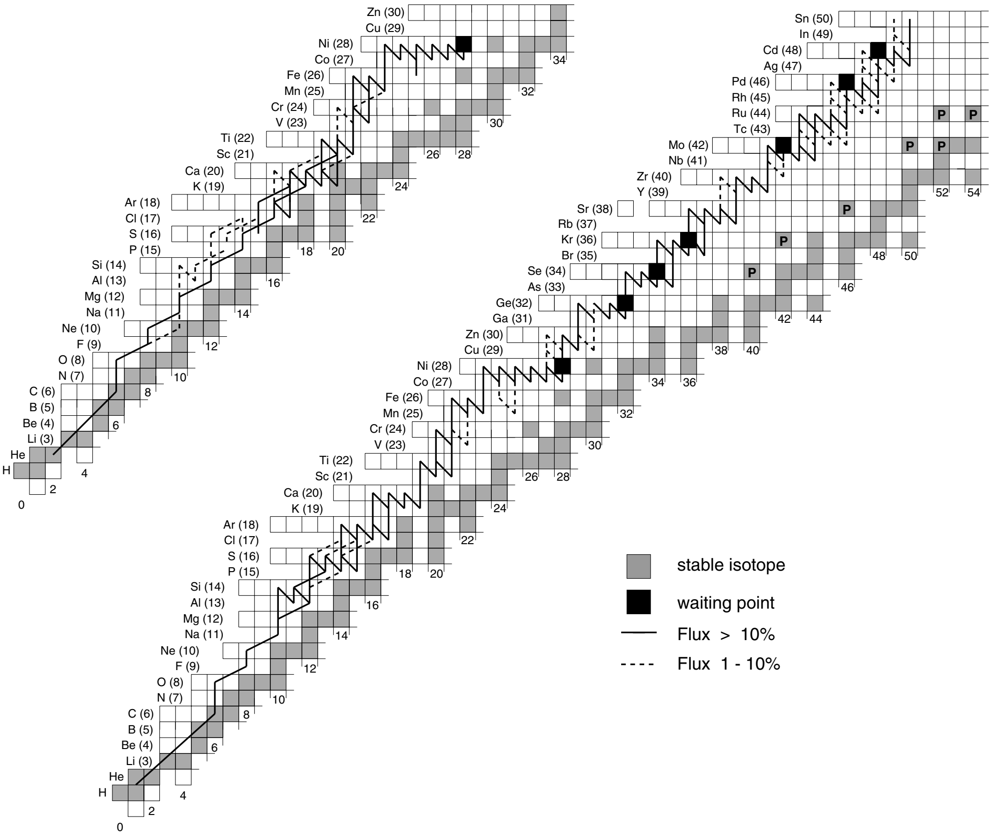

Figure 29. The paths of the rp- and αp-processes up to and beyond ^{56}Ni under different astrophysical conditions [1]. The process is stopped at ^{56}Ni at temperatures of (2–3) × 10^9 K due to a (p, γ)–(γ, p) equilibrium and a low Q-value (upper panel). If at lower temperatures photodisintegration is suppressed the process continues up to ^{100}Sn (lower panel).

(α, p) and (p, γ) reactions processing the ash of the hot CNO cycles, ^{14}O and ^{18}Ne, up to the ^{34}Ar and ^{38}Ca range. The rp-process represents a sequence of rapid proton captures up to the proton dripline and subsequent β-decays of dripline nuclei processing the material from the argon, calcium range up to ^{56}Ni and beyond. The rp-process path is shown in figure 29. The runaway freezes out in thermal equilibrium at peak temperatures of around (2.0–3.0) × 10^9 K due to a (p, γ)–(γ, p) equilibrium and low Q-values (upper panel of figure 29). Re-ignition of the rp-process takes place during the subsequent cooling phase of the explosion by suppression of photodisintegration, mainly enabling the (p, γ) reaction on ^{56}Ni to compete with its inverse, thus allowing matter flow beyond ^{56}Ni up to ^{100}Sn (lower panel of figure 29).

11.1. The rp- and αp-process paths below ^{56}Ni

To verify the present models nuclear reaction and structure studies on the neutron deficient side of the line of stability are essential. Measurements of the break-out reactions will set stringent constraints on the ignition conditions for the thermonuclear runaway, measurements of alpha and proton capture on neutron deficient radioactive nuclei below ^{56}Ni will set limits on the time scale for the actual runaway, but will also affect other macroscopic observables.

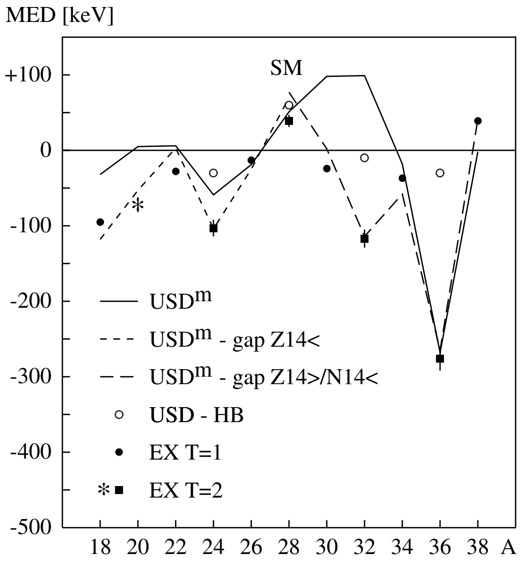

Figure 30. Experimental mirror energy differences for $T = 1$ and $T = 2$ 1s0d shell nuclei and shell model results [102, 314]. The recently measured $A = 20$ value ($\star$) [311] completes the $T = 2$ chain and confirms the shell model prediction [102].

Recent simulations of the x-ray burst characteristics with self-consistent multi-zone models suggested a significant impact of proton capture reaction rates between $A = 20$ and $A = 64$ on expansion velocity, temperature and luminosity of the burst [309, 310].

The nuclear structure input needed for the description of bound states in the rp-process below ^{56}Ni is inferred from experimental data by means of model descriptions. Besides the cluster model which has been discussed in sections 4 and 7, reliable shell model calculations with predictive power are at hand in the 1s0d [39] and 1p0f [36, 37, 42] shells. As nuclei with $T_z \geqslant 0$ are more reliably known isospin symmetry can be used to describe the $T_z < 0$ mirror nuclei in the rp-process path (see figure 29). However, neither the shell model nor other theoretical approaches are able to predict the energies of states sufficiently accurately to allow for reliable estimates of capture rates if resonances happen to be located in the Gamow energy window and hence dominate the capture rate. An essential prereqisite for a correct extrapolation is a satisfactory calculation of Coulomb energies and Thomas–Ehrmann shifts. While this seems well under control in the $f_{7/2}$ part of the 1p0f shell for $T \leqslant 1$ states [312, 313] a recent study of mirror energy differences (MED) in the 1s0d shell [102] has shown that the extremely large MED cannot be described properly in terms of Coulomb energies only [314]. In figure 30 experimental MED for $T = 1,2$ states in the sd shell are shown and compared with shell model results using isospin asymmetric single-particle energies from the $A = 17$ isobars and an isospin-symmetric two-body interaction obtained from a modified USD interaction [34, 39, 102] (solid line). The observed discrepancy in midshell can only be cured if additionally a substantial reduction of the proton and neutron subshell gaps at $Z = 14$ respective $N = 14$ for the proton-rich $N = 8$ isotones and $Z = 20$ (Ca) isotopes is introduced (dashed lines) [102]. This is clear though model dependent evidence that at the proton dripline both proton and neutron gaps are reduced relative to their mirror partners. A consistent description of the dripline region requires a treatment by models which account for the continuum, e.g. by the Gamow shell model (see section 3). It should be noted that the MED shown in figure 30 are large enough to influence barrier penetration for proton capture seriously. The accuracy needed for (p, γ) Q-values due to the exponential dependence of penetration on the decay energy is $\simeq$100 keV, while it is $\simeq$10 keV for resonance captures [224]. It is obvious from figure 29 (lower panel) that at temperatures below 2×10^9 K, when the rp-process is driven towards the proton dripline, this becomes important. The cluster aspect of rp-process relevant nuclear structure is discussed in section 7.

11.2. The rp-process path above ^{56}Ni

Nuclear structure and nuclear reaction measurements near the doubly closed shell nucleus ^{56}Ni determine the conditions for the re-ignition of the burst in its cooling phase. A crucial role is played here by the (p, γ) reaction on ^{56}Ni as due to the very low proton separation energy in ^{57}Cu proton capture can only overcome photodisintegration if the temperature has dropped to $T \approx 9 \times 10^8$ K which is achieved by matter expansion. With present-day techniques a direct measurement of the ^{56}Ni(p,γ) cross section is not feasible [224]. However, an estimate of this important cross section could be derived indirectly using spectroscopic informations obtained from (d, p) and (^{3}He, d) reactions on ^{56}Ni [10, 315]. Structure and reaction measurements beyond ^{56}Ni, in particular the experimental study of two-proton capture reactions bridging the dripline for even–even $N = Z$ nuclei like ^{68}Se, ^{72}Kr and possibly ^{76}Sr, are necessary to determine the final fate of the neutron star crust. These reaction measurements have to be complemented with decay studies. Of particular importance are beta-decay studies of isomeric and/or thermally populated excited states, which are not accessible by experiment with present equipment. In general there is a substantial need for nuclear structure information at the proton drip line, especially in the Ge–Kr mass region and most likely up to the Sn–Te–I mass range where the endpoint of the rp-process is expected. The information needed to calculate the flow of nuclear reactions in x-ray bursts includes masses, lifetimes, level structures and proton separation energies. An important structure ingredient governing the rp-process is the position of the proton dripline as seen in figures 29 and 31. The odd–even Z staggering of the last particle bound isotope, which is due to the pairing force, creates waiting points that can only be passed after delay via β-decay and subsequent proton capture or as in the cases of ^{68}Se, ^{72}Kr and possibly ^{76}Sr by two-proton captures.

The latter process has been considered only recently and, based on statistical Hauser–Feshbach calculations, was found to compete with the β-decay detour due to the finite lifetime of the intermediate proton-unbound odd-Z nucleus [4]. The rate estimates, however, are often hampered by the unsufficient knowledge of the resonance energy (mass). The accuracy of mass extrapolations for trans-dripline nuclei from their mirrors by accounting for the Coulomb energy is again in the 100 keV range and exceeds that of global mass models by far. A general unknown systematic uncertainty is introduced by (i) mirror energy differences (MED) due to quenching of the two-body interaction by reduced overlap at the dripline [103] and (ii) shape differences in the initial, resonance and final states [68]. The former will affect penetration factors while the latter determines spectroscopic factors. Experimentally little is known about the inverse process of proton decay and spectroscopic factors. Recently proton decay of high-spin states have been reported in ^{58}Cu [316, 317] and ^{94}Ag [67] and interpreted [68, 318]. In both cases large suppression of the partial widths due to different shapes of parent and daughter states was inferred.

Recently Grigorenko has shown within a three-body approach for the ^{15}O + 2p reaction that two-proton capture through non-resonant states can significantly enhance the capture rate [319]. It is important to find out whether this is also the case for the 2p-captures on the rp-process waiting point nuclei.

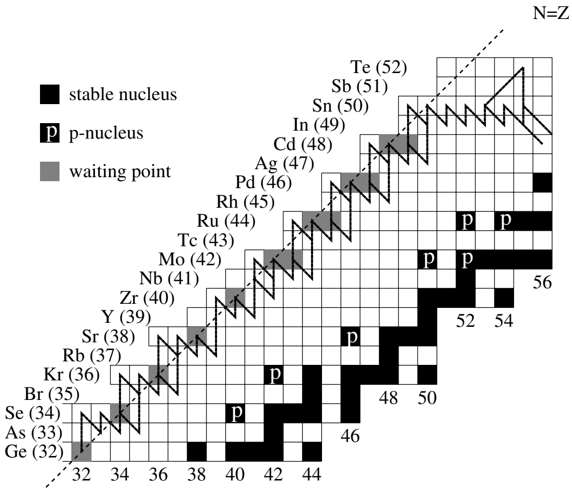

Figure 31. The rp-process path beyond $Z = 32$ [4]. The termination due to fast α decay beyond ^{100}Sn was taken from [223, 224].

Shape coexistence in the $A \approx 80$ region which is due to the shape driving effect of the $g_{9/2}$ orbital may change drastically the GT distribution for β decay and its location inside the $Q_{\mathrm{EC}} - S_{\mathrm{p}}$ window and therefore both half lives and β-delayed proton emission. For illustration in figure 32 the GT distributions for the $^{80}\mathrm{Zr} \rightarrow {}^{80}\mathrm{Y}$ as calculated in the FRDM/QRPA [57,320] is shown for the three competing shapes at $N = Z = 40$ in figure 4. The large uncertainties are best characterized by the experimental values and errors for $S_{\mathrm{p}} = 3.03(18)$ MeV and $Q_{\mathrm{EC}} = 5.7(1.5)$ MeV [149]. Shape coexistence gives rise to $I^{\pi} = 0^{+}$ shape isomers as recently observed in ^{72}Kr, that will be populated in β decay. For low excitation energy and/or in the absence of atomic electrons in a hot environment the E0 ground state transitions will be hindered giving rise to substantial half lives. If such shape isomers exist in nuclei along the rp-process path, the astrophysical significance is that the proton capture on long-lived isomers may speed up the reaction flow, thus reducing the time scale for the rp-process nucleosynthesis during the cooling phase [2, 321].

One zone parametrized x-ray burst calculations have shown that the rp-process terminates in a SnSbTe cycle [223] (see figure 31). The reason is that the light tellurium isotopes $^{105-108}$Te are unbound against α emission by 3.4–4.9 MeV. Recently the α decay of the ^{105}Te ground state was observed [322, 323] with a half life of 0.6 μs and a decay energy of 4.889(6) MeV. The presence of fast α decays is a clear signature for a pronounced shell closure at $Z, N = 50$ as known from the ^{208}Pb region [324] and is expected to be even enhanced at $N \simeq Z$ as *superallowed* α decay is predicted. The cyclic flow pattern stops continuation of the rp-process to higher Z and at the same time is a source of increased ^{4}He production. More realistic multi-zone calculations [325, 326] have shown that only the first burst can reach the SnSbTe cycle, for successive bursts a combination of ash from the previous burst and more realistic modeling of burning in a range of mass zones gives conditions which realistically do not produce nuclei heavier than $A \sim 60$.

12. Summary and outlook

The description of a large variety of astrophysical events requires knowledge of the relevant nuclear physics input combined with state-of-the-art hydrodynamic modeling, which then

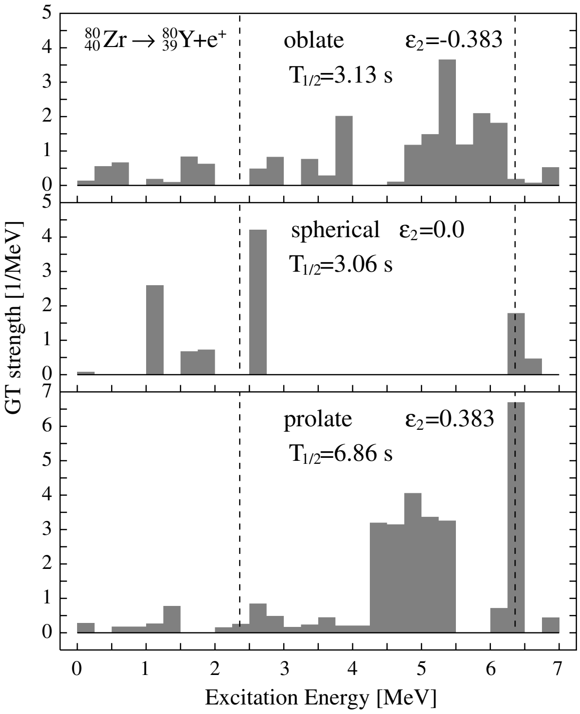

Figure 32. Gamow–Teller distribution and half life for the β decay of ^{80}Zr calculated for three different shapes as indicated in figure 4 [4]. The dashed lines mark the theoretical proton separation energy S_p in the daughter ^{80}Y and the Q_{EC} value. Best experimental estimates for these quantities are 3.03(18) Mev and 5.7(1.5) MeV, respectively.

leads to testable predictions with actual observations. The field of nuclear astrophysics has benefitted recently from a wealth of data of unprecedented quality provided by both satellite and earthbound observations as well as by neutrino detectors. Many of these new insights relate to explosive astrophysical events like supernovae, novae or x-ray bursters, which occur at rather extreme temperatures and densities. Under these conditions unstable nuclei with very exotic proton-to-neutron ratios come into existence and determine the dynamics of the astrophysical events. In the future, experiments with radioactive ion beams will allow one to determine some of the crucial nuclear input data directly making it unnecessary to rely on empirical global models. Equally important, these investigations are essential for the understanding of the isospin and density-dependence of the effective nucleon–nucleon interaction thus constraining and improving nuclear models and giving more confidence in the application of such models to nuclei very far-off stability where data are not yet available, but which are required to simulate, for example, supernovae explosions or r-process nucleosynthesis.

In this paper we have summarized some of the recent experimental and theoretical progress related to several astrophysical events. Our review includes

- the evolution of nuclear structure towards the driplines and the ‘sites’ of astrophysical processes in the Segré chart;
- the current status, its potential and the predictability of nuclear structure models such as the spherical shell model, the continuum shell model, the cluster model and the globally

applicable models based on the deformed shell structure in the macroscopic–microscopic approach and on density functionals;

- global properties of nuclei like masses, half lives and level densities, which are indispensable input data for astrophysical nucleosynthesis calculations;
- the role of weak interaction processes in the evolution and nucleosynthesis of several astrophysical events;
- key examples of nuclear structure impact on different nucleosynthesis scenarios including Big Bang nucleosynthesis, s- and r-processes;
- the current experimental evidences for the quenching of neutron shell gaps far-off stability and its relevance for the abundance predictions of r-process models;
- the role of fission in r-process calculations and its dependence on the shell structure far-off stability and
- nuclear properties and reactions relevant for the rp-process that occurs in x-ray bursts.

Future challenges for nuclear structure theory are the extension of *ab initio* calculations based on realistic nucleon–nucleon interactions to nuclei beyond $A = 12$. This can be achieved by the Green's function Monte Carlo and the no-core shell model, which have been successfully applied to a detailed description of light nuclei in recent years, or by alternative approaches like the coupled-cluster model and the fermionic molecular dynamics or antisymmetric molecular dynamic models. The latter offer the appealing feature to describe also cluster degrees of freedom, which often occur in light nuclei, and to allow a consistent description of bound, resonant and scattering states which makes them the method of choice for studies of low-energy reactions among light nuclei as they are important in hydrostatic stellar burning and offers the possibility of extending *ab initio* models from the description of nuclear structure to nuclear reactions. Intermediate mass and heavy nuclei are traditionally described by the nuclear shell model and by mean-field approaches. Here the challenge is to further improve the effective interactions in such studies by, for example, better incorporation of long- and short-range correlations and, for the shell model, to derive improved treatments for the evolution of the monopole shift with mass number.

Experimental nuclear spectroscopy of exotic nuclei far off the stability line provides stringent constraints for theoretical models. Experimental radioactive beam (RIB) programs are presently being pursued world-wide by major research laboratories. Upgrades to improve RIB intensities and R&D programs for the development of new facilities have started, providing research opportunities with nuclei closer to the driplines. ISAC at TRIUMF, REX-ISOLDE at CERN, SPIRAL at GANIL, the A1900 fragment separator (FRS) at NSCL/MSU and FRS/RISING at GSI are operating. The upgraded radioactive beam factory (RIBF) at RIKEN will start in 2007. The project features a superconducting cyclotron and a projectile-like fragment separator system to provide intensive high-energy RIB. SPIRAL 2 at GANIL is planned to start operation in 2010. In the US a radioactive ion-beam facility of the next generation is also projected. At GSI the future Facility for Antiproton and Ion Research (FAIR) is planned to deliver beams in 2012 opening an unprecedented range of experimental opportunities around a superconducting double-ring synchrotron, a system of storage rings for beam collection and cooling and a new superconducting fragment separator Super-FRS. RIB energies range from 10–100 MeV/nucleon to stopped ions that may be extracted and reaccelerated to tens of keV/nucleon. Once these facilities are operational a new era of nuclear astrophysics will begin.

Acknowledgments

The authors gratefully acknowledge support and assistance by their collegues I Borzov, H Feldmeier, M Górska, A Jungclaus, T Neff, H Schatz, F-K Thielemann and M Wiescher for discussion, provision of figures and communication of results prior to publication.

References

[1] Langanke K, Thielemann F-K and Wiescher M 2004 *The Euroschool Lectures on Physics with Exotic Beams vol 1* (*Lecture Notes in Physics* vol 651) pp 383–467
[2] Aprahamian A, Langanke K and Wiescher M 2005 *Prog. Part. Nucl. Phys.* **54** 535–613
[3] Pfeiffer B, Kratz K L, Thielemann F-K and Walters W B 2001 *Nucl. Phys.* A **693** 282–324
[4] Schatz H *et al* 1998 *Phys. Rep.* **294** 167–263
[5] Käppeler F and Mengoni A 2006 *Nucl. Phys.* A **777** 291–310
[6] Grawe H and Lewitowicz M 2001 *Nucl Phys.* A **693** 116–32
[7] Grawe H 2004 *The Euroschool Lectures on Physicswith Exotic Beams vol 1* (*Lecture Notes in Physics* vol 651) pp 33–75
[8] ENSDF database, http://www.nndc.bnl.gov/ensdf/
[9] Fogelberg B *et al* 2004 *Phys. Rev.* C **70** 034312
[10] Rehm K E *et al* 1998 *Phys. Rev. Lett.* **80** 676–79
[11] Grawe H, Schubart R, Maier K H and Seweryniak D 1995 *Phys. Scr.* T **56** 71–8
[12] Lisetskiy A, Brown B A, Horoi M and Grawe H 2004 *Phys. Rev.* C **70** 044314
[13] Grawe H, Blazhev A, Górska, Grzywacz R and Mukha I 2006 *Eur. Phys. J.* A **27** (s01) 257–67
[14] Caurier E, Martínez-Pinedo G, Nowacki F, Poves A and Zuker A P 2005 *Rev. Mod. Phys.* **75** 427–88
[15] Martínez-Pinedo G, Zuker A P, Poves A and Caurier E 1997 *Phys. Rev.* C **55** 187–205
[16] Dillmann I *et al* 2003 *Phys. Rev. Lett.* **91** 162503
[17] Duflo J and Zuker A P 1999 *Phys. Rev.* C **59** 2347–50
[18] Brown B A 1998 *Phys. Rev.* C **58** 220–31
[19] Ring P 1996 *Prog. Part. Nucl. Phys.* **37** 193–263
[20] Brown B A 2001 *Prog. Part. Nucl. Phys.* **47** 517–603
[21] Otsuka T and Fukunishi N 1996 *Phys. Rep.* **264** 297–310
[22] Navratil P and Barrett B R 1998 *Phys. Rev.* C **57** 3119–28
[23] Barrett B R, Navratil P and Vary J P 2002 *Nucl. Phys.* A **704** 254c–63c
[24] Caurier E, Rejmund M and Grawe H 2003 *Phys. Rev.* C **67** 054310
[25] Sinatkas J *et al* 1992 *J. Phys. G: Nucl. Part. Phys.* **18** 1377–400
Sinatkas J *et al* 1992 *J. Phys. G: Nucl. Part. Phys.* **18** 1401–18
[26] Otsuka T *et al* 2002 *Nucl. Phys.* A **704** 21c–26c
[27] Nogga A, Navratil P, Barrett B R and Vary J P 2006 *Phys. Rev.* C **73** 064002
[28] Epelbaum E 2006 *Prog. Part. Nucl. Phys.* **57** 654–741
[29] Hjorth-Jensen M, Kuo T T S and Osnes E 1995 *Phys. Rep.* **261** 125–270
[30] Bogner S, Kuo T T S and Coraggio L 2001 *Nucl. Phys.* A **684** 432c–6c
[31] Suzuki K and Lee S Y 1980 *Prog. Theor. Phys.* **64** 2091–106
[32] Roth R, Hergert H, Papakonstantinou P, Neff T and Feldmeier H 2005 *Phys. Rev.* C **72** 034002
[33] Neff T and Feldmeier H 2003 *Nucl. Phys.* A **713** 311–71
[34] Utsono Y, Otsuka T, Mizusaki T and Honma M 1999 *Phys. Rev.* C **60** 054315
[35] Poves A and Zuker A P 1981 *Phys. Rep.* **70** 235–314
[36] Caurier E, Zuker A P, Poves A and Martínez-Pinedo G 1994 *Phys. Rev.* C **50** 225–36
[37] Poves A, Sanchez-Solano J, Caurier E and Nowacki F 2001 *Nucl. Phys.* A **694** 157–98
[38] Cohen D and Kurath D 1965 *Nucl. Phys.* A **73** 1–24
[39] Brown B A and Wildenthal B H 1988 *Annu. Rev. Nucl. Sci.* **38** 29–66
[40] Brown B A and Richter W A 2006 *Phys. Rev.* C **74** 034315
[41] Richter W A, Van der Merve M J, Julies R E and Brown B A 1991 *Nucl. Phys.* A **523** 325–353
[42] Honma M, Otsuka T, Brown B A and Mizusaki T 2002 *Phys. Rev.* C **65** 061301
[43] Brown B A, Etchegoyen A, Godwin N, Rae W, Richter W, Ormand W E, Warburton E, Winfield J, Zhao L and Zimmerman C 1985 *MSU-NSCL Report* No 524
Brown B A, Etchegoyen A, Godwin N, Rae W, Richter W, Ormand W E, Warburton E, Winfield J, Zhao L and Zimmerman C 2004 *MSU-NSCL Report* No 1289

[44] Caurier E and Nowacki F 1999 *Acta Phys. Pol.* B **30** 705–14

[45] Ormand W E and Johnson C 2002 *Shell model code REDSTICK* http://phys.lsu.edu/graceland/faculty/cjohnson/redstick

[46] Mizusaki T 2000 *RIKEN Acc. Prog. Rep.* **33** 14

[47] Johnson C W, Koonin S E, Lang G H and Ormand W E 1992 *Phys. Rev. Lett.* **69** 3157–60

[48] Koonin S E, Dean D J and Langanke K 1997 *Phys. Rep.* **278** 1–77

[49] Lang G H, Johnson C W, Koonin S E and Ormand W E 1993 *Phys. Rev.* C **48** 1518–45

[50] Alhassid Y, Dean D J, Koonin S E, Lang G and Ormand W E 1994 *Phys. Rev. Lett.* **72** 613–6

[51] Otsuka T, Honma M and Mizusaki T 1998 *Phys. Rev. Lett.* **81** 1588–91

[52] Otsuka T, Honma M, Mizusaki T, Shimizu N and Utsuno Y 2001 *Prog. Part. Nucl. Phys.* **47** 319–400

[53] Petrovici A, Schmid K W, Faessler A, Hamilton J H and Ramayya A V 1999 *Prog. Part. Nucl. Phys.* **43** 485–535

[54] Schmid K W 2001 *Prog. Part. Nucl. Phys.* **46** 145–54

[55] Elliott J P 1958 *Proc. R. Soc. Lond.* Ser. A **245** 128
Elliott J P 1958 *Proc. R. Soc. Lond.* Ser. A **245** 562

[56] Rauscher T and Thielemann F-K 2000 *At. Data Nucl. Data Tables* **75** 1–351

[57] Möller P, Nix J R and Kratz K-L 1997 *At. Data Nucl. Data Tables* **66** 131–343

[58] Raman S, Nestor C W and Tikkanen P 2001 *At. Data Nucl. Data Tables* **78** 1–128

[59] Glasmacher T 2001 *Nucl. Phys.* A **693** 90–104

[60] Radford D C *et al* 2002 *Phys. Rev. Lett.* **88** 222501

[61] Scheit H *et al* 2005 *Eur. Phys. J.* A **25** (s01) 397–402

[62] Grodzins L 1962 *Phys. Lett.* **2** 88–91

[63] Stephens F S, Diamond R M, Leigh J R, Kammuri T and Nakai K 1972 *Phys. Rev. Lett.* **29** 438–441

[64] Möller P and Nix J 1992 *Nucl. Phys.* A **536** 20–60

[65] Möller P, Nix J, Myers W and Swiatecki W 1995 *At. Data Nucl. Data Tables* **59** 185–381

[66] Pearson J M and Goriely S 2006 *Nucl. Phys.* A **777** 623–644

[67] Mukha I *et al* 2005 *Phys. Rev. Lett.* **95** 022501

[68] Delion D S, Liotta R J and Wyss R 2003 *Phys. Rev.* C **68** 054603

[69] Aboussir Y, Pearson J M, Dutta A K and Tondeur F 1995 *At. Data Nucl. Data Tables* **61** 1–30

[70] Lalazissis G A, Raman S and Ring P 1999 *At. Data Nucl. Data Tables* **71** 1–40

[71] Goriely S, Tondeur F and Pearson J M 2001 *At. Data Nucl. Data Tables* **77** 311–81

[72] Goriely S, Samyn M, Heenen P-H, Pearson J M and Tondeur F 2002 *Phys. Rev.* C **66** 024326

[73] Samyn M, Goriely S, Heenen P-H, Pearson J M and Tondeur F 2002 *Nucl. Phys.* A **700** 142–56

[74] Duflo J and Zuker A P 1995 *Phys. Rev.* C **52** R23–27

[75] Borzov I N and Goriely S 2000 *Phys. Rev.* C **62** 035501

[76] Engel J, Bender M, Dobaczewski J, Nazarewicz W and Surman R 1999 *Phys. Rev.* C **60** 014302

[77] Borzov I N 2003 *Phys. Rev.* C **67** 025802

[78] Aboussir Y, Pearson J M, Dutta A K and Tondeur F 1992 *Nucl. Phys.* A **549** 155–79

[79] Pearson J M, Nayak R C and Goriely S 1996 *Phys. Lett.* B **387** 455–59

[80] Werner T R, Dobaczewski J and Nazarewicz W 1997 *Z. Physik* A **358** 169–73

[81] Bohr A and Mottelson B R 1998 *Nuclear Structure* vol 1 (Singapore: World Scientific) chapters 2–4, figures 2–30, p 239

[82] Dobaczewski J, Hamamoto I, Nazarewicz W and Sheikh J A 1994 *Phys. Rev. Lett.* **72** 981–84

[83] Kratz K-L *et al* 1998 *Nucl. Phys.* A **630** 352–67

[84] Pfeiffer B, Kratz K-L and Thielemann F-K 1997 *Z. Phys.* A **357** 235–38

[85] Pfeiffer B, Kratz K-L, Dobaczewski J and Möller P 1996 *Acta Phys. Pol.* B **27** 475–80

[86] Freiburghaus C, Rembges J-F, Rauscher T, Kolbe E, Thielemann F-K, Kratz K-L, Pfeiffer B and Cowan J J 1999 *Astrophys. J.* **516** 381–98

[87] Otsuka T, Suzuki T, Fujimoto R, Grawe H and Akaishi Y 2005 *Phys. Rev. Lett.* **95** 232502

[88] Otsuka T, Fujimoto R, Utsuno Y, Brown B A, Honma M and Mizusaki T 2002 *Phys. Rev. Lett.* **87** 082502

[89] Grawe H 2003 *Acta Phys. Pol.* B **34** 2267–76

[90] Grawe H, Blazhev A, Górska M, Mukha I, Plettner C, Roeckl E, Nowacki F, Grzywacz R and Sawicka M 2005 *Eur. Phys. J.* A **25** (s01) 357–62

[91] Schiffer J P *et al* 2004 *Phys. Rev. Lett.* **92** 162501

[92] Okołowicz J, Płoszajczak M and Rotter I 2003 *Phys. Rep.* **374** 271–83

[93] Ehrmann J B 1951 *Phys. Rev.* **81** 412–16
Thomas R G 1951 *Phys. Rev.* **81** 148–49

[94] Mahaux C and Weidenmüller H 1969 *Shell Model Approaches to Nuclear Reactions* (Amsterdam: North-Holland)

[95] Bennaceur K, Michel N, Nowacki F, Okołowicz J and Płoszajczak M 2000 *Phys. Lett.* B **488** 75–82
Bennaceur K, Nowacki F, Okołowicz J and Płoszajczak M *Nucl. Phys.* A **671** 203–32
[96] Berggren T 1982 *Nucl. Phys.* A **389** 261–84
[97] Michel N, Nazarewicz W, Płoszajczak M and Bennaceur K 2002 *Phys. Rev. Lett.* **89** 042502
[98] Lind P 1993 *Phys. Rev.* C **47** 1903–20
[99] Michel N, Nazarewicz W, Płoszajczak M and Okołowicz J 2003 *Phys. Rev.* C **67** 054311
[100] Michel N, Nazarewicz W and Płoszajczak M 2003 *Phys. Rev.* C **70** 064313
[101] Michel N, Nazarewicz W and Płoszajczak M 2005 *Eur. Phys. J.* A **25** (s01) 357–62
[102] Doornenbal P *et al* 2007 *Phys. Lett.* B **647** 237–42
[103] De Angelis G *et al* 2001 *Eur. Phys. J.* A **12** 51–55
[104] Hagen G, Hjorth-Jensen M and Michel N 2006 *Phys. Rev.* C **73** 064307
[105] Hagen G, Dean D J, Hjorth-Jensen M and Papenbrock T 2007 *Preprint* nucl-th/0610072
[106] Rotureau J, Okołowicz J and Płoszajczak M 2006 *Nucl. Phys.* A **767** 13–57
[107] Rotureau J, Okołowicz J and Płoszajczak M 2005 *Phys. Rev. Lett.* **95** 042503
[108] Bennaceur K, Nowacki F, Okołowicz J and Płoszajczak M 1999 *Nucl. Phys.* A **651** 528–50
[109] Chatterjee R, Okołowicz J and Płoszajczak M 2006 *Nucl. Phys.* A **767** 289–319
[110] Schümann F *et al* 2006 *Phys. Rev.* C **73** 015806
[111] Johnson C W, Kolbe E, Koonin S E and Langanke K 1992 *Astrophys. J.* **392** 320–327
[112] Kolbe E, Langanke K and Assenbaum H J 1988 *Phys. Lett.* B **214** 169–72
[113] Descouvemont P and Baye D 1994 *Nucl. Phys.* A **567** 341–53
[114] Descouvemont P 2004 *Phys. Rev.* C **70** 065802
[115] Navratil P, Bertulani C A and Caurier E 2006 *Phys. Rev.* C **73** 065801
[116] Nollet K M, Pieper S C, Wiringa R B, Carlson J and Hale G M 2007 *Phys. Rev. Lett.* **99** at press
[117] Langanke K and Friedrich H 1987 *Advances in Nuclear Physics* vol 17 (New York: Plenum) p 223
[118] Wildermuth K and Tang Y 1977 *A Unified Theory of the Nucleus* (Braunschweig: Vieweg)
[119] Langanke K 1986 *Nucl. Phys.* A **457** 351–66
[120] Descouvemont P 2003 *Theoretical Models for Nuclear Astrophysics* (New York: Nova Science)
[121] Langanke K 1994 *Advances in Nuclear Physics* vol 21 (New York: Plenum) p 85
[122] Dean D J and Hjorth-Jensen M 2004 *Phys. Rev.* C **69** 054320
[123] Kümmel H, Lührmann K H and Zabolitzki J G 1978 *Phys. Rep.* **36** 1–63
[124] Mihaila B and Heisenberg J H 2000 *Phys. Rev.* C **61** 054309
Mihaila B and Heisenberg J H 2000 *Phys. Rev. Lett.* **84** 1403
[125] Kanada-En'yo Y and Horiuchi H 2001 *Prog. Theor. Phys. Suppl.* **142** 205
[126] Feldmeier H and Schnack J 2000 *Rev. Mod. Phys.* **72** 655–88
[127] Roth P, Neff T, Hergert H and Feldmeier H 2004 *Nucl. Phys.* A **745** 3–33
[128] Neff T, Feldmeier H and Roth R 2005 *Nucl. Phys.* A **752** 321c–4c
[129] Feldmeier H, Neff T and Roth R 2006 *Proc. Frontiers in Nuclear Structure, Astrophysics and Reactions—FINUSTAR (Kos, Greece) AIP Conf. Proc.* vol 831 pp 217–24
[130] Neff T and Feldmeier H 2004 *Nucl. Phys.* A **738** 357c–61c
[131] Kanada-En'yo Y 2002 *Phys. Rev.* C **66** 011303
[132] Kimura M 2004 *Phys. Rev.* C **69** 044319
[133] Kanada-En'yo Y and Kimura M 2005 *Phys. Rev.* C **72** 064322
[134] Dote A, Horiuchi H, Akaishi Y and Yamazaki T 2004 *Phys. Rev.* C **70** 044313
[135] Kanada-En'yo Y 2005 *Phys. Rev.* C **71** 014310
[136] Navratil P, Vary J P and Barrett B R 2000 *Phys. Rev. Lett.* **84** 5728–31
[137] Tohsaki A, Horiuchi H, Schuck P and Röpke G 2001 *Phys. Rev. Lett.* **87** 192501
[138] Chernykh M, Feldmeier H, Neff T, von Neumann-Cosel P and Richter A 2007 *Phys. Rev. Lett.* **98** 032501
[139] Imai N *et al* 2004 *Phys. Rev. Lett.* **92** 062501
[140] Sorlin O *et al* 2002 *Phys. Rev. Lett.* **88** 092501
[141] Langanke K, Terasaki J, Nowacki F, Dean D J and Nazarewicz W 2003 *Phys. Rev.* C **67** 044314
[142] Terasaki J, Engel J, Nazarewicz W and Stoitsev M 2002 *Phys. Rev.* C **66** 054313
[143] Cribeiro A 2005 *PhD Thesis* TU Darmstadt
[144] Neff T, Feldmeier H and Langanke K 2007 *Preprint* nucl-th/0703030
[145] Schatz H, Bildsten L and Cummings A 2003 *Astrophys. J.* **583** L87–90
[146] Gasques L R, Afanasiev A V, Aquilera E F, Beard M, Chamon L C, Ring P, Wiescher M and Yakovlev D G 2005 *Phys. Rev.* C **72** 025806
[147] Burbidge E M, Burbidge G R, Fowler W A and Hoyle F 1957 *Rev. Mod. Phys.* **29** 547–650
[148] Cameron A G W 1957 Stellar evolution, nuclear astrophysics, and nucleogenesis *Report* CRL-41 Chalk River

[149] Wapstra A, Audi G and Thibault C 2003 *Nucl. Phys.* A **729** 337–676

[150] Goriely S, Samyn M, Bender M and Pearson J M 2003 *Phys. Rev.* C **68** 054325

[151] Samyn M, Goriely S and Pearson J M 2003 *Nucl. Phys.* A **725** 69–81

[152] Lunney D, Pearson J M and Thibault C 2003 *Rev. Mod. Phys.* **75** 1021–81

[153] Bender M, Heenen P-H and Reinhard P G 2003 *Rev. Mod. Phys.* **75** 121–80

[154] Rikovska-Stone J 2005 *J. Phys. G: Nucl. Part. Phys.* **31** R211–30

[155] Blomqvist J, Kerek A and Fogelberg B 1983 *Z. Phys.* A **314** 199–204

[156] Korgul A, Mach H, Fogelberg B, Urban W, Kurcewicz, W and Isakov V I 2001 *Phys. Rev.* C **64** 021302

[157] Möller P, Pfeiffer B and Kratz K-L 2002 *Los Alamos LANL-Report* LA-UR-02-2919

[158] Ikeda K I, Fujii S and Fujita J I 1963 *Phys. Lett.* **3** 271–2

[159] Martínez-Pinedo G and Langanke K 1999 *Phys. Rev. Lett.* **83** 4502–5

[160] Martínez-Pinedo G 2001 *Nucl. Phys.* A **688** 357c–64c

[161] Herndl H and Brown B A 1997 *Nucl. Phys.* A **627** 35–52

[162] Pruet J and Fuller G M 2003 *Astrophys. J. Suppl.* **149** 189–203

[163] Fayans S A, Tolokonikov S V, Trykov E L and Zawischa D 2000 *Nucl. Phys.* A **676** 49–119

[164] Borzov I N 2006 *Nucl. Phys.* A **777** 645–675

[165] Cowan J J, Thielemann F-K and Truran J W 1991 *Phys. Rep.* **208** 267–94

[166] Howard W M and Möller P 1980 *At. Data Nucl. Data Tables* **25** 219–85

[167] Mamdouh A, Pearson J, Rayet M, and Tondeur F 2001 *Nucl. Phys.* A **679** 337–58

[168] Möller P, Madland D G, Sierk A J and Iwamoto A 2001 *Nature (Lond.)* **409** 785–90

[169] Peter Möller, Sierk A J and Iwamoto A 2004 *Phys. Rev. Lett.* **92** 072501

[170] Gilbert A and Cameron A G W 1965 *Can. J. Phys.* **43** 1446

[171] Bethe H A 1936 *Phys. Rev.* **50** 332–41

[172] Ignatyuk A V, Smirenkin G N and Tishin A S 1975 *Yad. Phys.* **21** 485
Ignatyuk A V, Istekov K K and Smirenkin G N 1979 *Sov. J. Nucl. Phys.* **29** 450

[173] Rauscher T, Thielemann F-K and Kratz K-L 1997 *Phys. Rev.* C **56** 1613–25

[174] Descouvemont P and Rauscher T 2006 *Nucl. Phys.* A **777** 137–56

[175] Ormand W E 1997 *Phys. Rev.* C **56** R1678–82

[176] Nakada H and Alhassid Y 1997 *Phys. Rev. Lett.* **79** 2939–42

[177] Langanke K 1998 *Phys. Lett.* B **438** 235–41

[178] Alhassid Y, Liu S and Nakada H 1999 *Phys. Rev. Lett.* **83** 4265–68

[179] Özen C, Langanke K, Martínez-Pinedo G and Dean D J 2007 *Phys. Rev.* C **75** 064307

[180] Alhassid Y, Bertsch G F, Liu S and Nakada H 2000 *Phys. Rev. Lett.* **84** 4313–16

[181] Mocelj D, Rauscher T, Martínez-Pinedo G, Langanke K, Pacearescu L, Faessler A, Thielemann F-K and Alhassid Y 2007 *Phys. Rev.* C **75** 045805

[182] Horoi M 2005 *Nucl. Phys.* A **758** 142c–5c

[183] Alhassid Y, Liu S and Nakada H 2007 *Phys. Rev.* C submitted (*Preprint* nucl-th/0607062)

[184] Kalmykov Y *et al* 2006 *Phys. Rev. Lett.* **96** 012502

[185] Langanke K 2006 *Nucl. Phys.* A **778** 233–46

[186] Langanke K, Dean D J and Nazarewicz W 2005 *Nucl. Phys.* A **757** 360–72

[187] Cole A L *et al* 2006 *Phys. Rev.* C **74** 034333

[188] Hagemann M *et al* 2004 *Phys. Lett.* B **579** 251–7

[189] Frekers D 2004 *Nucl. Phys.* A **731** 76–93

[190] Caurier E, Langanke K, Martínez-Pinedo G and Nowacki F 1999 *Nucl. Phys.* A **653** 439–52

[191] Bäumer C *et al* 2003 *Phys. Rev.* C **68** 031303

[192] Langanke K and Martínez-Pinedo G 2000 *Nucl. Phys.* A **673** 481–508

[193] Fuller G M, Fowler W A and Newman M J 1980 *Astrophys. J. Suppl.* **42** 447
Fuller G M, Fowler W A and Newman M J 1982 *Astrophys. J. Suppl.* **48** 279
Fuller G M, Fowler W A and Newman M J 1982 *Astrophys. J.* **252** 715
Fuller G M, Fowler W A and Newman M J 1985 *Astrophys. J.* **293** 1

[194] Langanke K, Martínez-Pinedo G, Sampaio J M, Dean D J, Hix R W, Messer O E, Mezzacappa A, Liebendörfer M, Janka H-Th and Rampp M 2003 *Phys. Rev. Lett.* **90** 241102

[195] Alford W P *et al* 1990 *Nucl. Phys.* A **514** 49–65
Alford W P *et al* 1993 *Phys. Rev.* C **48** 2818–27

[196] El-Kateb S *et al* 1994 *Phys. Rev.* C **49** 3128–36

[197] Williams A L *et al* 1995 *Phys. Rev.* C **51** 1144–53

[198] Langanke K and Martínez-Pinedo G 2002 *Nucl. Phys.* A **704** 154c–64c

[199] Heger A, Langanke K, Martínez-Pinedo G and Woosley S E 2001 *Phys. Rev. Lett.* **86** 1678–81

[200] Heger A, Woosley S E, Martínez-Pinedo G and Langanke K 2001 *Astrophys. J.* **560** 307–25

[201] Hix R W, Messer O E B, Mezzacappa A, Liebendörfer M, Sampaio J, Langanke K, Dean D J and Martínez-Pinedo G 2003 *Phys. Rev. Lett.* **91** 201102

[202] Marek A, Janka H-Th, Buras R, Liebendörfer M and Rampp M 2005 *Astron. Astrophys.* **443** 201–10

[203] Juodagalvis A, Langanke K, Martínez-Pinedo G, Hix W R, Dean D J and Sampaio J M 2005 *Nucl. Phys.* A **747** 87–108

[204] Sampaio J M, Langanke K and Martínez-Pinedo G 2001 *Phys. Lett.* B **511** 11–18

[205] Sampaio J M, Langanke K, Martínez-Pinedo G and Dean D J 2002 *Phys. Lett.* B **529** 19–25

[206] Kolbe E, Langanke K and Fuller G M 2004 *Phys. Rev. Lett.* **92** 111101

[207] Janka H-Th, Langanke K, Marek A, Martínez-Pinedo G and Müller B 2007 *Phys. Rep.* **442** 38–74

[208] Langanke K, Martínez-Pinedo G, Mueller B, Janka H-Th, Marek A, Hix W R, Juodagalvis A and Sampaio J M 2007 *Phys. Rev. Lett.* submitted (*Preprint* 0706.1687v1)

[209] Fuller G M and Meyer B S 1995 *Astrophys. J.* **453** 792–809

[210] Qian Y-Z, Haxton W C, Langanke K and Vogel P 1997 *Phys. Rev.* C **55** 1532–44

[211] Surman R and Engel J 1998 *Phys. Rev.* C **58** 2526–30

[212] Hektor A, Kolbe E, Langanke K and Toivanen J 2000 *Phys. Rev.* C **61** 055803

[213] Kolbe E, Langanke K, Martínez-Pinedo G and Vogel P 2003 *J. Phys. G: Nucl. Part. Phys.* **29** 2569–96

[214] Langanke K and Kolbe E 2002 *At. Nucl. Data Tables* **82** 191–209

[215] Jachowicz N, Heyde K and Ryckebusch J 2002 *Phys. Rev.* C **66** 055501

[216] Engel J, McLaughlin G and Volpe C 2003 *Phys. Rev.* D **67** 013005

[217] Volpe C, Auerbach N, Colo G and Van Giai N 2002 *Phys. Rev.* C **65** 044603

[218] Toivanen J, Kolbe E, Langanke K, Martínez-Pinedo G and Vogel P 2001 *Nucl. Phys.* A **694** 395–408

[219] Descouvemont P and Baye D 1987 *Phys. Rev.* C **36** 54–9

[220] Ikeda K, Takigawa N and Horiuchi H 1968 *Prog. Theor. Phys. Suppl.* **24** 464

[221] Funaki Y, Tohsaki A, Horiuchi H, Schuck P and Röpke G 2003 *Phys. Rev.* C **67** 051306

[222] Wiescher M, Görres J and Schatz H 1999 *J. Phys. G: Nucl. Part. Phys.* **25** R133–61

[223] Schatz H, Aprahamian A, Barnard V, Bildsten L, Cumming A, Oulette M, Rauscher T, Thielemann F-K and Wiescher M 2001 *Phys. Rev. Lett.* **86** 3471–4

[224] Schatz H and Rehm K E 2006 *Nucl. Phys.* A **777** 601–22

[225] Fulton B R 1999 *Contemp. Phys.* **40** 299–311

[226] Freer M and Merchant A C 1997 *J. Phys. G: Nucl. Part. Phys.* **23** 261–323

[227] Becker H W, Kettner K U, Trautvetter H P and Rolfs C 1981 *Z. Phys.* A **303** 305–12

[228] Jiang C L *et al* 2005 *Phys. Rev.* C **71** 044613

[229] Jiang C L, Back B B, Esbensen H, Janssens R V F and Rehm K E 2006 *Phys. Rev.* C **73** 014613

[230] Görres J, Graff S, Wiescher M, Azuma R E, Barnes C A and Wang T R 1992 *Nucl. Phys.* A **548** 414–26

[231] Dababneh S, Heil M, Käppeler F, Görres J, Wiescher M, Reifart R and Leiste H 2003 *Phys. Rev.* C **68** 025801

[232] Drotleff H W, Denker A, Knee H, Soin M, Wolf G, Hammer J W, Greife U, Rolfs C and Trautvetter H P 1993 *Astrophys. J.* **414** 735

[233] Harms V, Kratz K-L and Wiescher M 1991 *Phys. Rev.* C **43** 2849–61

[234] Koehler P E 2002 *Phys. Rev.* C **66** 055805

[235] Busso M, Gallino R and Wasserburg G J 1999 *Annu. Rev. Astron. Astrophys.* **37** 239

[236] Seeger P, Fowler W A and Clayton D D 1965 *Astrophys. J. Suppl.* 121

[237] Käppeler F 1999 *Prog. Part. Nucl. Phys.* **43** 419–83

[238] Käppeler F, Schanz W, Wisshak K and Reffo G 1993 *Astrophys. J.* **410** 370

[239] Doll C, Börner H G, Jaag S, Käppeler F and Andrejtscheff W 1999 *Phys. Rev.* C **59** 492–9

[240] Belic D *et al* 1999 *Phys. Rev. Lett.* **83** 5242–5

[241] Woosley S E, Hartmann D H, Hoffmann R D and Haxton W C 1990 *Astrophys. J.* **356** 272–301

[242] Heger A, Kolbe E, Haxton W C, Langanke K, Martínez-Pinedo G and Woosley S E 2005 *Phys. Lett.* B **606** 258–64

[243] Keil M Th, Raffelt G and Janka H-Th 2003 *Astrophys. J.* **590** 971–91

[244] Takashi Y, Toshitaka K, Hidekazu Y, Keiichi K, Akira T and Hartmann D H 2006 *Phys. Rev. Lett.* **96** 091101

[245] Takashi Y, Toshitaka K and Hartmann D H 2005 *Phys. Rev. Lett.* **94** 231101

[246] Byelikov A *et al* 2007 *Phys. Rev. Lett.* **98** 082501

[247] Woosley S E, Heger A and Weaver T A 2002 *Rev. Mod. Phys.* **74** 1015–71

[248] Fröhlich C *et al* 2006 *Astrophys. J.* **637** 415–26

[249] Pruet J, Woosley S E, Buras R, Janka H T and Hoffman R D 2005 *Astrophys. J.* **623** 325–36

[250] Cowan J, Sneden Ch, Lawler J E and Den Hartog E A 2006 *Proc. Int. Symp. Nuclear Astrophysics—Nuclei in the Cosmos—IX* ed A Mengoni *Proc. Sci.* http://pos.sissa.it//archive/conferences/028/014/NIC-IX_014.pdf

[251] Cowan J J and Sneden C 2006 *Nature* **440** 1151–56
[252] Wasserburg G J, Busso M and Gallino R 1996 *Astrophys. J.* **466** L109–14
[253] Qian Y Z and Wasserburg G J 2001 *Astrophys. J.* **559** 925–41
[254] Wanajo S and Ishimaru Y 2006 *Nucl. Phys.* A **777** 676–99
[255] Travaglio C, Gallino R, Arnone E, Cowan J, Jordan F and Sneden Ch 2004 *Astrophys. J.* **601** 864–84
[256] Arnould M and Goriely S 2003 *Phys. Rep.* **384** 1–84
[257] Costa V, Rayet M, Zappalà R-A and Arnould M 2000 *Astron. Astrophys.* **358** L67–70
[258] Hayakawa, T, Iwamoto N, Shizuma T, Kajino T, Umeda H and Nomoto K 2004 *Phys. Rev. Lett.* **93** 161102
[259] Dauphas N, Rauscher T, Marty B and Reisberg L *Nucl. Phys.* A **719** 287c–95c
[260] Fröhlich C, Martínez-Pinedo G, Liebendörfer M, Thielemann F-K, Bravo E, Hix W R, Langanke K and Zinner N T 2006 *Phys. Rev. Lett.* **96** 142502
[261] Pruet J, Hoffman R D, Woosley S E, Janka H-T and Buras R 2006 *Astrophys. J.* **644** 1028–39
[262] Hanawald M *et al* 1999 *Phys. Rev. Lett.* **82** 1391–4
[263] Langanke K, Terasaki J, Nowacki F, Dean D J and Nazarewicz W 2003 *Phys. Rev.* C **67** 044314
[264] Sawicka M *et al* 2002 *Eur. Phys. J.* A **16** 51–4
[265] Bürger A *et al* 2005 *Phys. Lett.* B **622** 29–34
[266] Dinca D-C *et al* 2005 *Phys. Rev.* C **71** 041302
[267] Janssens R V F *et al* 2002 *Phys. Lett.* B **546** 55–62
[268] Cowan J J and Thielemann F-K 2004 *Phys. Today* 47–53
[269] Freiburghaus C, Rosswog S and Thielemann F-K 1999 *Astrophys. J.* **525** L121–4
[270] Wheeler J C, Cowan J J and Hillebrandt W 1998 *Astrophys. J.* **493** L101–4
[271] Cameron A G W 2001 *Astrophys. J.* **562** 456–69
[272] Woosley S E, Wilson J R, Mathews G J, Hoffman R D and Meyer B S 1994 *Astrophys. J.* **433** 229–46
[273] Witti J, Janka H-Th and Takahashi K 1994 *Astron. Astrophys.* **286** 857–69
[274] Meyer B S, Mathews G J, Howard W M, Woosley S E and Hoffman R D 1992 *Astrophys. J.* **399** 656
[275] Woosley S E and Hoffmann R D 1992 *Astrophys. J.* **395** 202
[276] Kratz K-L, Harms V, Wöhr A and Möller P 1988 *Phys. Rev.* C **38** 278–84
[277] Zhang Y H *et al* 2004 *Phys. Rev.* C **70** 024301
[278] Grzywacz R *et al* 1998 *Phys. Rev. Lett.* **81** 766–69
[279] Daugas J M *et al* 2000 *Phys. Lett.* B **476** 213–18
[280] Sawicka M *et al* 2004 *Eur. Phys. J.* A **20** 109–10
[281] Grzywacz R 2005 *Eur. Phys. J.* A **25** (s01) 89–92
[282] Mazzocchi C *et al Phys. Lett.* B **622** 45–54
[283] Franchoo S *et al* 2001 *Phys. Rev.* C **64** 054308
[284] Sawicka M *et al* 2003 *Phys. Rev.* C **68** 044304
[285] Grawe H *et al* 2002 *Nucl. Phys.* A **704** 211c–222c
[286] Möller P, Pfeiffer B and Kratz K-L 2003 *Phys. Rev.* C **67** 055802
[287] Hosmer P T *et al* 2005 *Phys. Rev. Lett.* **94** 112501
[288] Kratz K-L 1993 *Astrophys. J.* **403** 216–238
[289] Chen B, Dobaczewski J, Kratz K-L, Langanke K, Pfeiffer B, Thielemann F-K and Vogel P 1995 *Phys. Lett.* B **355** 37–44
[290] Sharma M M and Farhan A R 2002 *Phys. Rev.* C **65** 044301
[291] Kautzsch T *et al* 2000 *Eur. Phys. J.* A **9** 201–6
[292] Jungclaus A *et al* 2007 *Phys. Rev. Lett.* **99** at press
[293] Anguiano M, Egido J L and Robledo L M 2001 *Nucl. Phys.* A **696** 467–93
[294] Górska M *et al* 2007 private communication
[295] Kratz K-L, Gabelmann H, Hillebrandt W, Pfeiffer B, Schlösser K and Thielemann F-K 1986 *Z. Phys.* A **325** 489–90
[296] Cuenca-Garcia J J *et al* 2007 *Eur. Phys. J.* A submitted
[297] Steer S J *et al* 2007 *Acta Phys. Pol.* B **38** 1283–6
[298] Podolyak Z *et al* 2007 *Eur. Phys. J.* A at press
[299] Langanke K and Martínez-Pinedo G 2003 *Rev. Mod. Phys.* **75** 819–62
[300] Kodama T and Takahashi K 1975 *Nucl. Phys.* A **239** 489–510
[301] Gaimard J-J and Schmidt K-H 1991 *Nucl. Phys.* A **531** 709–45
[302] Benlliure J, Grewe A, de Jong M, Schmidt K-H and Zhdanov S 1998 *Nucl. Phys.* A **628** 458–78
[303] Myers W D and Świątecki W J 1999 *Phys. Rev.* C **60** 014606
[304] Panov I V, Kolbe E, Pfeiffer B, Rauscher T, Kratz K-L and Thielemann F-K 2005 *Nucl. Phys.* A **747** 633–54

[305] Martínez-Pinedo G *et al* 2006 *Proc. Int. Symp. Nuclear Astrophysics—Nuclei in the Cosmos—IX* ed A Mengoni *Proc. Sci.* http://pos.sissa.it//archive/conferences/028/064/NIC-IX_064.pdf

[306] Martínez-Pinedo G, Mocelj D, Zinner N T, Kelić A, Langanke K, Panov I, Pfeiffer B, Rauscher T, Schmidt K-H and Thielemann F-K 2007 *Prog. Part. Nucl. Phys.* **59** 199–205

[307] Martínez-Pinedo G *et al* 2007 in preparation

[308] Cowan J J, Pfeiffer B, Kratz K-L, Thielemann F-K, Sneden Ch, Burles S, Tytler D and Beers T C 1999 *Astrophys. J.* **521** 194–205

[309] Fisker J L, Thielemann F-K and Wiescher M 2004 *Astrophys. J.* **608** L61–4

[310] Fisker J L, Brown E F, Liebendörfer M, Thielemann F-K and Wiescher M 2005 *Nucl. Phys.* A **752** 604–7

[311] Gade A *et al* 2007 *Phys. Rev.* C **76** at press

[312] Lenzi S M *et al* 2002 *Phys. Rev. Lett.* **87** 122501

[313] Zuker A P, Lenzi S, Martínez-Pinedo G and Poves A 2002 *Phys. Rev. Lett.* **89** 142502

[314] Herndl H, Görres J, Wiescher M, Brown B A and Van Wormer L 1995 *Phys. Rev.* C **52** 1078–94

[315] Rehm K E *et al* 2000 *Nucl. Instrum. Methods* A **449** 208–16

[316] Rudolph D *et al* 1998 *Phys. Rev. Lett.* **80** 3018–21

[317] Rudolph D *et al* 2001 *Nucl. Phys.* A **694** 132–46

[318] Mukha I *et al* 2006 *Nature* **439** 298–302

[319] Grigorenko L, Langanke K, Shul'gina N B and Zhukov M V 2006 *Phys. Lett.* B **641** 254–9

[320] Möller P and Randrup J 1990 *Nucl. Phys.* A **514** 1–48

[321] Woosley S E, Heger A and Weaver T A 2002 *Rev. Mod. Phys.* **74** 1015–71

[322] Liddick S N *et al* 2006 *Phys. Rev. Lett.* **97** 082501

[323] Seweryniak D *et al* 2006 *Phys. Rev.* C **73** 061301(R)

[324] Roeckl E 2004 *The Euroschool Lectures on Physics with Exotic Beams, vol I* (*Lecture Notes in Physics* vol 651) (Berlin: Springer) pp 223–61

[325] Woosley S E, Heger A, Cumming A, Hoffman R D, Pruet J, Rauscher T, Fisker J L, Schatz H, Brown B A and Wiescher M 2004 *Astrophys. J. Suppl.* **151** 75–102

[326] Fisker J L, Hix W R, Liebendörfer M and Thieleman F-K 2003 *Nucl. Phys.* A **718** 614c–616c